creative commons

COMMONS DEED

저작자표시-비영리-변경금지 2.0 대한민국

이용자는 아래의 조건을 따르는 경우에 한하여 자유롭게

- 이 저작물을 복제, 배포, 전송, 전시, 공연 및 방송할 수 있습니다.

다음과 같은 조건을 따라야 합니다:

저작자표시. 귀하는 원저작자를 표시하여야 합니다.

비영리. 귀하는 이 저작물을 영리 목적으로 이용할 수 없습니다.

변경금지. 귀하는 이 저작물을 개작, 변형 또는 가공할 수 없습니다.

- 귀하는, 이 저작물의 재이용이나 배포의 경우, 이 저작물에 적용된 이용허락조건을 명확하게 나타내어야 합니다.
- 저작권자로부터 별도의 허가를 받으면 이러한 조건들은 적용되지 않습니다.

저작권법에 따른 이용자의 권리는 위의 내용에 의하여 영향을 받지 않습니다.

이것은 이용허락규약(Legal Code)을 이해하기 쉽게 요약한 것입니다.

Disclaimer

dCollection

공학박사학위논문

Ph. D. Thesis

An Experimental Study on Combustion Instability and NO_X Emission Characteristics of $H_2/CO/CH_4$ Syngas in a Gas Turbine Combustor

가스터빈 연소기에서 $H_2/CO/CH_4$ 합성가스의 연소불안정 및 NO_X 배출 특성에 관한 실험 연구

2014년 2월

서울대학교 대학원

기계항공공학부

이 민 철

An Experimental Study on Combustion Instability and NO_X Emission Characteristics of $H_2/CO/CH_4$ Syngas in a Gas Turbine Combustor

가스터빈 연소기에서 $H_2/CO/CH_4$ 합성가스의 연소불안정 및 NO_X 배출 특성에 관한 실험 연구

지도교수 윤 영 빈

이 논문을 공학박사 학위논문으로 제출함.

2013년 11월

서울대학교 대학원

기계항공공학부

이 민 철

이민철의 공학박사 학위논문을 인준함.

2013년 12월

위 원 장 : 鄭仁碩 (인)

부위원장 : 尹寧彬 (인)

위 원 : 余載翊 (인)

위 원 : 車東震 (인)

위 원 : 安奎福 (인)

“The LORD is my shepherd, I shall not be in want.
He makes me lie down in green pastures,
he leads me beside quiet waters,
he restores my soul.
He guides me in paths of righteousness for his name's sake.
Even though I walk through the valley of the shadow of death,
I will fear no evil, for you are with me;
your rod and your staff, they comfort me.
You prepare a table before me in the presence of my enemies.
You anoint my head with oil; my cup overflows.
Surely goodness and love will follow me all the days of my life,
and I will dwell in the house of the LORD forever.”

Psalm 23: 1~6 (NIV)

“Do not be anxious about anything,
but in everything, by prayer and petition, with thanksgiving,
present your requests to God.
And the peace of God, which transcends all understanding,
will guard your hearts and your minds in Christ Jesus.”
“I can do everything through him who gives me strength.”

Philippians 4: 6~7, 13 (NIV)

ABSTRACT

The effects of the $H_2/CO/CH_4$ syngas compositions and the N_2/CO_2/steam dilution ratios are investigated in a partially-premixed gas turbine model combustor, which can prevent flashback problem even in high hydrogen content to understand the combustion characteristics of new fuel for IGCC and SNG plants. The temperatures of flame and combustor, NO_x/CO emissions, combustion instability, flame stability, and flame structures are examined. Cause and effects of each combustion characteristics were determined from the relationship between them. For example, in order to identify the detailed flame structure during combustion instability, OH^*-chemiluminescence images were taken at the rate of 12500 frame/sec using the high-speed intensified ICCD camera and/or planar OH^* distribution in flame was obtained using phase-locked OH^*-PLIF setup.

First, the fuel composition effects of $H_2/CO/CH_4$ syngas (0~100%, span: 12.5% by LHV) on trends of each combustion performance were investigated by using ternary diagram. A lot of NO_x is emitted at high H_2 composition due to high flame temperature and high CO composition due to long residence time. This feature could be also explained by flame structure and combustor temperature. H_2/CH_4 syngas flame generated high combustion instability at the frequency of 750 Hz, 1000 Hz and 1500 Hz correspond to 3L, 4L and 6L mode which varies according to the fuel composition. This self-excited high multi-mode combustion instability characteristics have been studied by investigating combustion properties, flame structure, Rayleigh indices, proper orthogonal decomposition and characteristic time scales from the images of high-speed chemiluminescence and OH^*-PLIF. The flames have different shapes and generate different combustion instability frequency at near 4L or 3L mode with their harmonics. The combustion oscillation frequency which is non-linear for fuel composition was appeared to be linearly proportional to T_{ad} and S_L. Phase-synchronized OH^*-PLIF images suggested clues of an important combustion instability driving mechanism including the periodic alternation of flame attachment/detachment and coupling of vortex with everlasting heat release at the outer recirculation zone due to high reactivity of high

hydrogen fuels. These images also used for the precise calculation of 2-D flame length by obtaining centroid of heat release intensity when performing time-lag analysis. The Rayleigh index results notified the dependence of the location and intensity of combustion instability driving/damping on the fuel composition and instability mode. For higher H_2 containing flame (4th mode), driving and damping is occurred in narrow region but with high heat release density and the frequency of Rayleigh index was doubled. Otherwise in case of 3rd mode Rayleigh index shape was similar with pressure fluctuation due to the characteristics of multi-mode combustion instability with high superposition of higher harmonics. Analysis of proper orthogonal decomposition from high-speed OH^* images showed the distinct coherent structures and large roll-up of flame are responsible for generating flame oscillations for each mode. High cross-correlation was found between proper orthogonal modes of 4th mode indicating convection of these coherent structures. When conducting time-lag analysis for syngas in a partially-premixed gas turbine model combustor, the significance of skewness time induced by wave distortion and importance of careful inspection on L_{flame} using 2-D OH^*-PLIF is verified by showing the improvement in prediction accuracy.

Next, the effect of the fuel-side dilution of N_2, CO_2 and steam on the combustion characteristic of syngas has been studied. This fuel-side dilution reduced flame temperature, combustor temperature and consequently NO_x but significantly increased CO emission due to incomplete combustion at low flame temperature. From the NO_x results of each diluent, it can be obtained that the dilution of syngas with nonflammable gas decreases NO_x emissions, and the amount of NO_x reduction per unit power is logarithmically related to only the diluent's heat capacity which is the product of mass flow rate of the diluent and constant pressure heat capacity. This relationship between NO_x reduction and diluent heat capacity is verified by inducing analytic solutions with some appropriate assumptions.

Finally, based on the combustion results of $H_2/CO/CH_4$ syngas with N_2/CO_2/steam dilution, the combustion tests were performed for the commercial fuels: coal-derived syngas and SNG. The results of coal gas of which H_2/CO ratio is 1/2 showed that N_2

dilution is appeared to be negative in view of flame stability and CO emission but can be operable with enough stability margins and to be very positive in view of NO_x emission. Combustion test of C0, C1, C3 and C5 SNGs of which H_2 content is 0%, 1%, 3% and 5% but Weber index is constant was performed. Combustion characteristics of temperature and NO_x/CO emission were almost identical for all SNGs but combustion instabilities of C0 and C1 were slightly differed from that C3 and C5 in frequency as well as amplitude. This feature also closely visualized by examining the high-speed unsteady flame behaviors. Even though the impact on combustion instability is not so significant for SNG which contains over 1% H_2, this 1% where the change of combustion starts can be provided as the quality standard in SNG considering the existence of various types of natural gas firing gas turbines.

***Keywords*:** Combustion instability; Nitrogen oxides; Synthetic gas; Gas turbine combustion; Integrated gasification combined cycle; Synthetic natural gas

***Student number*:** 2011-30206

CONTENTS

ABSTRACT i
KEYWORDS iii
CONTENTS iv
LIST OF FIGURES vii
LIST OF TABLES xii
NOMENCLATURE xiii

CHAPTER 1
INTRODUCTION 1

CHAPTER 2
EXPERIMENTAL APPARATUS AND TECHNIQUES 9
2.1 The gas turbine combustion test facility and test conditions 9
2.2 Model gas turbine combustor 12
2.3 Measurements and optical setup 14

CHAPTER 3
COMBUSTION CHARACTERISTICS OF H_2/CO/CH_4 SYNGAS 18
3.1 Determination of test conditions 18
3.2 Test results of temperature, combustion instability, NO_x and CO emissions and flame structure 20
3.2.1 Temperature characteristics 20
3.2.2 NO_x and CO emission characteristics 21
3.2.3 Combustion instability characteristics 24
3.2.4 Flame structures 25
3.3 Analysis of combustion instability 27
3.3.1 Frequency and mode analysis 27
3.3.2 OH^*-PLIF 33

3.3.3 Rayleigh indices 34
3.3.4 Proper orthogonal decomposition analysis 38
3.3.5 Time-lag analysis in multi-mode combustion instability 39
3.3.6 Summary and conclusion of the CI analysis for $H_2/CO/CH_4$ syngas . 42

CHAPTER 4
EFFECT OF N_2/CO_2/STEAM DILUTION ON THE SYNGAS COMBUSTION ... 43
4.1 Effect of N_2 dilution on the combustion Characteristics of $H_2/CO/CH_4$ syngas 43
4.2 Effect of N_2/CO_2/steam dilution on the combustion characteristics H_2/CO syngas 48
4.2.1 NOx emission characteristics 49
4.2.2 CO emission characteristics 53
4.2.3 Combustion oscillation characteristics 53
4.2.4 Temperature characteristics 56
4.2.5 Summary and conclusion of N_2/CO_2/steam dilution study 59

CHAPTER 5
APPLICATION ON THE COMMERCIAL GASES: COAL GAS AND SYNTHETIC NATURAL GAS 60
5.1 Coal-derived syngas combustion 60
5.1.1 Flame stability map 63
5.1.2 Temperature characteristics 67
5.1.3 NO_x and CO emission characteristics 68
5.1.4 Combustion oscillation characteristics 73
5.1.5 Flame structures 75
5.1.6 Summary and conclusions of coal gas combustion study 77
5.2 Synthetic natural gas combustion 78
5.2.1 Temperature characteristics 80
5.2.2 CO and NO_x emission characteristics 81

5.2.3 Combustion oscillation characteristics 83
5.2.4 Flame structures and heat release oscillation 84
5.2.5 Summary and conclusions of SNG combustion study 89

CHAPTER 6
CONCLUSION 91

APPENDICES 94
Appendix A. Calculation of adiabatic flame temperature 94
Appendix B. Calculation of ignition delay time 97
Appendix C. Calculation of larminar flame speed 99
Appendix D. Analysis of proper orthogonal decomposition 100
Appendix E. Carbonyl trapper 105

REFERENCES 107

ABSTRACT IN KOREAN 115
KEYWORDS IN KOREAN 118
ACKNOWLEDGEMENT IN KOREA 119

LIST OF FIGURES

Fig. 1.1	Estimated bird's-eye view of Taean IGCC plant.	2
Fig. 1.2	Estimated bird's-eye view of Kwangyang SNG plant.	6
Fig. 2.1	Schematic diagram of the syngas turbine combustion test facility.	11
Fig. 2.2a	Schematic diagram of the gas turbine model combustor and measurements.	12
Fig. 2.2b	Magnified view of burner head and quartz liner.	13
Fig. 2.2c	Fig. 2.2c Oblique view of quartz liner and burner head.	13
Fig. 2.2d	Cross-sectional view of fuel nozzle.	13
Fig. 2.2e	Direct photo of tested fuel nozzle.	13
Fig. 2.3	Optical setup for OH^*-PLIF and OH^*-chemiluminescence.	17
Fig. 2.4	Timing sequences of signals for triggering the ICCD camera for phase-synchronized OH^*-PLIF	17
Fig. 3.1	Test conditions of $H_2/CO/CH_4$ syngas combustion. (a) Ternary test matrix and test number (b) Ternary test colorization corresponding to test matrix	19
Fig. 3.2	Temperatures of adiabatic flame and combustor liner at $40kW_{th}$ and $50kW_{th}$. (a) Adiabatic flame temperature at $40kW_{th}$ (b) Adiabatic flame temperature at $50kW_{th}$ (c) Combustor liner temperature at $40kW_{th}$ (d) Combustor liner temperature at $50kW_{th}$	21
Fig. 3.3	NOx emission at (a) $40kW_{th}$ (left) and (b) $50kW_{th}$ (right).	23
Fig. 3.4	CO emission at (a) $40kW_{th}$ (left) and (b) $50kW_{th}$ (right).	23
Fig. 3.5	RMS of $P'_{(3)}$ at (a) $40kW_{th}$ (left) and (b) $50kW_{th}$ (right).	23
Fig. 3.6	Time-averaged OH^*-Chemiluminescence (upper) and their Abel-deconvoluted images (lower) with the increment of (a) H_2 in CH_4 flame, (b) H_2 in CO flmae and CO in H_2/CH_4 flame. T# indicates the test number in Fig. 3.1.	25

Fig. 3.7	Time-averaged OH^*-chemiluminescence (left) and Abel-deconvoluted images (right) at $40kW_{th}$ and $50kW_{th}$.	26
Fig. 3.8	Representative pressure fluctuation cycles of 4th and 3rd mode CIs.	29
Fig. 3.9	FFTs of representative pressure fluctuation cycles of 4th and 3rd modes.	30
Fig. 3.10	Relationship between S_L and ignition delay time for all fuels studied.	30
Fig. 3.11	Relationship between adiabatic flame temperature and ignition delay time for all fuels studied.	31
Fig. 3.12	Relationship between adiabatic flame temperature and laminar flame speed for all fuels studied.	31
Fig. 3.13	Effect of laminar flame speed and adiabatic flame temperature on the frequency of the CI for all fuels studied. (a) Effect of laminar flame speed. (b) Effect of adiabatic flame temperature.	32
Fig. 3.14	Images of phase-resolved OH^*-PLIF for (a) 3rd and (b) 4th mode CIs. (upper half: instantaneous image, lower half: averaged image of 100 instantaneous images)	34
Fig. 3.15	Temporal variation of normalized pressure and heat release fluctuation and Rayleigh indices for 3rd mode. (a) Normalized pressure and heat release fluctuation (top), mean axial RI (middle), and normalized integral RI (bottom) for 3rd mode. (b) RI maps with corresponding time step of Fig. 3.13a	36
Fig. 3.16	Temporal variation of normalized pressure and heat release fluctuation and Rayleigh indices for 3rd mode. (b) RI maps with corresponding time step of Fig. 3.14c and 3rd mode.	37
Fig. 3.17	Mode shapes from POD analysis of 3rd and 4th mode CIs with corresponding frequency and fractions of their energy level.	39
Fig. 3.18	Evolution of multi-mode pressure disturbance in GTMC.	41

Fig. 3.19	(a) Time-lag plot for 1-D flame model, 2-D flame model and 2-D flame model with $\boldsymbol{\tau}_{skew}$ and (b) fraction of time scales in $\boldsymbol{\tau}_{tot}$.	41
Fig. 4.1	Quaternary diagram of $H_2/CO/CH_4/N_2$ syngas to describe the dilution ratio of nitrogen.	44
Fig. 4.2	Combustor liner temperature at $40kW_{th}$ with respect to N_2 dilution ratio.	46
Fig. 4.3	Combustor liner temperature at $50kW_{th}$ with respect to N_2 dilution ratio.	46
Fig. 4.4	NOx emission at $40kW_{th}$ with respect to N_2 dilution ratio.	46
Fig. 4.5	NOx emission at $50kW_{th}$ with respect to N_2 dilution ratio.	46
Fig. 4.6	CO emission at $40kW_{th}$ with respect to N_2 dilution ratio.	47
Fig. 4.7	CO emission at $50kW_{th}$ with respect to N_2 dilution ratio.	47
Fig. 4.8	RMS of P'_3 at $40kW_{th}$ with respect to N_2 dilution ratio.	47
Fig. 4.9	RMS of P'_3 at $50kW_{th}$ with respect to N_2 dilution ratio.	47
Fig. 4.10	NO_x emissions with respect to the N_2 dilution ratio.	51
Fig. 4.11	NO_x reduction with respect to the diluent heat capacity of N_2, CO_2, and steam.	52
Fig. 4.12	NO_x reduction per unit heat input with respect to the diluent heat capacity of N_2, CO_2, and steam.	52
Fig. 4.13	CO emissions with respect to the DR of N_2, CO_2, and steam.	55
Fig. 4.14	Pressure fluctuation with respect to the DR of N_2, CO_2, and steam.	55
Fig. 4.15	Direct flame photos of H_2/CO syngas with respect to the N_2 dilution ratio	56
Fig. 4.16	Characteristics of fuel nozzle temperature, dump plane temperature, exit gas temperature and adiabatic flame temperature with respect to the N_2 dilution ratio.	58
Fig. 5.1	Criteria for classification on a flame stability map.	65
Fig. 5.2	Flame stability map of Taean and Buggenum syngases. (a) Flame	66

stability map of Taean and Buggenum syngases according to the DR_{N2}. (b) Flame stability map of Taean and Buggenum syngases according to the nitrogen mole fraction in fuel.

Fig. 5.3 Temperature characteristics of Taean and Buggenum syngases according to the IR_{N2}. 68

Fig. 5.4 NO_x and CO emissions of Taean and Buggenum syngases. (a) NO_x and CO emissions of Taean syngas according to the IR_{N2}. (b) NO_x and CO emissions of Buggenum syngas according to the IR_{N2}. 71

Fig. 5.5 NO_x emissions of Taean and Buggenum syngases with respect to T_{ad}. 72

Fig. 5.6 Primary combustion zone of Taean and Buggenum syngases 72

Fig. 5.7 CO emissions of Taean and Buggenum syngases with respect to T_{ad}. 73

Fig. 5.8 RMS values of pressure fluctuations according to the IR_{N2}. 74

Fig. 5.9 FFT of pressure fluctuations of Buggenum syngas at 35 kW with 100% DR_{N2}. 75

Fig. 5.10 OH^*-chemiluminescence and Abel-deconvoluted images of Taean and Buggenum. 76

Fig. 5.11 Fuel and air supply sequence. 79

Fig. 5.12 Temperatures of combustor with respect to relative power output. 81

Fig. 5.13 CO and NO_x emissions of C0, C1, C3 and C5 gases with respect to heat input. 82

Fig. 5.14 Pressure fluctuations of C0, C1, C3 and C5 gases with respect to heat input. 85

Fig. 5.15 FFT results of pressure fluctuations with respect to heat input of C0 gas. 86

Fig. 5.16 FFT results of pressure fluctuations with respect to heat input of C5 gas. 86

Fig. 5.17 Normalized fluctuations of pressure and heat release at $60kW_{th}$ heat input of C0 natural gas. 86

Fig. 5.18	Normalized fluctuations of pressure and heat release at 60kW$_{th}$ heat input of C5 natural gas.	87
Fig. 5.19	OH*-chemiluminescence images at 60kW$_{th}$.	88
Fig. 5.20	Cause and effect diagram for the relationship between combustion properties in SNG and gas turbine combustion characteristics. (+): positive effect, (-): negative effect, dashed line: weak effect.	89
Fig. B.1	Configuration of reactors in CHEMKIN for the calculation of ignition delay time.	97
Fig. B. 2	Results of the CHEMKIN simulation for the calculation of ignition delay time. (a) Temperature and pressure (b) CH* (c) Time derivative of temperature and pressure in RCM (left) (d) Time derivative of CH* in RCM (right)	98
Fig. C.1	Configuration of reactors for the calculation of laminar burning velocity.	99
Fig. C.2	Laminar burning velocity with respect to test number from 1 to 45.	99
Fig. E.1	Comparison of quartz tubes between before (left) and after (right) burning of CO containing fuels.	105
Fig. E.2	Reddish particles colleted for XRD analysis	106
Fig. E.3	XRD Analyzer (D8 Advance)	106
Fig. E.4	XRD Analysis result (2-theta vs. intensity).	106

LIST OF TABLES

Table 2.1	Baseline operating conditions for this study.	11
Table 3.1	Properties of hydrogen, carbon monoxide, and methane.	27
Table 4.1	Experimental conditions for N_2/CO_2/steam dilution test.	48
Table 4.2	Syngas gas composition and constant pressure specific heat at 573K.	49
Table 5.1	Syngas composition of Taean and Buggenum.	62
Table 5.2	Combustion properties of hydrogen, methane, ethane, propane and n-buthane.	78
Table 5.3	Chemical composition and combustion properties of tested gases.	79

NOMENCLATURE

Alphabet

ANOVA	analysis of variance
c	sonic velocity
c_p	specific heat at constant pressure
$c_{p,i}$	constant pressure specific heat of i-gas
CCS	carbon capture and storage
CI	combustion instability
COFM	continuous oscillation feedback mechanism
D	dimension
DAQ	data acquisition system
DR	dilution ratio
DR_{CO2}	dilution ratio of carbon dioxide
DR_{N2}	dilution ratio of nitrogen
DR_{steam}	dilution ratio of steam
DLN	dry low NO_x
DME	dimethyl ether
f	frequency
f_D	frequency of dominant mode
$f_{p'}$	frequency of pressure fluctuation
$f_{q'}$	frequency of heat release fluctuation
FDF	flame describing function
FOV	field of view
FFT	fast Fourier transform
FL	flammability limit
FL_{mix}	flammability limit of the mixture
FL_i	flammability limits of the binary sub-mixtures

FTF	flame transfer function
GTMC	gas turbine model combustor
HHC	high hydrogen content
IGCC	integrated gasification combined cycle
IR	integration ratio
IR_{N2}	integration ratio of nitrogen
IRI	integral Rayleigh index
L	length
L_{flame}	flame length
$L_{flame, PPM}$	flame length of a partially-premixed gas turbine model combustor
$L_{flame, LPM}$	flame length of a lean premixed gas turbine model combustor
$L_{mix, PPM}$	fuel/air mixing length of a partially-premixed gas turbine model combustor
$L_{mix, LPM}$	fuel/air mixing length of a lean premixed gas turbine model combustor
LFL	lower flammability limit
LHV	lower heating value
LSI	low swirl injector
LPM	lean-premixed
$\dot{m}$	mass flow rate
$\dot{m}_{air}$	mass flow rate of air
MFC	mass flow controller
n	integer
ORZ	outer recirculation zone
p'	pressure fluctuation
P_3,	combustion chamber inlet pressure
$P'_{(3)}$	dynamic pressure at dump plane
P'_{rms}	root mean squared value of dynamic pressure
P_{th}	thermal power (heat input)
PLIF	planar laser induced fluorescence

POD	proper orthogonal decomposition
POM	proper orthogonal mode
PPM	the partially-premixed
ppm	parts per milion
PVC	processing vortex core
q'	heat release fluctuation
q'_{PLIF}	heat release fluctuation calculated by PLIF images
q'_{chem}	heat release fluctuation calculated by chemiluminescence images
R	gas constant
RCM	rapid compression machine
R^2	correlation coefficient
R_{air}	ideal gas constant for air
RR	cross-correlation coefficient
RI	Rayleigh index
RMS	root mean square
SCGP	Shell coal gasification process
SNG	synthetic natural gas
S_L	laminar flame speed
T	temperature
T_{ad}	adiabatic flame temperature
T_n	temperature at fuel nozzle
T_d	temperature at dump plane
T_{ex}	gas temperature at combustor exit
TIT	turbine inlet temperature
T_3	combustor liner temperature
T_{in}	combustion chamber inlet temperature
TLA	time-lag analysis
V_{pz},	volume of the primary zone
WLN	wet low NO_x

x_i	volume percentage of a sub-mixture in total fuel
XRD	X-ray diffractometer
[X]	molar concentration of species X

Greek

γ	*specific gravity*
τ	time
τ_{acou}	acoustic time
τ_{conv}	convective time
τ_{res}	residence time
$\tau_{delay,\ trigger}$	delay time of trigger
$\tau_{delay,\ trigger}$	delay time of laser
τ_{ign}	ignition delay time
τ_{osc}	oscillation time (period of oscillation)
τ_{chem}	chemical reaction time
τ_{skew}	skewness ime
θ	phase-angle
$\theta_{p'-q'}$	phase-angle between p' and q'
θ_{RR}	phase difference

Subscripts

acou	acoutsic
ad	adiabatic
chem	chemical
conv	convective
d	dump

ex	exit
ign	ignition
L	laminar
mix	mixture
n	nozzle
skew	skewness
osc	oscillation
res	residence
th	thermal

CHAPTER 1
INTRODUCTION

In this energy-climate era [1], the widespread concern about global warming and the ongoing depletion of fossil fuels is not only a social issue, but it also presents a vital problem for the survival of mankind. Among the promising efforts aiming to solve these problems, gasification technology is one of the key candidates because it can utilize abundant coal, residual oil, CO_2 neutral biomass and agricultural wastes. Furthermore, emissions of NO_x, SO_x, and CO_2 can be reduced to a negligible level when using integrated gasification combined cycle (IGCC) technology as it offers low NO_x combustion, syngas desulfurization, and carbon capture and storage (CCS) capabilities. This technology can also be used for the production of hydrogen, chemicals, and liquid fuels so it can be called a multi-source and multi-purpose technology. However, this promising IGCC technology has not yet been fully developed, meaning many outages have been reported from previous major coal-based IGCC plants including Tampa Electric [2], Wabash River [3], Puertollano, Buggenum and Nakoso. More specifically, unplanned outage due to fuel nozzle and liner burn out, combustion instability (CI), and compressor surging in gas turbine unit is the most critical source of low availability [2, 3, 4]. Since many outages in a gas turbine combustor of new IGCC plants are highly anticipated based on lessons learned from existing IGCC plants, more detailed understanding of syngas combustion is necessary and mature technology of syngas turbine should be adapted to enjoy renaissance era of IGCC.

In an effort to solve such problems, many researches have been conducted to study H_2/CO syngas combustion and to assess the fuel composition effect. These syngas combustion researches can be categorized into two parts: one fundamental research on the combustion characteristics such as laminar burning velocity [5, 6], ignition [7, 8], flashback [9], blow-off [10], flammable limit [11], emissions [12-14] and etc., and the other advanced research using gas turbine-like combustor at gas turbine-similar condition

[15-21]. As a former group, Natarajan et al. examined the effect of CO_2 dilution, preheating, and pressure on the laminar flame speed of H_2/CO mixtures by using two measurement approaches: flame area images of a conical Bunsen flame and velocity profile measurements in a one-dimensional stagnation flame [5]. Walton et al. provided experimental data set on the ignition delay time of hydrogen and carbon monoxide syngas at conditions of high pressure and high temperature [7]. From the regression analysis of their data set, they obtained best-fit correlation between ignition delay time and experimental variables. Lieuwen et al. investigated the impact of syngas composition on the four combustor operability issues: blowout, flashback, combustion instability and autoignition by analyzing calculation results of CHEMKIN program [10]. Giles et al. investigated the NO_x emission characteristics of syngas mixtures with airstream dilution of H_2O, CO_2 and N_2 in a counter-flow diffusion flame. The NO_x reduction effect of dilution was found to be $H_2O > CO_2 > N_2$ in order [13]. Such scientific findings from these fundamental researches has provided useful insights and information which can be used when analyzing results of advanced studies and enable rather economic approach when understanding the combustion phenomena in syngas combustor before conducting complicated test of real scale engine. On the other hand, as a latter group, many advanced researches have been conducted at even great expenses to evaluate combustion performance of syngas combustor and to investigate syngas combustion characteristics at gas turbine-like environment. Littlejohn et al. conducted combustion test on a prototype injector of Taurus 70 engine for various syngas compositions and determined the lean blow-off limits, log-linear dependency of NO_x and turbulent flame speed correlation using PIV data [15]. Dodo et al. investigated the performance of a multiple-injection dry low NO_x combustor with hydrogen-rich syngas fuels and reported the effectiveness of convex perforated plate swirler on enhanced cooling of the combustor liner and suppression of combustion oscillation and NO_x [16]. Through combustion test of one can combustor of heavy duty gas turbines, Hasegawa et al. reported many useful results concerning NO_x/CO emission, pattern factor, combustion efficiency and thermal efficiency [17-19]. Lee et al. also tested one can combustor of GE7EA gas turbine

combustor and reported combustion performance characteristics of H_2/CO syngas and the effect of N_2, CO_2 and steam dilution on them [20, 21]. On a mass basis, 40% dilution of N_2, CO_2 and steam reduced NO_x emission by 79%, 88% and 95% respectively and the NO_x reduction per unit power was logarithmically related to diluent's heat capacity. These results of dilution effect are described in detail in chapter 4 to give more understandings of nitrogen dilution effect on the Taean and Buggenum syngases.

Although above mentioned practical studies achieved technical progress in syngas turbine combustion, many unsolved problems on syngas turbine combustion remains due to the highly nonlinear behavior of combustion characteristics according to the syngas composition, combustor geometry and test conditions. On top of that, the knowledge of the syngas combustion in commercial gas turbine is mostly confined to commercial gas turbine makers such as GE and Siemens and the operators of existing plants. Therefore, motivated by this consideration, we tested H_2/CO/CH_4 syngas to obtain broad understanding of combustion characteristics at gas turbine relevant condition.

Firstly, in chapter 3, the effect of fuel composition on combustion characteristics including combustion instabilities, NO_x/CO emissions, steady/unsteady flame structures and temperatures at combustor liner, nozzle and exit are investigated when varying content of H_2, CO and CH_4 from 0% to 100% respectively of which compositions have not been tested in gas turbine model combustor due to the failure from flashback. It is true that much advancement has been made in knowledge of CI mechanisms such as flame-vortex interaction [22, 23], continuous feedback of oscillations among acoustic pressure, equivalence and heat release [24, 25], entropy perturbation [26, 27], processing vortex core (PVC) [28, 29], interference between acoustic and convective disturbances [30], and temporal fluctuation of swirl strength [31-33]. On top of that, with advances in optic measurements such as high-repetition high-power laser, high-speed intensified CCD camera and their utilizing technics, new findings on high-speed interaction between flame and flow have being been reported [28, 34, 35], and useful CI analysis methods including proper orthogonal decomposition (POD) [34-36], time-lag analysis (TLA) [37, 38], flame transfer function (FTF) [39, 40], flame describing function (FDF) [41, 42] and spatio-

temporal Rayleigh index [36, 40, 43, 44] have been introduced and gradually progressed. However, there remains a subject of great interest and some controversy, since it is almost impossible to derive a universal mechanism for the interpretation, control and prediction of complex unsteady combustion physics [45, 46] and the application of CI mechanism can be varied for combustor geometry, combustion methods and fuels. Recently, with increasing concern on the integrated gasification combined cycle (IGCC) and synthetic natural gas (SNG), new CI characteristics on syngas containing various compositions of H_2, CO and CH_4 have been reported [17, 36, 37, 47-50]. Some of them are conducted in lean-premixed (LPM) combustor because it is original designed for CI researches of methane and then just changed fuel, so very limited results from high hydrogen content (HHC) fuels are published. Otherwise, Allison et al. [43] utilized the partially-premixed (PPM) gas turbine model combustor (GTMC) which is modified version of LPM GTMC developed at DLR Stuttgart by Meier and investigated CI characteristics of syngas up to 45 mole% H_2. As another good manner to burn HHC fuel, low swirl injector (LSI) is utilized by Davis et al. [36] and compared thermo-acoustic coupling mechanisms of pure CH_4 and syngas of 90 mole% H_2 and 10 mole% CH_4. Since mostly used combustion concept in syngas turbines to handle the high flame speed and CI of HHC fuels, the present study also used the PPM GTMC combustion concept.

The new aspects of the study in chapter 3, differentiated from other CI researches, are the following. (1) While most researches are tested syngas up to 90 mole% of H_2 (Davis et al. < 90% [36]; Allison et al. < 45 % [43]; Dodo et al. < 65 % [47]; Hasegawa et al. < 30 % [17]), this study observed full trends according to the fuel composition of H_2/CO/CH_4 and singular behaviors of 100% H_2 or CO are discussed. Especially, for CO, to overcome the contamination problem of quartz combustor wall, preventing laser diagnostic measurements [51, 52], cold trapper was implemented by immersing condensation coils in a -30 ^{o}C ~ -60°C alcohol bath. Thus flame was clearly visualized even in high content of CO by eliminating carbonyl compounds such iron pentacarbonyl and nickel tetracarbonyl though this condensation/solidification process. (2) At the compositions of high H_2/CH_4 (>77.5% by LHV) and low CO (<12.5% by LHV), natural

high longitudinal mode CI, most of which does not contain fundamental mode, is generated at frequency of 500Hz, 750Hz and 1000Hz corresponds to 2nd , 3rd and 4th longitudinal mode respectively. To determine the reason that syngas causes these high mode CIs and to characterize them, measurements were taken of OH^* planar laser induced fluorescence (PLIF) and phase-resolved high-speed images of OH^*-chemiluminescence at the rate of 12.5kHz and proper orthogonal decomposition (POD) analysis, Rayleigh index (RI) map are characteristic time scales are introduced. (3) At some particular compositions of $H_2/CO/CH_4$, multi-mode CI (e.g. 3rd, 4th and 6th modes are generated simultaneously) is observed, as similarly previously reported phenomena of self-excited CI of multi-mode [53] or transition from fundamental mode to its higher harmonic mode [54-56]. In these cases, general time-lag analysis with 1-dimensional thin flame assumption or approximation to single mode is not appropriate since p' is not simply sinusoidal but largely distorted. Thus, as a new approach of TLA, time scale of skewness ($\boldsymbol{\tau}_{skew}$) is introduced to precisely analyze the multi-mode CI. (4) All tests are conducted by thermal power (P_{th}, equivalent to heat input) ranging between $30kW_{th}$ and $60kW_{th}$, since operation variable of gas turbines are based on the lower heating value (LHV), not equivalence ratio. Moreover, a PPM GTMC, which is scaled-down model combustor of a GE7EA gas turbine combustor, is utilized to give more practical information for the syngas turbine industries. Combustor liner temperature, NO_x/CO emission, the results are also mentioned using ternary for $H_2/CO/CH_4$ but as much as the CI results which is the most critical issues in gas turbine industries.

Secondly, in contrast to chapter 3, diluents effects on the NOx emission is closely investigated in chapter 4, because dilution technique is mostly used for NOx reduction in IGCC plants. The syngas that is fed to the gas turbine is mainly composed of hydrogen, carbon monoxide, nitrogen, carbon dioxide, and steam. Most of their combustion systems use wet low NO_x (WLN) and/or steam/nitrogen dilution technologies to control NO_x emissions and flash back because the flame temperature and burning velocity of H_2 and CO fuels are much higher than CH_4, which is major component of natural gases. This means flash back and NO_x emission problems can frequently occur if dry low NO_x (DLN)

technology is introduced to the syngas turbine [5, 9, 19]. Therefore, most existing IGCC plants use a syngas saturator and nitrogen injection technology for the lower flame temperature, resulting in lower thermal NO_x emissions as well as preventing burn-out failure of the fuel nozzle and combustor liner [57]. The diluents in the syngas such as nitrogen, carbon dioxide, and steam are very effective in enhancing the combustion performance, yet the level of their effectiveness and the reasons for it are not sufficiently understood. Some numerical and experimental studies about the dilution effect of carbon dioxide and nitrogen were conducted [4, 13, 58], but they either focused on the fundamental combustion characteristics using basic burners such as jet, Bunsen, and counter flow burners, or the measurements were somewhat restricted and were not well proven in the case of commercial-scale gas turbine combustors. No published study has investigated the dilution effect of N_2, CO_2, and steam on H_2 and CO combustion by comparing each dilution gas, even though they are major components of synthetic gas. In this chapter, a broader understanding of dilution effects on the gas turbine combustion performance of H_2 and CO syngas and correlation between diluent heat capacity and NO_x reduction is provided from lots of experimental data.

Thirdly, the test results at the syngas composition of commercial syngas including coal gases and SNG are described in chapter 5. The Korea first IGCC project (net power output: 300MW_e, plant site: Taean) was launched in 2006 and is expected for the completion toward the end of 2015 [59]. In this chapter, for the better operational availability and combustion optimization of this plant, Taean syngas was tested to quantify the potential applications problems and to evaluate the combustion performance as a gas turbine fuel. In particular, compared are the results of the Taean syngas in the views of flame stability, thermo-acoustic combustion instability, NO_x/CO emission, combustion efficiency, flame structure with the syngas of Buggenum which uses the same gasification technology of Taean: SCGP (Shell Coal Gasification Process). The ultimate goal of the study in chapter 5.1 is to provide appropriate solution of syngas combustion issues and to contribute improvement in the efficiency and reliability of the Taean IGCC through understanding syngas combustion characteristics.

Not only IGCC, but also synthesis fuels from gasification such as dimethyl ether (DME), methanol, synthetic natural gas (SNG, sometimes known as substitute natural gas) and etc. are gaining more interest even though they are not new technologies. Synthetic natural gas (SNG) or substitute natural gas production is especially promising since it can utilize the well-organized natural gas infrastructure such as storage facilities and gas piping grids. As a first trial of SNG production in Korea, Kwangyang SNG project was launched by Pohang Steel Company (POSCO) in 2010 and is scheduled for completion by the end of 2014 [60]. This plant will be capable of producing 0.5 million tons of SNG per year and the produced SNG will be plugged into the national gas grid. It can also generate 92MW electricity when SNG production is not needed. SNG is produced by the methanation process of hydrogen and carbon monoxide as described in Eq. (1.1).

$$CO + 3H_2 \rightarrow CH_4 + H_2O \tag{1.1}$$

In this process, SNG may contain a small amount of hydrogen. Increased repetition and fine control of the methanation process may lead to a higher methane yield, but it will be accompanied by higher price. Thus, in the economic perspective, it is important to understand the effect of hydrogen concentration in natural gas on the natural gas user's facility. Thus the effects of hydrogen in SNG on gas turbine combustion characteristics are investigated in subchapter 5.2. The ultimate aim of this study is to give important information for the establishment of quality standards for synthetic natural gas in Korea.

Numerous studies on the combustion characteristics of methane-based fuel blends have been conducted globally. Petersen et al. investigated autoignition delay time for various methane-based fuel blends in a helium-driven shock tube under gas turbine conditions [61, 62]. They showed that addition of hydrogen reduces ignition intensity and delays ignition time. This means the flashback problem does not seem to be significant in the view of autoignition, at least when firing natural gas of higher hydrogen content in gas turbines. However, as shown in Table 1, since hydrogen burns much faster than methane, flashback from the accelerating effects of hydrogen is one of the key issues in hydrogen-enriched gas turbine combustion.

More practically, Samuelsen et al. [63-65] investigated the effect of methane-based

mixture variations on a gas turbine combustor. They reported the flashback tendency and NOx and CO emission characteristics when varying the hydrogen content of the non-premixed pilot fuel and premixed main fuel. Jones and Leng [66] also studied on the effect of adding hydrogen and propane to the fuel on CO, NO and NO_2 emissions in a natural gas-fired non-premixed pulsed combustor. York et al. [67] successfully demonstrated a multi-tube burner, which uses high hydrogen fuel, achieving one digit NOx and flash back-free performance at F-class burning conditions.

Though many studies on the hydrogen addition to fuel have been performed in both fundamental and practical manner, combustion test of SNG which contains very small levels (0% ~ 5% in volume) of hydrogen has not yet been performed on an industrial gas turbine. The aim of the SNG study is to examine and inform the effect of low hydrogen content in natural gas on the gas turbine combustion performance and ultimately to judge whether retrofitting of any combustor part is necessary for stable and reliable combustion.

Fig. 1.1 Estimated bird's-eye view of Taean IGCC plant [59].

Fig. 1.2 Estimated bird's-eye view of Kwangyang SNG plant [60].

CHAPTER 2
EXPERIMENTAL APPARATUS AND TECHNIQUES

A description of the ambient pressure and high temperature gas turbine model combustor is given in this chapter. First, the flow delivery and metering systems for air and gaseous fuel are presented. Detailed explanation of the gas turbine model combustor designed for this study is described with respect to its function and purpose. Description of data acquisition systems (DAQs) for monitoring flow and data logging systems are followed by a detailed presentation of the optical diagnostic techniques applied to the experimental study of syngas combustion.

2.1 THE GAS TURBINE COMBUSTION TEST FACILITY AND TEST CONDITIONS

For the purposes of this study, an atmospheric pressure high temperature combustion test facility for a 60 kW-scale gas turbine was installed. As shown in Fig. 2.1, this facility consisted of an air compressor, an air heater, a cooling and combustion air feed line, an atmospheric pressure combustor, an external stack with silencer, and a fuel supplying system that can control the flow rate of H_2, CO, CH_4, N_2, CO_2 and steam respectively. Mass flow controller (MFC, Parker Porter 200, uncertainty: ±1% of full range) is used for the control of H_2, CO, CH_4, N_2 and CO_2, and electro-pneumatic positioner (Power-Genex MK-708, uncertainty: ±3% of full range) is used for steam. Fuel gases were provided from each bottle of high-purity feedstock gases (H_2 > 99.95 mol%, CO > 99.95 mol%, CH_4 > 99.9 mol%). These gases were mixed well through the inline static mixer and injected to the combustor through 14 fuel injection holes within the inner side of swirl vanes at 2.7mm upstream of dump plane to make partially premixed flame. Especially, for CO supply, carbonyl trapper was installed to overcome the contamination problem of quartz combustor wall, preventing laser diagnostic measurements [31, 32]. The cold carbonyl trapper was implemented by immersing condensation coils in a -30 ^{o}C ~ -60°C

alcohol bath. The solidified or liquefied carbonyls such iron pentacarbonyl ($Fe(CO)_5$) and nickel tetracarbonyl ($Ni(CO)_4$) were eliminated though five particle trapper followed by the alcohol bath. Though this condensation/solidification process, the flame could be clearly visualized in even high content of CO. The detailed description on carbonyl trapper is provided in Appendix F.

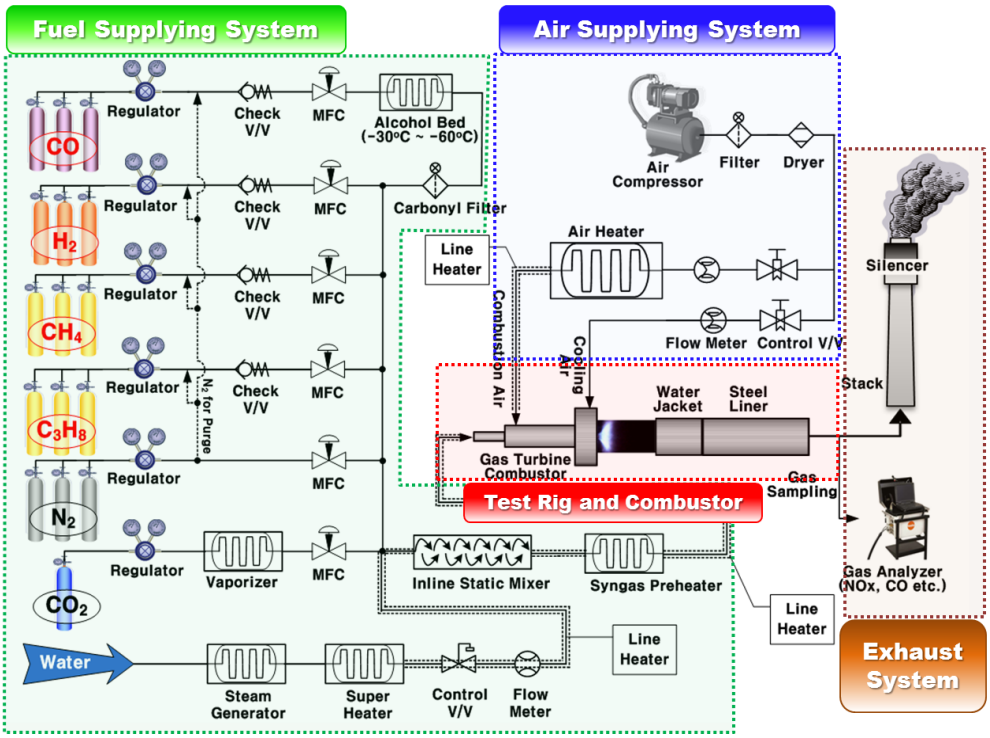

Fig. 2.1 Schematic diagram of the syngas turbine combustion test facility.

To meet gas turbine relevant conditions, dry air at the temperature of 356 °C (±5 °C) was supplied to the flame through a central annular swirling nozzle. The flow rate of combustion air was also controlled by a MFC (Bronkhorst F-206BI, uncertainty: ±0.8% of full range) and choke orifice is installed at the immediately upstream of the combustor to prevent the perturbation of supplying air by blocking the influence of pressure variation at the upstream flow. As shown in Table 2.1, combustion tests were conducted at slightly aviated pressure (1.1~1.4 bar) since 90% area of combustor outlet was blocked by

water-cooled plug nozzle, shown in Fig. 1b, to form an acoustic boundary of combustion chamber outlet. The combustion air was supplied to the combustor at the rate of 66Nm^3/hr in a dried condition and the quartz liner cooling air was also supplied at the identical flow rate with the combustion air. A fuel composition is varies according to the test subject but their heating values were maintained almost constant at every heat input from 30kW$_{th}$ to 60kW$_{th}$ by adjusting the flow rate of each component gases.

According to the fuel and airflow rate, the averaged jet velocity of the fuel–air mixture at the combustor inlet varied from 41.2 m/s to 74.9 m/s, which are almost comparable values with a real engine. The Reynolds number, calculated by the following equation, was maintained between 28,398 and 51,600:

$$\mathrm{Re} = \frac{\rho \overline{U}_{jet} D_h}{\mu} \tag{2.1}$$

where ρ, $\overline{U}_{jet}$, D_h, and μ are density of mixture, jet velocity of mixture, hydraulic diameter at combustor inlet and dynamic viscosity. The turbulent Reynolds number was 45,000–81,000, assuming a relative turbulence intensity of 10% and an integral scale of 1/10 in the chamber diameter. Although chemical reaction times vary significantly according to the fuel composition, the operational points in this research lie between the wrinkled laminar-flame regime and the flame in-eddies regime in the Damköhler-Turbulence Reynolds chart, as in other gas turbines and internal combustion engines [68].

Items	Unit	Value
Combustion chamber pressure	bara	1.1–1.4
Air inlet temperature	^{o}C	200
Mean mixture jet velocity at combustor inlet	m/s	41.2–74.9
Reynolds number	-	28,398–51,600
Swirl number	-	0.832
Heat input	kW$_{th}$	30–60
Overall equivalence ratio	L/L	0.381–0.766

Table 2.1 Baseline operating conditions for this study.

2.2 MODEL GAS TURBINE COMBUSTOR

To examine the combustion characteristics of the syngases, a 1/3 scaled-down one-can dump combustor of a GE7EA gas turbine was designed and fabricated as a test bed combustor. Fig. 2 shows the schematic of the combustion test rig and details of the fuel nozzle. The combustion chamber consisted of two parts. The first part was made from optically accessible quartz, which was cooled by a high-pressure injection of the same amount air as the combustion air, and the second part was made from steel. The inner diameter and length of the combustion chamber was 130 mm and 1410 mm, respectively. As shown in Fig. 2.2a and 2.2b, the fuel–air mixture was supplied through the annularly arranged fourteen swirl vanes of a 45° angle, and fuel was injected within the swirl vanes at 2.7 mm upstream of the dump plane to make a partially premixed flame. The detailed view of fuel-air mixing within the swirl vane is shown in Fig. 2.2d and the direct photo of fuel nozzle is Fig. 2.2e. The inner and outer diameter of each swirl vane was 25.5 mm and 40 mm, respectively, and the swirl number was 0.832, which was calculated via the following equation [69]:

$$S_n = \frac{2}{3}\left[\frac{1-(D_{swirl_in}/D_{swirl_out})^3}{1-(D_{swirl_in}/D_{swirl_out})^2}\right]\tan\theta \tag{2.2}$$

where D_{swirl_in}, D_{swirl_out} and θ are inner diameter of swirler, outer diameter of swirler and swirl vane angle respectively.

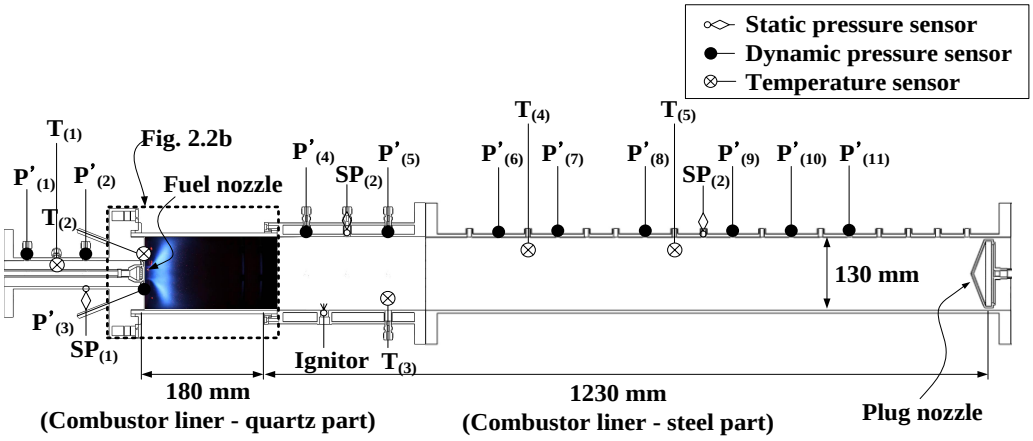

Fig. 2.2a Schematic diagram of the gas turbine model combustor and measurements.

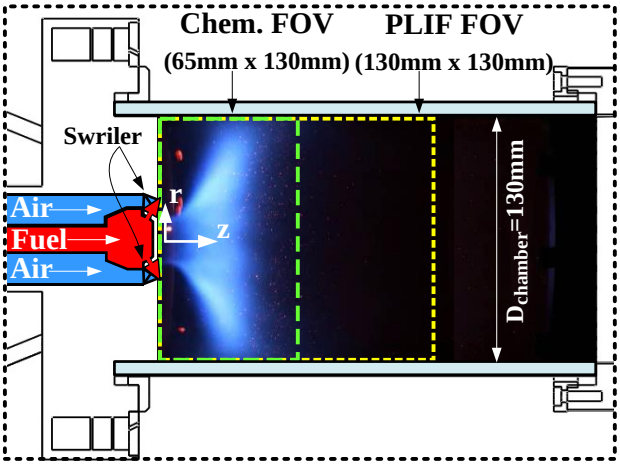

Fig. 2.2b Magnified view of burner head and quartz liner.

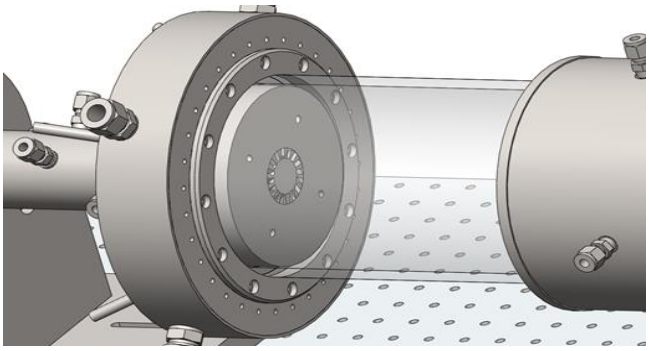

Fig. 2.2c Oblique view of quartz liner and burner head.

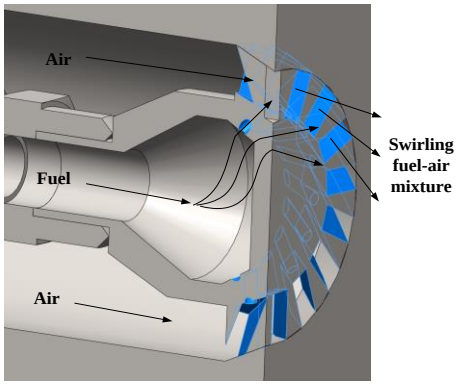

Fig. 2.2d Cross-sectional view of fuel nozzle. Fig. 2.2e Direct photo of tested fuel nozzle.

2.3 MEASUREMENTS AND OPTICAL SETUP

As shown in Fig. 2.2a, eleven piezoelectric dynamic pressure sensors (PCB 102A05), three static pressure sensors, and five k-type thermocouples were installed at the combustor and air inlet line to measure the dynamic and static pressure and temperature of each locations. The flow rates of fuel and air were kept constant for more than at least 100 seconds (sometimes more than test minutes) before data acquisition to achieve steady state value for all measurements. To improve the data acquisition accuracy, the ten-plus data of NO_x and CO, and the temperatures, are measured respectively in the steady-state of each experimental condition before being averaged.

Each dynamic pressure was sampled at a rate of 10kHz using a multi-channel DAQ system, which is simultaneously recorded the camera intensifier trigger for the planar laser induced fluorescence (PLIF) and high-speed OH^*-chemiluminescence. This allowed synchronization of the acoustic and optic measurements. Since the piezoelectric pressure transducers are equipped with the infinite tube, the reflective waves could be prevented and the time lag from the measuring point to the sensor signal was calculated and deduced from the original time series signal by assuming appropriate gas temperature at each test conditions.

Exhaust gas was sampled at the combustor outlet, and the concentrations of NO, NO_2, CO, O_2, CO_2, and UHC were measured by a TESTO 360 gas analyzer. The maximum total accuracy of this analyzer is under 5% of full scale ranges for O_2=0~21vol%, NO=0~3000ppmv, NO_2=0~500ppmv, CO_2=0~25vol%, CO=0~5000ppmv. The measured results for emissions were corrected to 15% oxygen on a dry basis using the following equations [70]:

$$(\mathrm{NO_x\ at\ 15\%\ O_2}) = \frac{(\text{measured NO}_x)}{29.79}\left\{\frac{4.76\times(2-(\text{measured O}_2))}{1-4.76\times(\text{measured O}_2)}\text{-1}\right\} \tag{2.3}$$

$$(\mathrm{CO\ at\ 15\%\ O_2}) = \frac{(\text{measured CO})}{29.79}\left\{\frac{4.76\times(2-(\text{measured O}_2))}{1-4.76\times(\text{measured O}_2)}\text{-1}\right\} \tag{2.4}$$

Combustion efficiency was also calculated to meter the completeness of combustion. Combustion efficiency is defined as the total energy contained per unit of fuel minus the energy carried away by the flue gas and unburned fuel exiting the stack. This can be expressed as following equation:

$$\eta_c\ [\%] = 1 - \left\{ \frac{\text{LHV of unburnt flue gas (CO and UHC)}}{\text{Total LHV of fuel gas}} \right\} \tag{2.5}$$

As shown in Fig. 2.3, PLIF system was set up to measure planar distribution of the OH radical. The triggering laser beam is delivered from Nd-YAG laser (Continuum Surelite I) at 532nm with an 8.5ns pulse served as pumping source for a dye laser (Continuum ND-6000, 532nm→566nm) and then frequency-doubled (566nm→283nm) to excite Q1(6) line of the A-X (1, 0) transition of OH at 282.93 nm. Before contacting to the flame, the beam was formed into a sheet with a height of 200mm and depth 0.5mm using 2 cylindrical lenses. The fluorescence of the OH radical from the A-X(1,0) and (0,0) bands at 306-320 nm was acquired with the optical filters (WG-305 and UG-11) and a UV-Nikkor objective lens (f = 105 mm, f/4.5) mounted on an ICCD (Princeton Instruments, PI-MAX II). This camera setup with the identical filter/lens configurations was also used to obtain the line-of-sight integrated images of OH^*-chemiluminescence, and a three-point Abel-deconvolution scheme was used to extract two-dimensional information from the line-of-sight integrated images.

To investigate the behavior of the unstable flame with proper orthogonal modes (POMs), line-of-sight integrated spontaneous emission of OH^* was imaged separately from the PLIF but under identical test conditions. OH^*-chemiluminescence images were acquired at the rate of 12.5kHz with same arrangement of filter and lens of PLIF but mounted on high-speed intensified CMOS camera (Photron, Fastcam ultima $APXi^2$). The field of view (FOV) for PLIF and chemiluminescence were 130mm×130mm and 130mm×65mm respectively, as shown in Fig. 2.2b. To enhance the uncertainties in PLIF, 100 phase-averaged images are used as a qualitative indicator of the integrated heat

release rate in the combustor.

Figure 2.4 illustrates the timing sequence for obtaining the phase resolved PLIF images. $P'_{(3)}$ used for the synchronization because it is the closest to the flame and antinode of combustor, showing largest amplitude. The raw pressure signal shape of $P'_{(3)}$ is similar to the one shown in Fig. 2.4a. This signal contains high frequency noise which has to be removed before inputting it to the function generator (DG535) so acoustic band pass filter (Krohn-Hite 3362) is utilized to reduce the noise of $P'_{(3)}$. The filtered signal, which is shown in Fig. 2.4b, provided a threshold level for generating the trigger signal (4V, 1ms duration before 111ms time-off) sent to DG535 function generator. Timing setting of DG535 limits the trigger pulse frequency to around 10 Hz because the Nd-YAG laser (Continuum Surelite I) achieves the maximum repetition rate of 10 Hz. Then trigger signal for laser was sent after the delay time of trigger ($\boldsymbol{\tau}_{\text{delay, trigger}}$) and the triggered laser generated beam in time with the laser burst signal. Finally, this signal was shifted in phase from the rising edge of $P'_{(3)}$ to match that in the combustion chamber and used to identify the phase angle in the acoustic cycle at which each optical measurement was recorded. The required delay time from rising edge of $P'_{(3)}$ to laser burst is calculated by dividing periodic time of $P'_{(3)}$ into twelve phases.

After acquisition, acoustic wave propagating time (~0.55ms) from flame to the dynamic pressure sensor of $P'_{(3)}$ is considered for the exact phase matching. Root mean squared (RMS, P'_{rms}) values are calculated in order to investigate the intensity of pressure fluctuations.

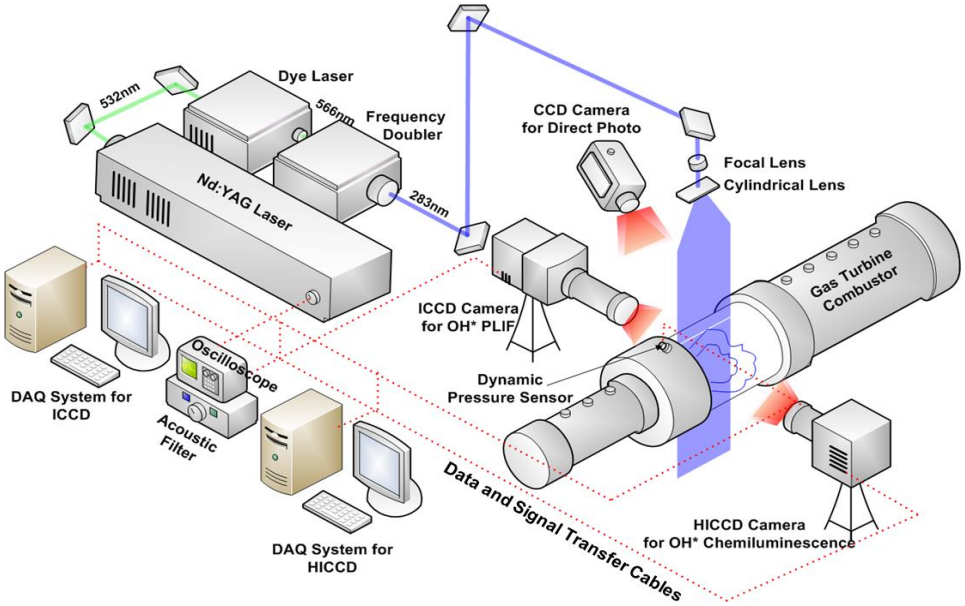

Fig. 2.3 Optical setup for OH^*-PLIF and OH^*-chemiluminescence.

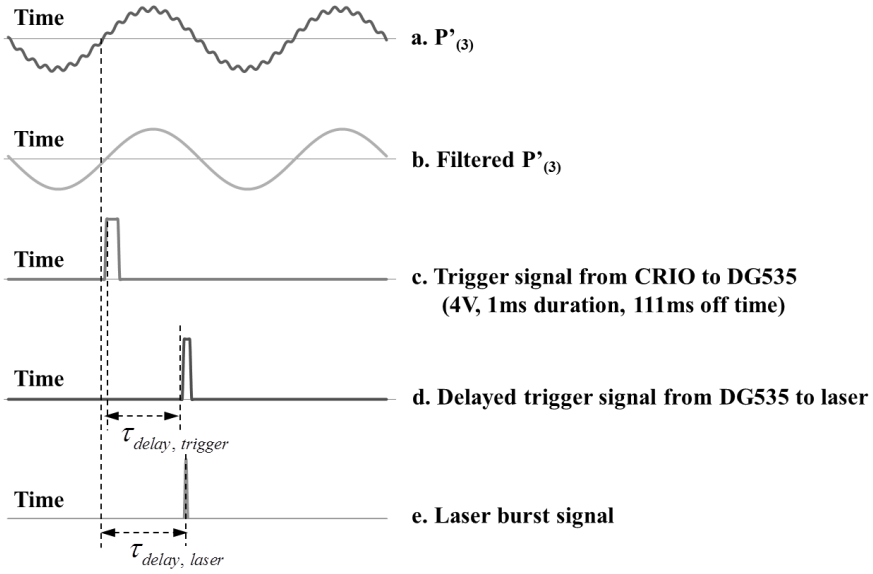

Fig. 2.4 Timing sequences of signals for triggering the ICCD camera for phase-synchronized OH^*-PLIF

CHAPTER 3
COMBUSTION CHARACTERISTICS OF $H_2/CO/CH_4$ SYNGAS

The experimental results from the combustion test of $H_2/CO/CH_4$ syngas are presented in this chapter. First, $H_2/CO/CH_4$ ternary diagrams, which are useful to understand the general trends of fuel effects on combustion characteristics, are presented for NOx and CO emissions, temperature, and combustion instability. Second, the fuel composition effects of $H_2/CO/CH_4$ syngas on the self-excited high multi-mode (mainly 3rd and 4th with their harmonics) combustion instability characteristics have been studied by investigating phase-resolved high-speed OH^* planar laser induced fluorescence (OH-PLIF) and OH^*-chemiluminescence at a rate of 12.5kHz and analyzing the proper orthogonal decomposition (POD), spatio-temporal Rayleigh index (RI), and time-lag. Third, statistical NO_x response model using analysis of variance (ANOVA) is developed for $H_2/CO/CH_4$ syngas from the various composition test results and this model is compared with other NO_x prediction models.

3.1 DETERMINATION OF TEST CONDITIONS

Ternary test conditions of 45 fuel compositions were determined as Fig. 3.1 to understand general trends of combustion performances according to fuel composition of syngas. The compositions of each fuel were varied from 0% to 100% with span of 12.5% by LHV. Test numbers of 1, 9, and 45 in Fig. 3.1a are the conditions of pure CH_4, CO and H_2 respectively and test number 23 is equivalent to the composition of 25% H_2, 62.5% CO and 12.5% CH_4 based on LHV. The combustion tests were conducted in the order of test number for heat inputs of 40kW$_{th}$ and 50kW$_{th}$. Figure 3.1b indicates the ternary test color which corresponds to the test numbers in Fig. 3.1a. This colorization was used to indicate the fuel composition when depicting the test results and test conditions for nitrogen dilutions in chapter 4.

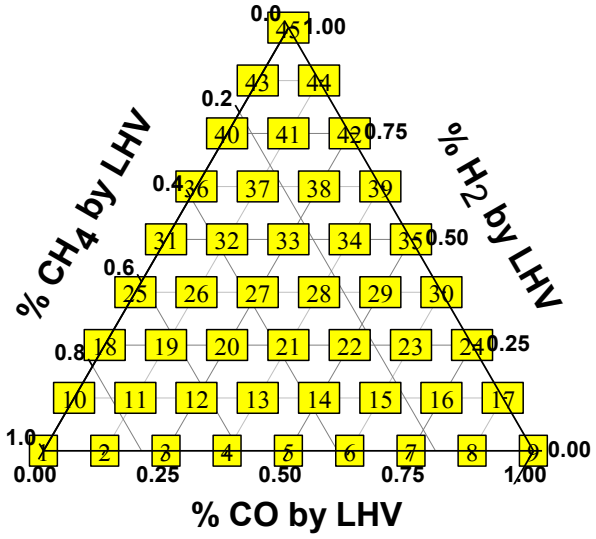

(a) Ternary test matrix and test number

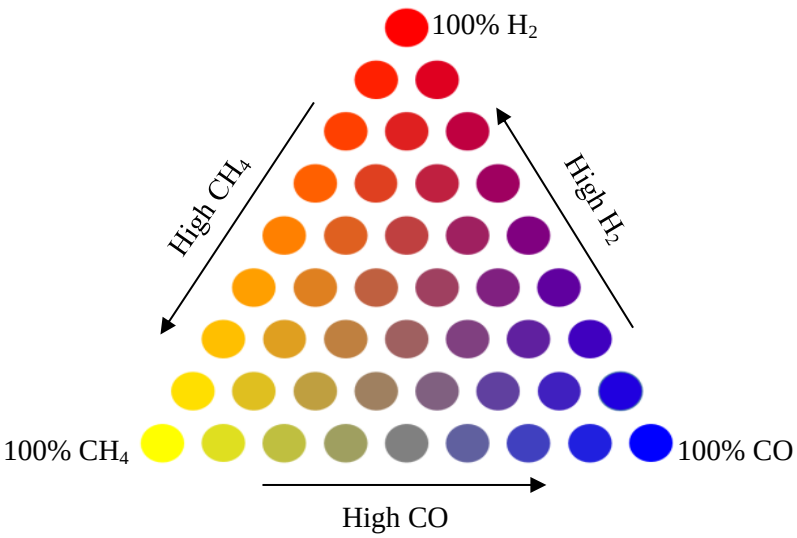

(b) Ternary test colorization corresponding to test matrix

Fig. 3.1 Test conditions of $H_2/CO/CH_4$ syngas combustion.

3.2 TEST RESULTS OF TEMPERATURE, COMBUSTION INSTABILITY, NO_X AND CO EMISSIONS AND FLAME STRUCTURE

3.2.1 Temperature characteristics

Figure 3.2 presents the ternary plots of adiabatic flame temperature (T_{ad}) and combustor liner temperature (T_3) for heat inputs of $40kW_{th}$ and $50kW_{th}$. The T_{ad} was calculated via CATERA code with the GRI 3.0 mechanism. The detailed calculation procedure with Matlab code is provided in Appendix A. Both T_{ad} and T_3 at $40kW_{th}$ was higher than $50kW_{th}$ by more than 200^oC due to the increase in equivalence ratio (φ). It is also notable that T_3 as well as T_{ad} varies significantly according to the fuel composition. The maximum adiabatic flame temperature of H_2 and CO is higher than that of CH_4 by 200^oC as shown in Table 3.1, but Figs. 3.2a and 3.2b show the almost linearly decreasing tendency from high CH_4 condition to high CO condition. This tendency is also due to the decrease in overall equivalence ratio which varies according to the fuel composition. For $40kW_{th}$ heat input, the φ changes from the maximum 0.58 at test number 1 via medium 0.48 at test number 45 to minimum 0.41 at test number 9. This trend is identical for the trend of T_3 at only $40kW_{th}$ for the same reasons. However, high temperature zone was appeared in high CO conditions at $50kW_{th}$. This might be due to the characteristics of CO flame shape which is very long enough to reach measuring point of T_3 and this flame shape will be discussed in subchapter 3.2.4. As shown in Table 3.1, CO reaction is very slow so the burning velocity of CO is significantly lower than methane whereas highly reactive H_2 burns much faster than and CH_4. Thus, T_3 of short H_2 flame is lower since the flame is far from the measure point of T_3. The hotter CH_4 flame losses more heat by the radiative and convective heat transfer though quartz liner so T_3 of higher CH_4 is lower than that of other compositions. Therefore, it can be concluded that the combustor liner temperature is affected by the fuel composition since it changes flame shape and amount of heat loss as well as adiabatic flame temperature.

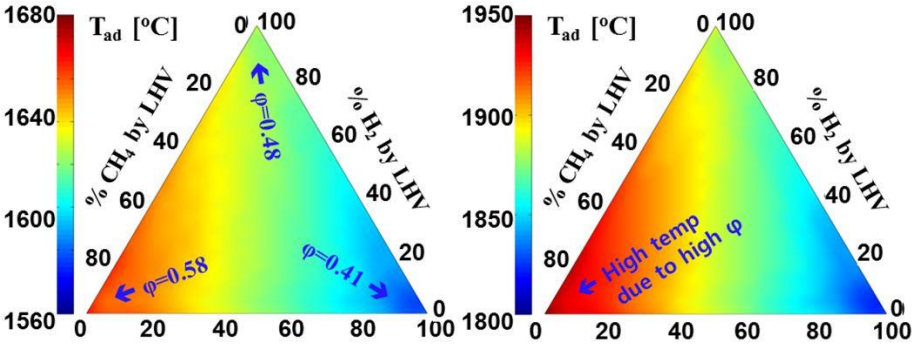

(a) Adiabatic flame temperature at $40kW_{th}$ (b) Adiabatic flame temperature at $50kW_{th}$

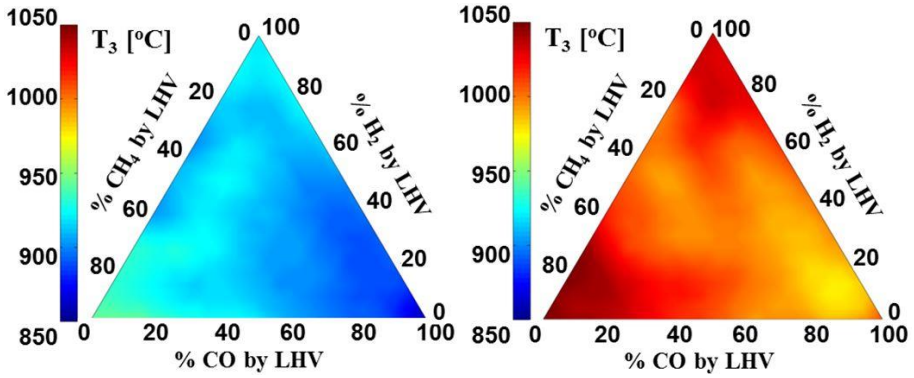

(c) Combustor liner temperature at $40kW_{th}$ (d) Combustor liner temperature at $50kW_{th}$

Fig. 3.2 Temperatures of adiabatic flame and combustor liner at $40kW_{th}$ and $50kW_{th}$.

3.2.2 NO_x and CO emission characteristics

Figures 3.3 and 3.4 show NO_x and CO emissions for $H_2/CO/CH_4$ syngas. The syngas containing high H_2 and CO emits NO_x above 20ppm, the strictest regulation in Korea. As increasing the thermal loads more NOx is emitted due to the higher flame temperature resulted from the higher φ. This phenomenon can be explained by introducing the Zeldovich NO_x mechanism which dominates the NO_x emission in lean partially-premixed flame as well as lean premixed flame [72]. According to this mechanism flame temperature and residence time is vital factor in thermal NO_x formation.

$$\frac{d[NO]}{dt} = 2k_{1,f}[O]_{eq}[N_2]_{eq}, \quad k_{1f} = 1.8\times10^{11}\exp\left(\frac{-38,370}{T\ [K]}\right) \quad m^3/kmol\cdot s \tag{3.1}$$

The residence time can be expressed as following formulation [73, 74]:

$$\tau_{res} = \frac{V_{pz}\ P_3}{\dot{m}_{air}\ R_{air}\ T_3} \tag{3.2}$$

where V_{pz}, P_3, $\dot{m}_{air}$, R_{air} and T_3 are volume of the primary zone [m^3], combustion chamber inlet pressure [Pa], mass flow rate of air [kg/s], ideal gas constant for air [J/kg-K] and combustion chamber inlet temperature [K] respectively. The reasons of this high NOx formation in high H_2 and CO flame can be inferred from the flame structure which gives intuitive information on the fuel-air mixing and residence time in the flame. Since the V_{pz} is highly correlated with flame shape, OH^*-chemiluminescence images and their Abel-deconvoluted images in Fig. 3.6 are closely observed. Highly reactive H_2 flame (test number=45) is appeared to be burnt very shortly and diffusively which resulting the flame temperature enough high to produce high NO_x. Otherwise, CO (test number=9) burns very slowly, so the flame distributed very largely hence resulting long residence time in flame. Even though flame temperature is not high, high NO_x in CO flame might be attributed to the long residence time in flame. In the case of CH_4 (test number=1) of which flame is neither short nor long, the reaction zone is located at the outer recirculation zone (ORZ) where the mixture burns after enough fuel-air mixing which results in the low flame temperature with the low NOx emission.

In all test cases without 100% CO, the CO emission is under 5ppmv, corrected by 15% oxygen in exhaust gas i.e. over 99.9% combustion efficiency. This high CO emission is the distinctive characteristics of slowly burning CO flame which also results in long and broad flame shape. Theoretically, the oxidation of CO can be activated when even small amount of OH* exists. Thus, 100% CO cannot be burnt at all but CO flame exists in this experiment because a small amount of hydrocarbon are estimated to be contained in feedstock gases as considering the purity of fuel gas is 99.5%. As increasing the heat input, CO emission is reduced due to the elevated mixed mean T_{ad}.

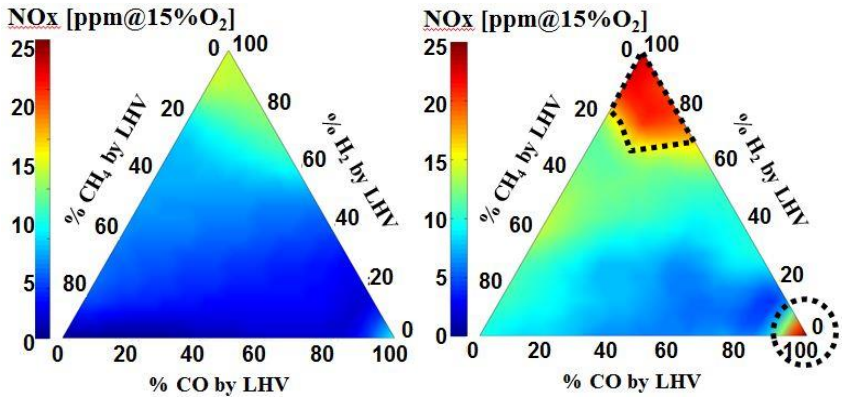

Fig. 3.3 NOx emission at (a) 40kW$_{th}$ (left) and (b) 50kW$_{th}$ (right).

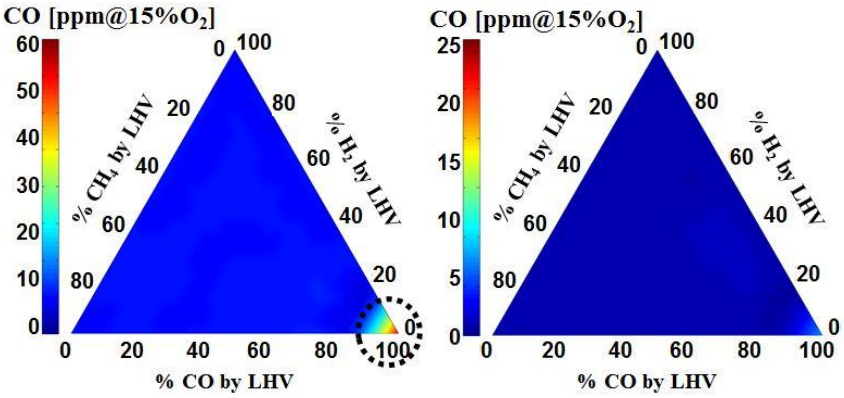

Fig. 3.4 CO emission at (a) 40kW$_{th}$ (left) and (b) 50kW$_{th}$ (right).

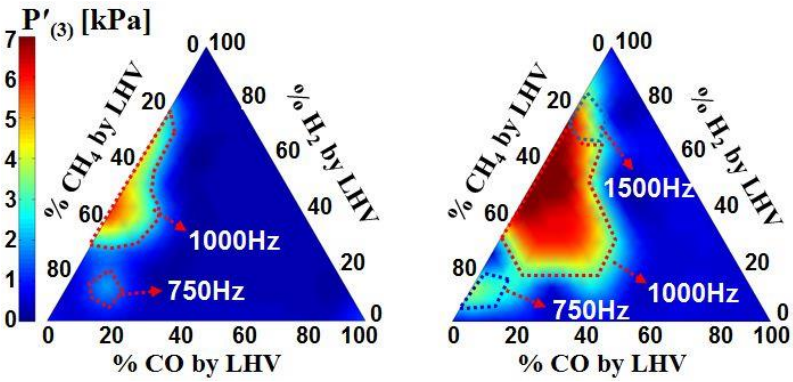

Fig. 3.5 RMS of P'$_{(3)}$ at (a) 40kW$_{th}$ (left) and (b) 50kW$_{th}$ (right).

3.2.3 Combustion instability characteristics

Figure 3.4 illustrates the combustion instability results for $H_2/CO/CH_4$ syngas at $40kW_{th}$ and $50kW_{th}$. For $40kW_{th}$, high combustion instability was generated from the H_2/CH_4 flame and as increasing the heat input, the intensity is amplified and unstable region was enlarged to some extent of CO containing fuels. This phenomenon can be simply explained by introducing Rayleigh criterion [75]:

$$\int_V \int_T p'(x,t)q'(x,t)dtdv \geq \int_V \int_T \sum_i L_i(x,t)dtdv \tag{3.3}$$

where p', q' and L_i are instantaneous pressure fluctuation, instantaneous heat release rate and i-th damping coefficient such as viscous dissipation. As easily expected, the increased heat release from the addition of heat input plays the role of combustion instability driving. On the other hand, no combustion instability was generated for H_2/CO flame CO/CH_4 flame over all heat inputs. One of the main reasons of this combustion instability phenomenon might be the combustion property of H_2 which cannot be easily extinguished due to large flammable limit and high flame extinction stretch rate [20], thus breaking the feedback loop among pressure fluctuation, heat release fluctuation and equivalence ratio fluctuation. Another reason can be raised from the flame structure in Fig. 3.6 which changes largely according to fuel composition. As increasing H_2 in CH_4 or CO flame (Figs. 3.6a-3.6b), enhanced reactivity caused flame short and narrow, and this resulted in the low probability of flame/vortex interaction at outer recirculation zone (ORZ). Due to the same reason, increment of CO in H_2/CH_4 flame at constant H_2 (Fig. 3.6c) caused the flame short and narrow, and thus combustion instability was attenuated. First peak frequency, calculated from the FFT analysis of $P'_{(3)}$, as labeled in Fig. 3.5, was approximately 750Hz, 1000Hz and 1500Hz, corresponds to the 3rd, 4th and 6th longitudinal mode respectively. From the results, it can be concluded that CH_4/H_2 syngas is prone to generate combustion instability and its instability mode and frequency are highly affected by fuel composition. Thus, more detailed investigation on the combustion instability of CH_4/H_2 flame is conducted in the subchapter 3.2 to determine the reason that syngas causes these complex high mode combustion instability.

3.2.4 Flame structures

Figures 3.6 and 3.7 show time-averaged OH^*-chemiluminescence images and their Abel-deconvoluted images at $40kW_{th}$ and $50kW_{th}$. As increasing H_2, enhanced reactivity causes flame more intense but shorter and narrower. Similarly, as increasing CO in H_2/CH_4 flame at constant H_2, the flame appeared to be shorter and narrower. Broadly and long shaped 100% CO flame and short and intense 100% H_2 flame which burns very close to fuel nozzle are also noteworthy. As mentioned previously, these features of flame structure suggested significant information when analyzing the characteristics of combustor temperature, NO_x/CO emission and combustion instability. To investigate high speed flame behavior for high combustion instability conditions, measurements were taken of OH* planar laser induced fluorescence (PLIF) and phase-resolved high-speed images of OH^*-chemiluminescence at the rate of 12.5kHz in subchapter 3.2.

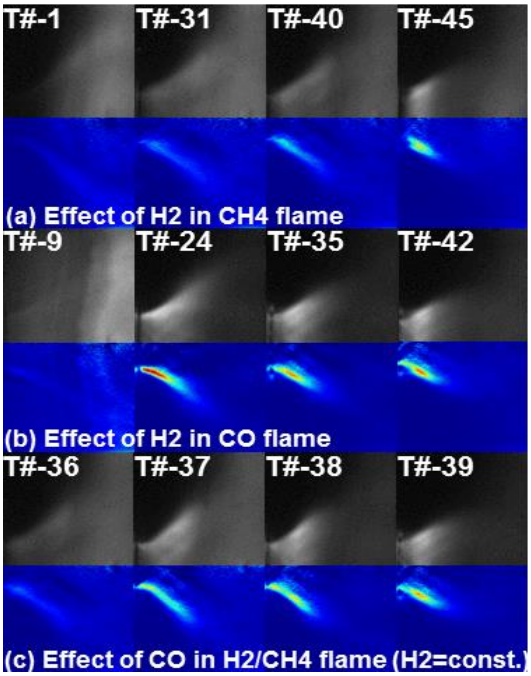

Fig. 3.6 Time-averaged OH^*-Chemiluminescence (upper) and their Abel-deconvoluted images (lower) with the increment of (a) H_2 in CH_4 flame, (b) H_2 in CO flmae and CO in H_2/CH_4 flame. T# indicates the test number in Fig. 3.1.

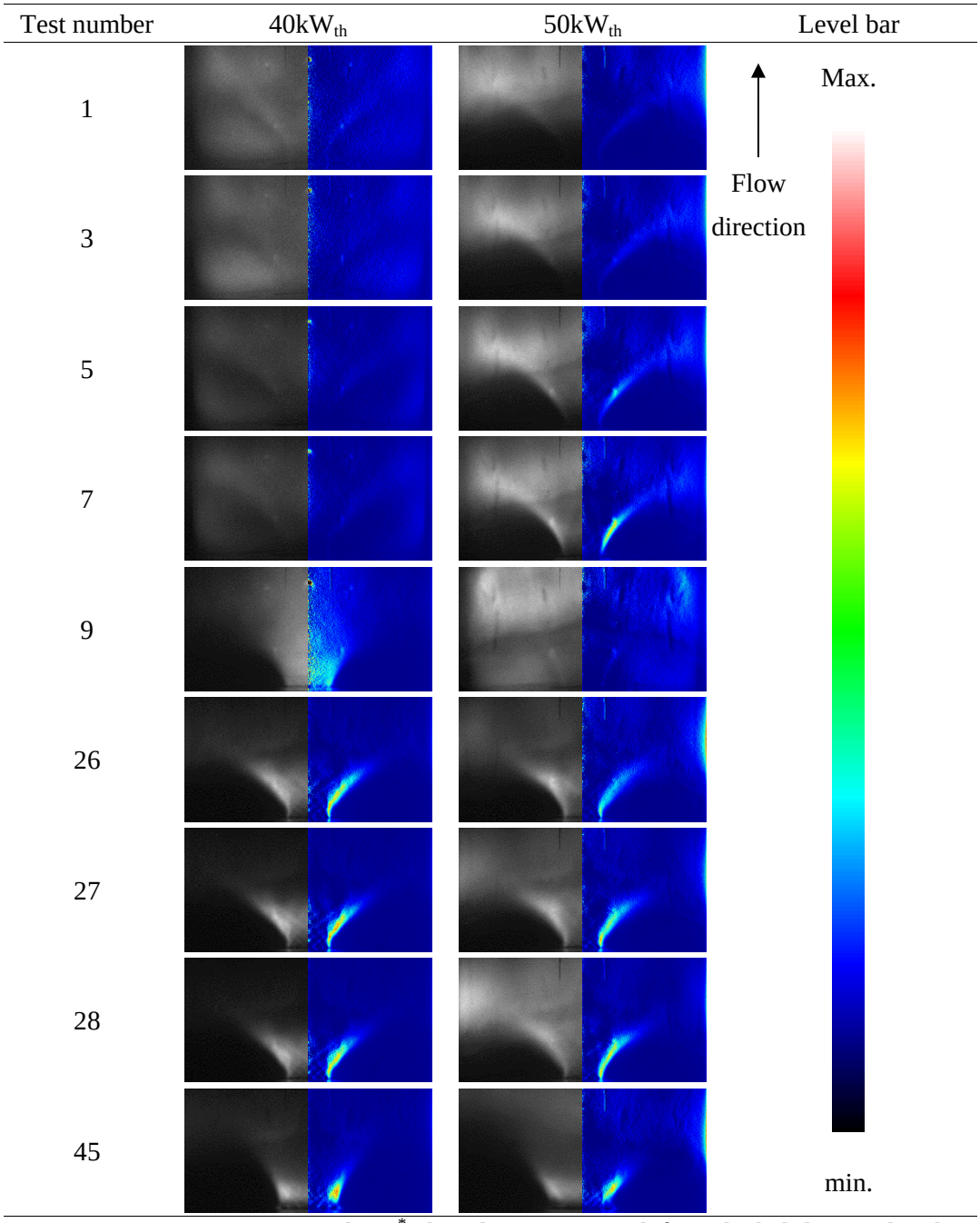

Fig. 3.7 Time-averaged OH*-chemiluminescence (left) and Abel-deconvoluted images (right) at 40kW$_{th}$ and 50kW$_{th}$.

Property	Unit	Hydrogen	Carbon Monoxide	Methane
Chemical formula	-	H_2	CO	CH_4
Boiling point	^oC	-252.8	-191.5	-161.5
Specific gravity	(vs. air)	0.07	0.97	0.55
Flammable limits in air	%	4-75	12.5-74.2	5.0-15.4
Auto-ignition temperature	^oC	500	609	537
Max. burning velocity	cm/s	289	19	37
Max. adiabatic flame temperature	^oC	2200	2210	2000
Stoichiometric air/fuel ratio	kg/kg	34.1	2.5	16.9
Higher heating value	kcal/kg	33,888	2,415	13,267
Lower heating value	kcal/kg	28,670	2,415	11,955

Table 3.1 Properties of hydrogen, carbon monoxide, and methane [6, 20, 21, 57, 71].

3.3 ANALYSIS OF COMBUSTION INSTABILITY

3.3.1 Frequency and mode analysis

As previously mentioned, high multi-mode self-excited thermo-acoustic combustion instability is generated when combusting $H_2/CO/CH_4$ syngas in a partially-premixed gas turbine model combustor. Figure 3.8 shows the representative pressure fluctuation cycles of 4th ($\boldsymbol{\tau}_{osc}$=0.979 msec, f=1021 Hz, test number=10, $0.125H_2/0.875CH_4$ at 50 kW_{th}) and 3rd ($\boldsymbol{\tau}_{osc}$=1.309 msec, f =764 Hz, test number=31, $0.5H_2/0.5CH_4$ at 50 kW_{th}) modes of which FFTs are plotted in Fig. 3.9. In 3rd mode, the amplitude of the first peak was 2.8

kPa at 764 Hz and the second peak was 1.4 kPa at 1528 Hz, approximately half of the first peak. The superposition of these two waves makes the distorted wave of p' as shown in Fig. 3.8b. Otherwise, in 4th mode, the amplitude of the first peak was 6.4kPa at 1021 Hz and the second was 1.3 kPa at 2042 Hz, approximately quarter of the first peak, so the sum of these waves is less distorted as shown in Fig. 3.8a. Though p' is distorted, q' is not so much as p' since continuous existence of flame and burning of entrapped unburned gas at ORZ appears to restore the distortion to be more sinusoidal. Thus this amplified higher harmonic component alleviates the coupling between the distorted p' and the less distorted q', generating less intense combustion instability like the 3rd mode.

Before conducting combustion instability analysis, basic combustion properties such as laminar flame speed (S_L), ignition delay time ($\boldsymbol{\tau}_{ign}$), and adiabatic flame temperature are calculated using the closed homogeneous reactor model and the flame speed model in the CHEMKIN-Pro program with GRI 3.0 and Aramco mechanisms to understand fuel composition dependence on the frequency and time scale of chemical reaction. The detailed method of calculation with chemical reactor model used for this study is described in Appendices B and C. Figures 3.10~3.12 present the relationship between each two combustion properties. It can be clearly observed that the ignition delay time is inversely correlated with the laminar burning velocity and both properties are highly affected by fuel composition as well as heat input. Especially, the addition of hydrogen decreases ignition delay time and increases laminar burning velocity very much. However, adiabatic flame temperature is affected by only fuel composition rather than heat inputs.

These S_L and T_{ad} for all test conditions were used to understand the effect of these combustion properties on the frequency. As illustrated in Fig. 3.13a, frequency is nearly linearly proportional to the S_L and this tendency coincides with the Allison's results [43]. Since high S_L normally shortens both the chemical reaction time ($\boldsymbol{\tau}_{chem} \fallingdotseq 2\alpha/S_L^2$, α=thermal diffusivity) and flame length (L_{flame}), oscillation period ($\boldsymbol{\tau}_{osc}=1/f$) is also shortened according to the continuous oscillation feedback mechanism (COFM). However, the slop of linear fitting ($\Delta f/\Delta S_L$) and correlation coefficient (R^2) were decreased as increasing mode, meaning less linearly correlated for higher modes because

larger $\boldsymbol{\tau}_{osc}$ of higher modes is less affected by relatively short $\boldsymbol{\tau}_{chem}$ and L_{flame}. Figure 3.13b shows that frequency in each mode is more linearly correlated with T_{ad} than S_L, in contrast to the results of Allison who addressed that ΔT_{ad} is not large enough to explain the significant variation in frequencies. In this study, data from large ΔT_{ad} (≒800°C) and broad frequency bands are included so the relationship between T_{ad} and frequency can be clearly seen with high R^2s. This relationship can be explained by explicit equations of closed-closed system standing wave (f=nc/2L) and sonic velocity ($c=\sqrt{\gamma RT}$). Frequency was logarithmically increased for S_L and T_{ad} throughout all modes and the mode-shift was very sensitive to those two properties. The reason of this mode-shift and non-fundamental mode is discussed by introducing characteristic length and time scales in subchapter 3.3.2 and 3.3.5.

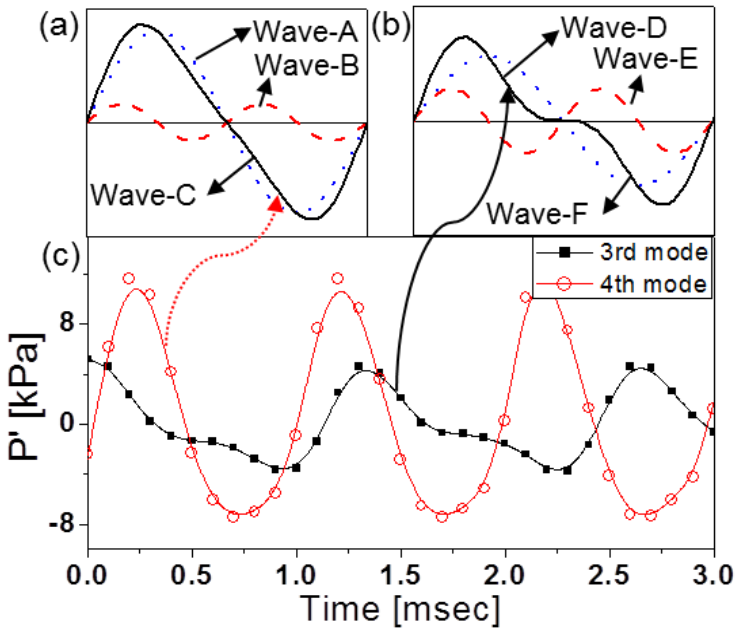

Fig. 3.8 Representative pressure fluctuation cycles of 4th and 3rd mode CIs.

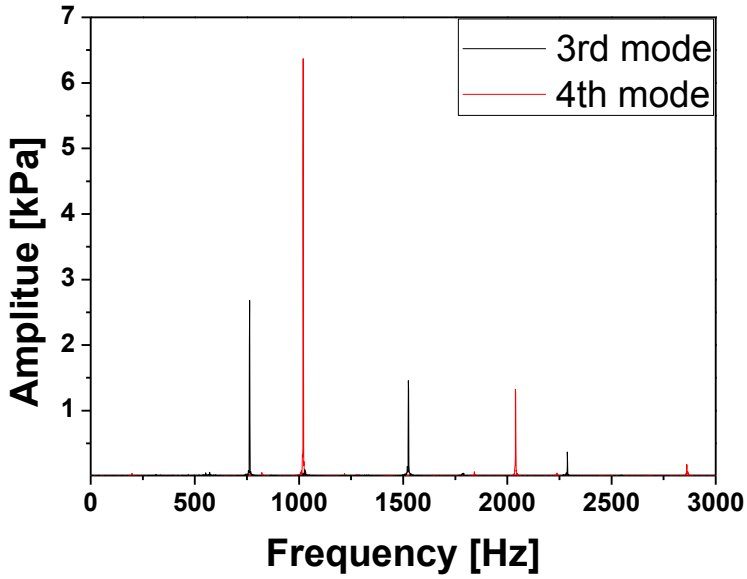

Fig. 3.9 FFTs of representative pressure fluctuation cycles of 4th and 3rd modes.

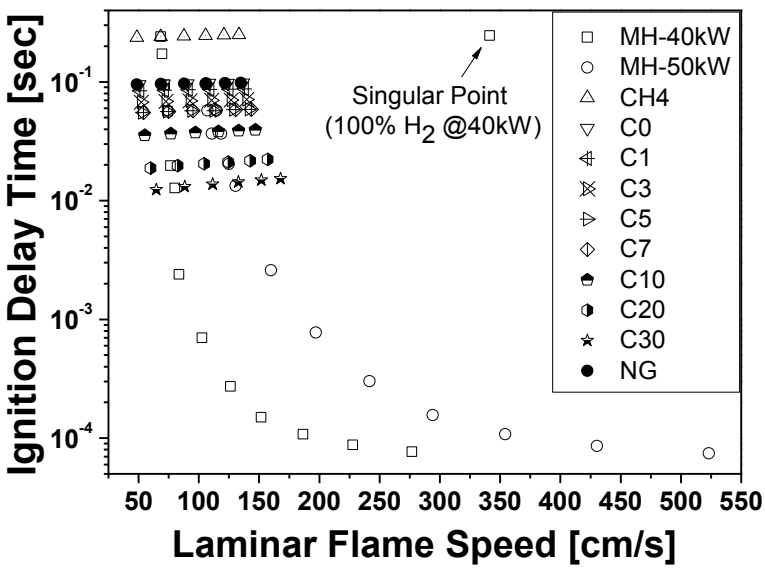

Fig. 3.10 Relationship between S_L and ignition delay time for all fuels studied.

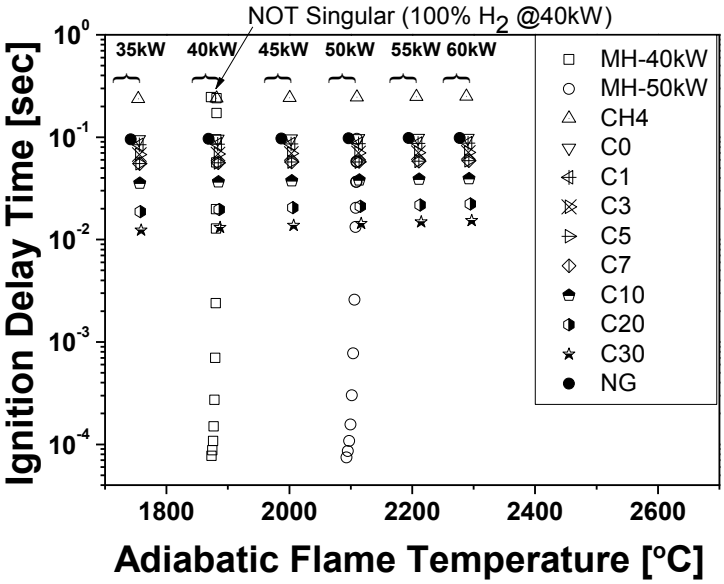

Fig. 3.11 Relationship between adiabatic flame temperature and ignition delay time for all fuels studied.

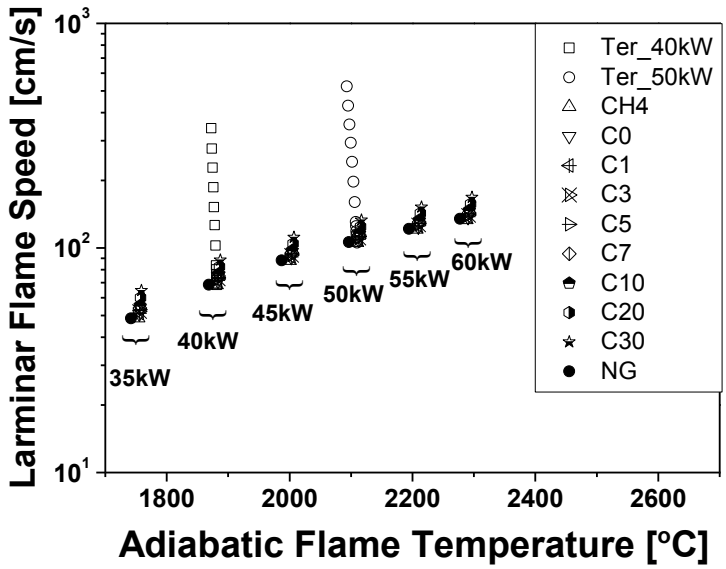

Fig. 3.12 Relationship between adiabatic flame temperature and laminar flame speed for all fuels studied.

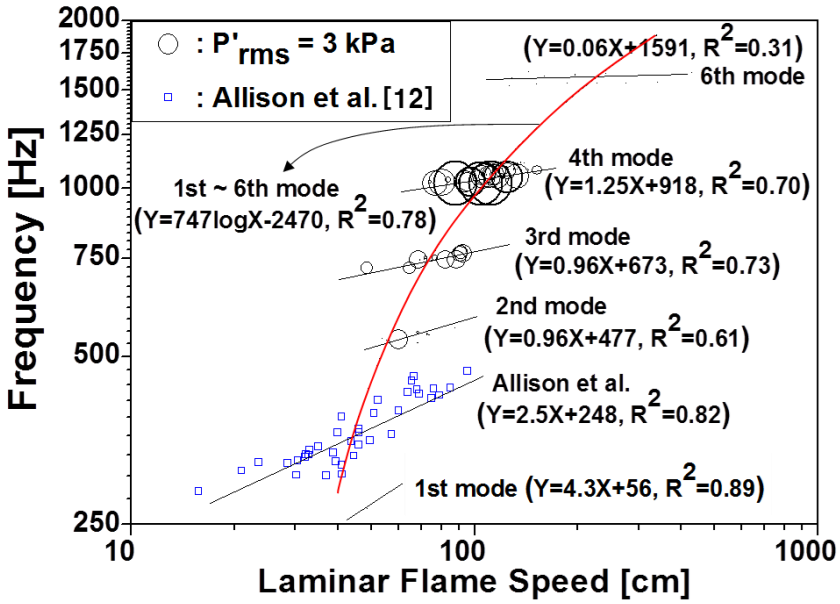

(a) Effect of laminar flame speed.

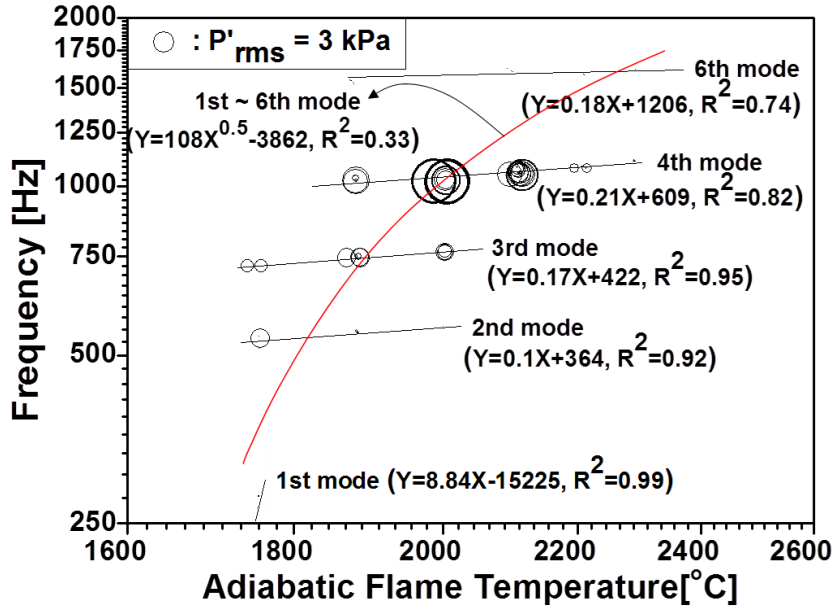

(b) Effect of adiabatic flame temperature.

Fig. 3.13 Effect of laminar flame speed and adiabatic flame temperature on the frequency of the CI for all fuels studied.

3.3.2 OH-PLIF*

Figure 3.12 shows instantaneous and phase-averaged images of OH-PLIF separated by 30° phase-angle (θ) taken during the previously mentioned representative CI cycles of 4th and 3rd modes. In both 4th and 3rd modes, there is a region of q' near the combustor wall at all times which appears to be partly interact with vortices in ORZ, and the portion of flame interact with this vortical flow is maximized at the phase during high q'. The entrapment of a portion of the flame by the ORZ seems to be a critical process in the unstable flame behavior according to FVIM. Although the flame intensity varies significantly, complete extinction of the flame is not observed and this might be resulted from the high reactivity of H_2 containing fuels. In 4th mode, a small flame spot emerges from the nozzle and travels towards the quartz combustor wall. When this spot merges with the reaction zone near the wall, there is a remarkable increase in q'. With this movement, flame attaches and detaches to the center nozzle periodically, and this flame attachment/detachment seems to be significant driving mechanism of CI since it is considered to be initial source of maximum q' in COFM.

Flame ignites and evolves from the inner shear layer of central mixture flow and develops to ORZ (mostly seen in instantaneous images) since fuel is injected inner wall of center swirl vane. (In 3rd mode, intermittent flame evolution from the inner shear layer of central mixture flow was observed.) This is distinguished feature of a PPM-GTMC of which fuel/air mixing length ($L_{mix,PPM}$=2.7mm) is considerably shorter than that of LPM-GTMC ($L_{mix,LPM}$>100mm). Short $L_{mix,PPM}$ with short L_{flame} due to high S_L resulted in short convection time of φ' ($\boldsymbol{\tau}_{conv}$) and acoustic time of p' ($\boldsymbol{\tau}_{acou}$) in both flame and mixing section, and consequently diminishing $\boldsymbol{\tau}_{osc}$ and elevating CI frequency. This also implies L_{flame} plays an important role in determining the CI frequency in a PPM-GTMC since $L_{mix,PPM}$ is quite shorter than $L_{flame,PPM}$ (~100mm) comparing to the LPM-GTMC ($L_{mix,LPM}$>$L_{flame,LPM}$), and this feature also gives the answer to why frequency and mode-shift is very sensitive to fuel composition for which $L_{flame,PPM}$ varies a lot.

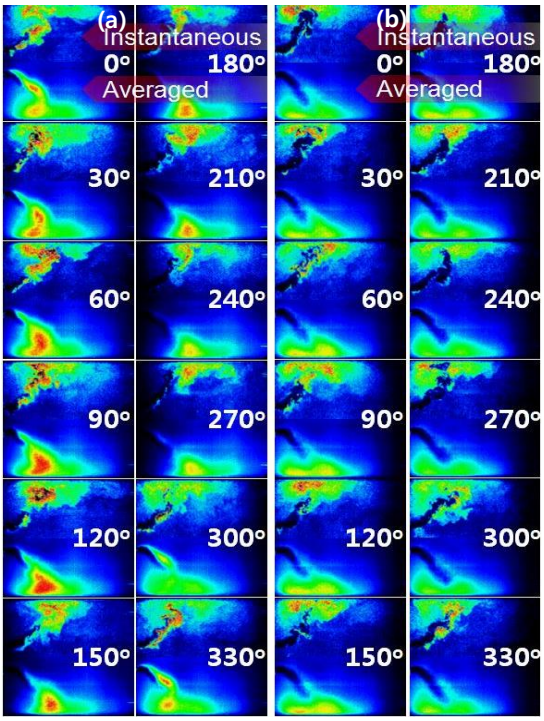

Fig. 3.14 Images of phase-resolved OH*-PLIF for (a) 3rd and (b) 4th mode CIs. (upper half: instantaneous image, lower half: averaged image of 100 instantaneous images)

3.3.3 Rayleigh indices

Spatially global heat release fluctuations (q'_{PLIF} and q'_{chem}) were calculated by averaging and normalizing the intensity from OH*-PLIF and chemiluminescence and depicted with normalized p' in Figs. 3.13a-top and 3.14a-top. As PLIF results are phase-averaged, sinusoidal fitting of normalized q'_{PLIF} are plotted repeatedly for each cycle. As expected, maximum fluctuations in q' and p' coincide temporally, satisfying Rayleigh criterion. While p' lags q' by approximately 30° phase-angle ($\theta_{p'-q'}$) in 4th mode, p' leads q' in 3rd mode but it is hard to determine $\theta_{p'-q'}$ due to the distortion in p' which is formed by the superposition of higher harmonics. In 3rd mode, the amplitude of the first peak was 2.8 kPa at 764 Hz and the second peak was 1.4 kPa at 1528 Hz, approximately half of the first peak. The superposition of these two waves makes the distorted wave of p' as Fig. 3.14a-top. Otherwise, in 4th mode, the amplitude of the first

peak was 6.4kPa at 1021Hz and the second was 1.3 kPa at 2042 Hz, approximately quarter of the first peak, so the sum of these waves is less distorted as shown in Fig. 3.13a-top. Though p' is distorted, q' is not so much as p' since continuous existence of flame and burning of entrapped unburned gas at ORZ appears to restore the distortion to be more sinusoidal. Thus this amplified higher harmonic component alleviates the coupling between the distorted p' and the less distorted q', generating less intense CI like the 3rd mode.

Rayleigh integral is used to identify regions where thermo-acoustic driving and damping occurs.

$$IRI = \iint p'(r,\theta,z,t)\ q'(r,\theta,z,t)dVdt = \iint RI(r,\theta,z,t)dVdt \tag{3.4}$$

Here, RI was calculated using the OH^*-chemiluminescence and longitudinal mode shape of p' in each mode. Figures 3.13b and 3.14b illustrate 2-dimensional RI maps that correspond to instances of CI driving/damping, and Figs. 3.13a-middle and 3.14a-middle show the temporal variation of mean axial RI of which axial integral (IRI) is plotted in Figs. 3.13a-bottom and 3.14a-bottom. The IRI of 4th mode is almost positive, meaning driving the CI stronger than damping, and has two peaks in a cycle meaning frequency-doubled. The first is a strong peak at around $\theta=60^o$ (③ t=0.16msec), which leads the peak of p' because q' leads p' by almost 30° and first peak of p' is slightly distorted towards left. The second is less sharp and looks round because negative peak of q' is less sharp than positive one due to the flame existence of HHC fuels during all the cycle. Contrastingly, the RI of 3rd mode is similar to p', which means RI also fluctuates at the same frequency and amplitude ratio of 3rd mode and 6th mode. Because the flame shapes in Fig. 3.12b do not change so much as intensity, RI maps in Fig. 3.14b reflect mostly the variation in p' without particular changes in shape.

As shown in Figs. 3.13b and 3.14b, driving/damping of CI occurs mainly at the flame so all RI maps are almost symmetric. The strongest CI driving region of mean axial RI in 4th and 3rd is at z=25mm and 35mm respectively because the higher H_2 flame is shorter. The corresponding axial RI distribution has a broad driving region centered at

each maximum driving point. Otherwise, the weakest region is slightly lower and narrower than the strongest region in both modes, meaning damping occurs further downstream and more compactly than the driving region since the flame get shortened during q'<0.

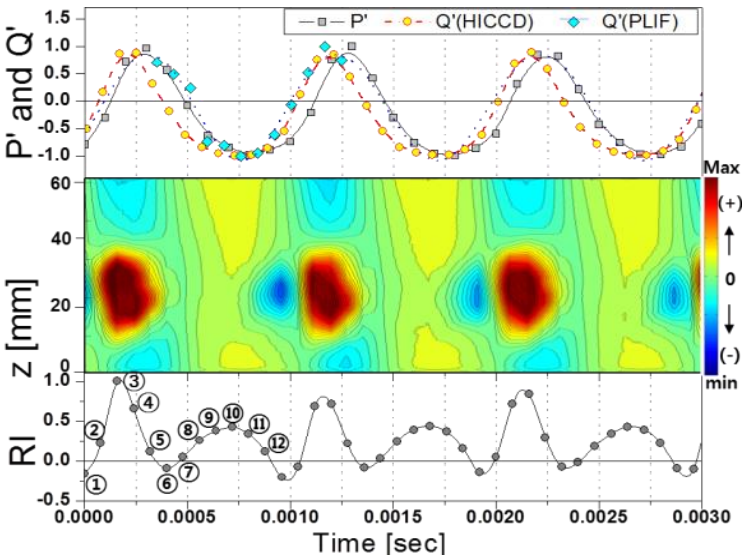

(a) Normalized pressure and heat release fluctuation (top), mean axial RI (middle), and normalized integral RI (bottom) for 3rd mode.

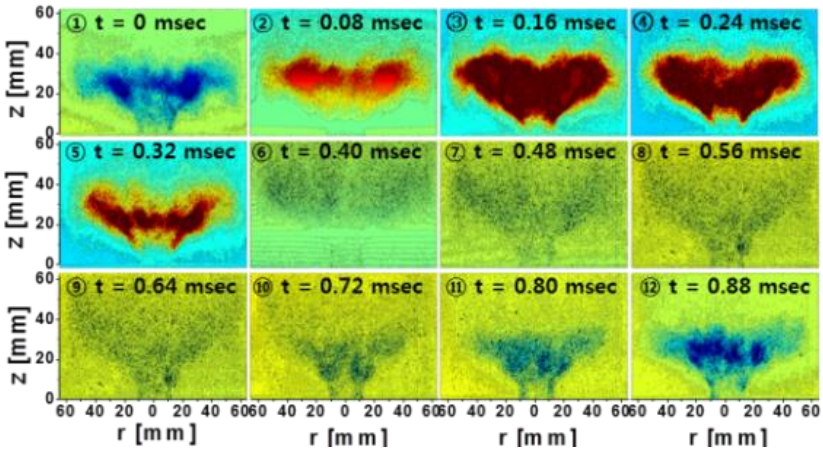

(b) RI maps with corresponding time step of Fig. 3.13a

Fig. 3.15 Temporal variation of normalized pressure and heat release fluctuation and Rayleigh indices for 3rd mode.

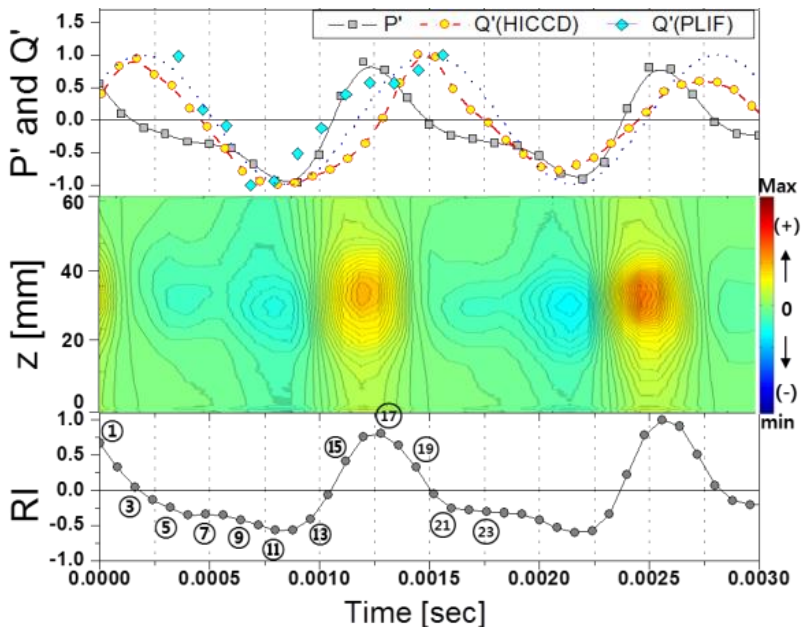

(a) Normalized pressure and heat release fluctuation(top), mean axial RI(middle), and normalized integral RI(bottom) for 3rd mode.

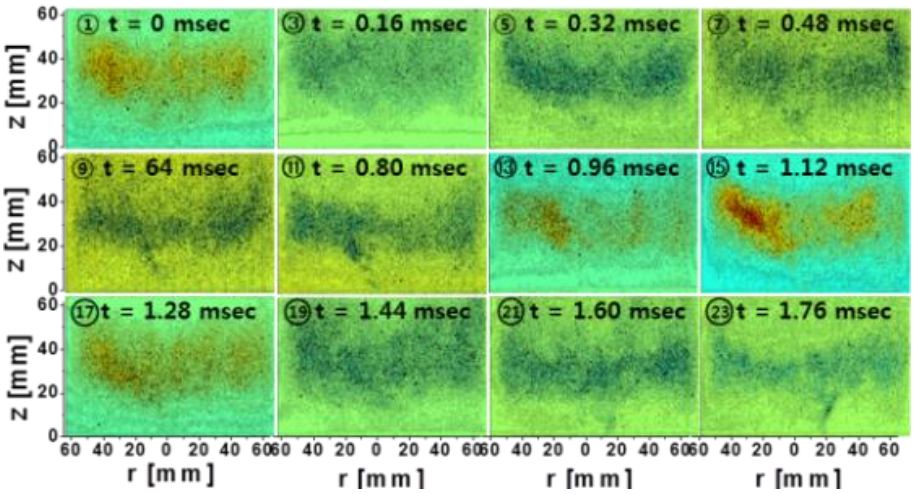

(b) RI maps with corresponding time step of Fig. 3.14c and 3rd mode.

Fig. 3.16 Temporal variation of normalized pressure and heat release fluctuation and Rayleigh indices for 3rd mode.

3.3.4 Proper orthogonal decomposition analysis

Spatially The POD, also known as Karhunen Lòeve expansion, is a method to decompose a set of vector or scalar fields (2D or 3D) into a set of empirical eigenfields, which describes the dominant behavior or dynamics of a given problem. The goal of this technique in the present study is to find a sequence of orthonormal basis functions φ_m (POD modes) representing the coherent flow field and flame structures of unsteady flames. Herein, the construction of the proper orthogonal modes (POMs) was performed by the 5000 instantaneous OH^*-chemiluminescence snapshot images from the HICCD that were used to form an eigenvalue problem of which solution determines a set of optimal basis functions for representing the flame structures. The detailed explanation on the POD used for this study can be referred to Ref. [76].

Figure 7 compares 1~8, 100 and 1000 POMs and their energy distribution for 4th and 3rd modes. The eigenvalues show that there is dominant mode at the frequency (f_D) of 1025Hz and 763Hz equivalent to each CI frequency because highest energy contributed by POM-1 is over 90%. This represents that most of energy is focused on the major first POM although CI have multi-mode characteristics. The dominant POM shapes present that the thermo-acoustically coupled q' in both flames are associated with the large roll-up flame structures. In 4th mode, cross-correlation of coefficients (RR) between two sets of coefficients of POM-1 and POM-4 was 71.4% with a phase difference (θ_{RR}) of 117.6^o and RR of POM-2 and POM-3 was 75.4% with -29.4^o θ_{RR}. This implies that the each two modes form a pair, to indicate a convective behavior of the unstable flame structures. POM-1~POM-4 are axisymmetric but POM-5~POM-8 are asymmetric, to indicate a swirl-like behavior. POM-2 and POM-3 have the harmonic frequency (2050Hz) of POM-1 and their contribution in total energy is 1.2% and 0.86%. Otherwise, RR in 3rd mode also showed that POM-1 is weakly correlated with POM-2 (θ_{RR}=-176°) and POM-3 is correlated with POM-5 (θ_{RR}=44°). Energy fraction of asymmetric modes (POM-2~POM-5) are increased showing the magnification of axially-alternative flame motion like swirl. For both CI modes, as increasing POM number, scale of coherent structure appears to be

smaller with lower fraction of energy content and no pairing was found.

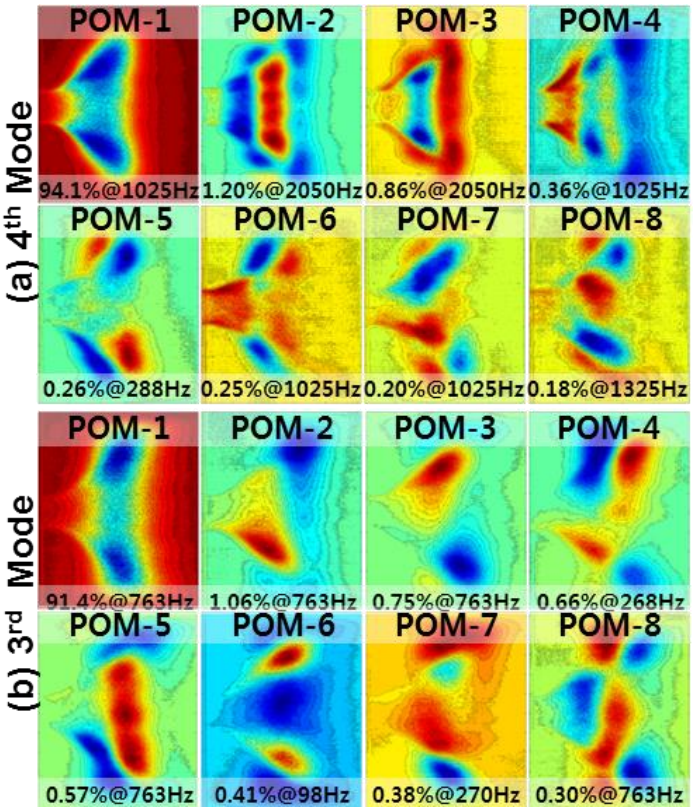

Fig. 3.17 Mode shapes from POD analysis of 3rd and 4th mode CIs with corresponding frequency and fractions of their energy level.

3.3.5 Time-lag analysis in multi-mode combustion instability

To give an answer to how these high multi-mode CIs are generated, time-lag analysis based on the feedback mechanism among p', φ' and q' was performed since φ' plays an important role in a PPM GTMC of which fuel injector is unchoked. As a first step in developing time-lag analysis, evolution of pressure disturbance in a GTMC can be modeled in terms of characteristic time scales as shown in Fig. 8: (a) p' is occurred at flame with periodic time of $\boldsymbol{\tau}_{osc}=1/f$; (b) this p' propagates from flame to the fuel injector ($\boldsymbol{\tau}_{acou}=(L_{flame}+L_{mix})/c$); (c) this p' at the injector plugs the fuel flow rate and results in the phase inversion between p' and φ'; (d) this φ' convects to flame base

($\boldsymbol{\tau}_{conv}$=(L_{flame}+L_{mix})/ $\bar{u}$); (e) heat releases at flame after ignition delay time ($\boldsymbol{\tau}_{ign}$) during the chemical reaction time ($\boldsymbol{\tau}_{chem}$=S_L/α where α is thermal diffusivity) of which calculations are based on the CHEMKIM-Pro computation results. $\boldsymbol{\tau}_{ign}$ is calculated by assuming premixed charges are in a rapid compression machine at appropriate initially-hot temperature which varies according to P_{th}. With these time scales, as previously mentioned, $\boldsymbol{\tau}_{skew}$ is considered to reflect the distortion from multi-mode CI. To analytically calculate $\boldsymbol{\tau}_{skew}$, two harmonic waves having amplitude ratio R=A/B are defined as follows: $Wave_1(\mathrm{t}) = \mathrm{A}\sin(2\pi f_1 \mathrm{t})$ and $Wave_2(\mathrm{t}) = \mathrm{B}\sin(4\pi f_1 \mathrm{t})$. Then, first peak of *wave₁* is located at t_1=1/4f_1, and $\boldsymbol{\tau}_{skew}$ (=t_1-t_2) can be obtained by finding the solution (t_2) which makes first derivative of sum of $Wave_1$ and $Wave_2$ zero.

$$\boldsymbol{\tau}_{skew} = \frac{1}{2\pi f_1}\left\{\frac{\pi}{2} - cos^{-1}\left(\frac{-R+\sqrt{R^2+32}}{8}\right)\right\} \tag{3.5}$$

Here, $\boldsymbol{\tau}_{skew}$ should be considered twice since peak of p' is left-skewed whereas right-skewed φ' generates peak of q' as shown in Fig. 8. Then, total lagging time ($\boldsymbol{\tau}_{tot}$) can be expressed as: $\boldsymbol{\tau}_{tot} = \boldsymbol{\tau}_{acou} + \boldsymbol{\tau}_{conv} + \boldsymbol{\tau}_{ign} + \boldsymbol{\tau}_{chem} + 2\boldsymbol{\tau}_{skew}$.

As shown in Fig. 9, a time-lag plots of 1-D flame model, 2-D flame model and 2-D model with $\boldsymbol{\tau}_{skew}$ are compared to investigate the effect of 1-D/2-D flame model and $\boldsymbol{\tau}_{skew}$. The shaded region (n-0.75 < $\boldsymbol{\tau}_{tot}/\boldsymbol{\tau}_{osc}$ < n-0.25, where n is integer) corresponds to the unstable conditions where p' and q' matches in phase within 90°, thus driving CI (+RI). 1-D thin flame model predicts CI incorrectly because L_{flame} is quite longer than L_{mix} so the approximation of 3-D flame to 1-D resulted in large error in predicting unstable region. This also implies the importance of exact calculation of L_{flame} in a PPM GTMC. Therefore, to describe L_{flame} more precisely, the intensity-weighted centroid [7] was calculated from the 2-D OH^*-PLIF images. This 2-D flame consideration allowed the prediction to be improved but there still remained a slight discordance especially for multi-modes with small amplitude ratio such as the above-mentioned 3rd mode CI. Finally, by including $\boldsymbol{\tau}_{skew}$, remarkable advancement in agreement between model predictions and experimental data is obtain with the strongest instabilities at around $\boldsymbol{\tau}_{tot}/\boldsymbol{\tau}_{osc}$ =1.5. The contribution to the total lagging time was in the order of $\boldsymbol{\tau}_{conv} > \boldsymbol{\tau}_{skew} > \boldsymbol{\tau}_{acou} > \boldsymbol{\tau}_{chem} > \boldsymbol{\tau}_{ign}$ for 3rd mode ($\boldsymbol{\tau}_{acou}$ >

τ_{skew} for 4th mode), and relatively small characteristic time scales such as τ_{chem} and τ_{ign} can be ignored for efficiency and simplicity of time-lag model.

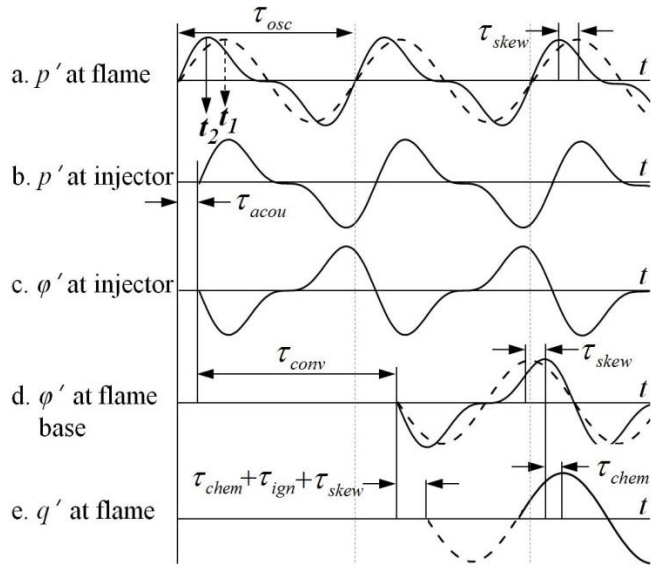

Fig. 3.18 Evolution of multi-mode pressure disturbance in GTMC.

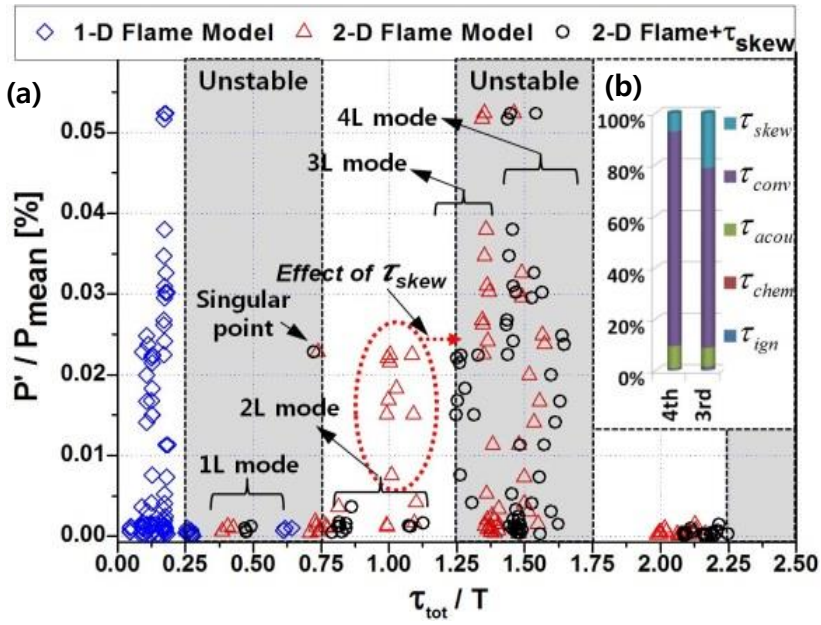

Fig. 3.19 (a) Time-lag plot for 1-D flame model, 2-D flame model and 2-D flame model with τ_{skew} and (b) fraction of time scales in τ_{tot}.

3.3.6 Summary and conclusion of the CI analysis for $H_2/CO/CH_4$ syngas

The fuel composition effects of $H_2/CO/CH_4$ syngas (0~100 mole% for each component gas) on the self-excited high multi-mode CI characteristics have been studied in a PPM GTMC by investigating flame structure, Rayleigh indices, POMs and characteristic time scales from the images of high-speed chemiluminescence and OH^*-PLIF. The flames have different shapes and generate different CI frequency at near 4L or 3L mode with their harmonics. The CI frequency which is non-linear for fuel composition was appeared to be linearly proportional to T_{ad} and S_L. Phase-synchronized OH^*-PLIF images suggested clues of an important CI driving mechanism including the periodic alternation of flame attachment/detachment and coupling of vortex with everlasting heat release at the ORZ due to high reactivity of high hydrogen fuels. These images also used for the precise calculation of 2-D flame length by obtaining centroid of heat release intensity when performing time-lag analysis. The RI results notified the dependence of the location and intensity of CI driving/damping on the fuel composition and instability mode. For higher H_2 containing flame (4th mode), driving and damping is occurred in narrow region but with high heat release density and the frequency of RI was doubled. Otherwise in case of 3rd mode RI shape was similar with pressure fluctuation due to the characteristics of multi-mode CI with high superposition of higher harmonics. Analysis of POD from high-speed OH* images showed the distinct coherent structures and large roll-up of flame are responsible for generating flame oscillations for each mode. High cross-correlation was found between POMs of 4th mode indicating convection of these coherent structures. When conducting TLA for syngas in a PPM GTMC, the significance of effect of wave distortion from superposition of higher harmonic waves and careful inspection on L_{flame} using 2-D OH^*-PLIF is verified by showing the improvement in prediction accuracy. To attenuate the likelihood of this high multi-mode CI in fuel-flexible syngas turbines, of importance is the optimum design of L_{mix}, which avoids unstable region with the consideration of widely varying flame shape as well as flashback and flame attachment/detachment.

CHAPTER 4

EFFECT OF N_2/CO_2/STEAM DILUTION ON THE SYNGAS COMBUSTION

Most IGCC plants utilize water saturation or nitrogen dilution technique to reduce the NO_x emission. Depending on where the diluents inject and with whom they are mixed, this dilution technique can be divided into two methods: fuel-side dilution and air-side dilution. Most of IGCC plant including Taean IGCC uses the latter methods since it is more effective in reduction NO_x [77]. Therefore, to provide useful information of fuel-side dilution technique to control the NO_x emission, the gas turbine combustion characteristics of syngas that is composed of H_2, CO, CH_4, N_2, CO_2, and steam are investigated and the dilution effect of the last three gases are evaluated. First, the effect of N_2 dilution on the characteristics of H_2/CO/CH_4 syngas is described in subchapter 4.1. Next, the effect of N_2, CO_2 and steam dilution on the characteristics of H_2/CO syngas is discussed in subchapter 4.2. Especially, the effectiveness of diluents on NO_x reduction is examined by suggesting analytical correlation between NOx reduction and diluent heat capacity.

4.1 EFFECT OF N_2 DILUTION ON THE COMBUSTION CHARACTERISTICS OF H_2/CO/CH_4 SYNGAS

Combustion performances including temperature, NO_x/CO emission and combustion instability are investigated when varying the amount diluent in H_2/CO/CH_4 syngas. To offer a simpler description, the dilution ratios of N_2, CO_2 and steam are defined in following equations:

$$DR_{N_2} = \frac{\text{flow rate of N}_2\text{ [slpm]}}{\text{sum of flow rate of combustible gases [slpm]}} \tag{4.1}$$

$$DR_{CO_2} = \frac{\text{flow rate of } CO_2 \text{ [slpm]}}{\text{sum of flow rate of combustible gases [slpm]}} \tag{4.2}$$

$$DR_{steam} = \frac{\text{flow rate of steam [slpm]}}{\text{sum of flow rate of combustible gases [slpm]}} \tag{4.3}$$

Here, the nitrogen dilution ratio indicates how many times of nitrogen are contained in the fuel, compared to the combustible H_2/CO gas. Thus, 100%, 60% and 0% of DR_{N2} are equivalent to 50 mol%, 30 mol% and 0 mol% of N_2 respectively, and these fuel compositions can be expressed in molar concentration as shown in Fig. 4.1.

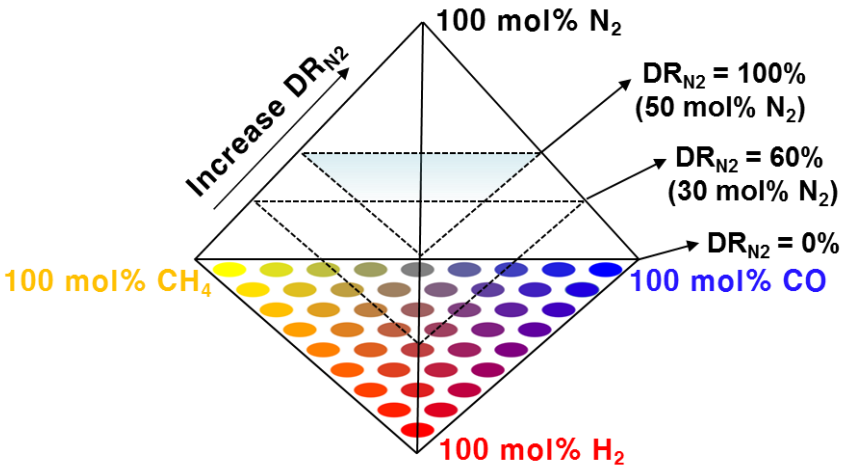

Fig. 4.1 Quaternary diagram of H_2/CO/CH_4/N_2 syngas to describe the dilution ratio of nitrogen.

Figures 4.1 and 4.2 show the T_3 at 40kW$_{th}$ and 50kW$_{th}$. For both heat inputs, the decreasing tendency of T_3 can be clearly seen as increasing the DR_{N2}. This tendency is attributed from the fact that dilution with nonflammable N_2 decreases the flame temperature, which reduces the rate of syngas oxidation reactions and hence combustor liner temperature. This low flame temperature also influences the NO_x and CO emission significantly. As shown in Figs. 4.3 and 4.4, NO_x decreases to the negligible levels as

increasing DR_{N2}. Since previously mentioned Zeldovich mechanism dominates the NO_x emission in fuel lean condition, the decreasing tendency of combustor liner temperature and NO_x emission is almost similar. On the other hand, it is known that CO is inversely proportional to the flame temperature. As illustrated in Figs. 4.5 and 4.6, CO emitted largely in high CO composition and the emission level increased as adding more nitrogen in fuel. Dilution with nonflammable gases decreases the flame temperature, which slows down the oxidation reaction of syngas and this slow reaction can cause incomplete combustion, especially at the low heat input since flame temperature depends on the φ.

The dilution ratio also affected both the intensity and location of combustion instability. The intensity of combustion oscillation attenuated as raising the DR_{N2} since heat release from flame decrease and consequently Rayleigh index, which are correlated with the oscillation between heat release rate and pressure fluctuation. The fuel composition at which instability occurs varied from higher H_2 containing H_2/CH_4 syngas to lower H_2 containing H_2/CH_4 syngas. This attenuated intensity of combustion instability and its diminished area which corresponds to fuel compositions are very positive aspects of the dilution technique. Therefore, it can be concluded that dilution of nitrogen in syngas plays a positive role in view of the combustion instability as well as NO_x emission. However, CO is emitted at significant level for low loads with high dilution so careful monitoring of CO emission is needed when using the fuel-size dilution technique.

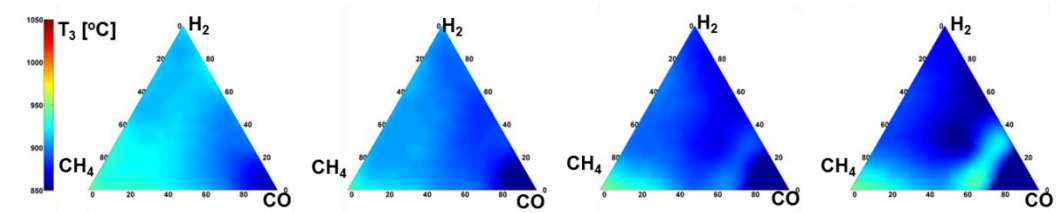

(a) DR_{N2}=0% (b) DR_{N2}=20% (c) DR_{N2}=40% (d) DR_{N2}=60%

Fig. 4.1 Combustor liner temperature at 40kW$_{th}$ with respect to N_2 dilution ratio.

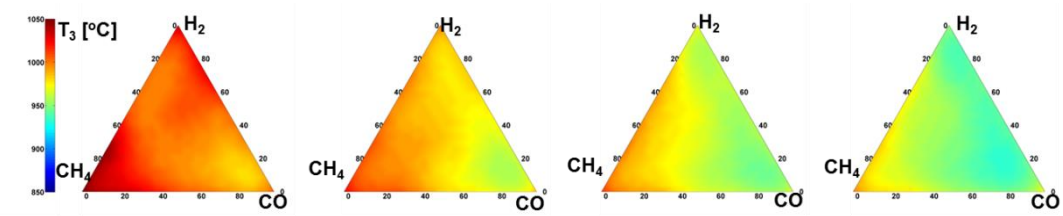

(a) DR_{N2}=0% (b) DR_{N2}=20% (c) DR_{N2}=40% (d) DR_{N2}=60%

Fig. 4.2 Combustor liner temperature at 50kW$_{th}$ with respect to N_2 dilution ratio.

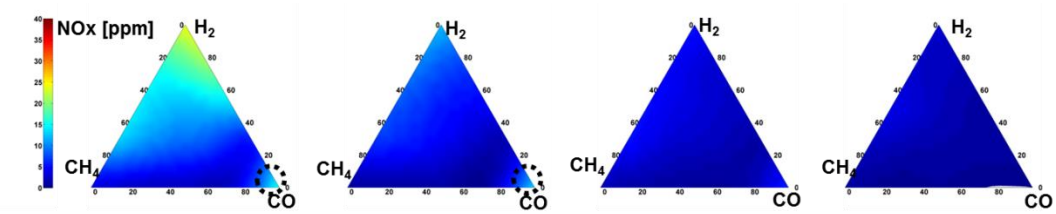

(a) DR_{N2}=0% (b) DR_{N2}=20% (c) DR_{N2}=40% (d) DR_{N2}=60%

Fig. 4.3 NOx emission at 40kW$_{th}$ with respect to N_2 dilution ratio.

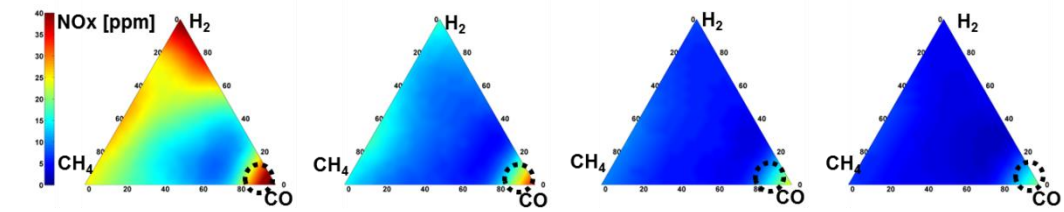

(a) DR_{N2}=0% (b) DR_{N2}=20% (c) DR_{N2}=40% (d) DR_{N2}=60%

Fig. 4.4 NOx emission at 50kW$_{th}$ with respect to N_2 dilution ratio.

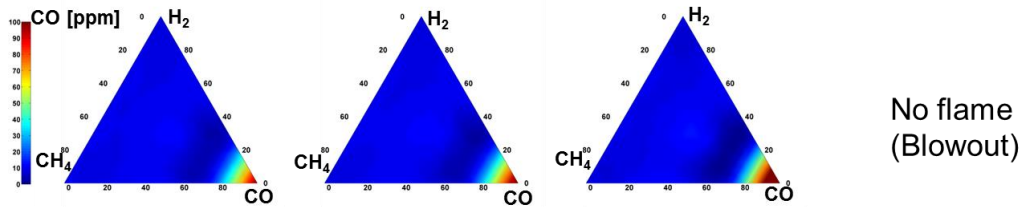

(a) DR_{N2}=0% (b) DR_{N2}=20% (c) DR_{N2}=40% (d) DR_{N2}=60%

Fig. 4.5 CO emission at 40kW_{th} with respect to N_2 dilution ratio.

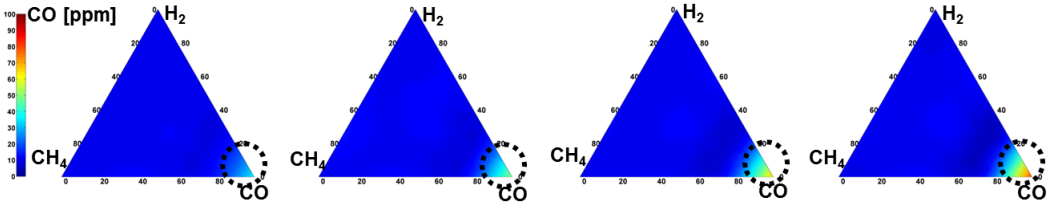

(a) DR_{N2}=0% (b) DR_{N2}=20% (c) DR_{N2}=40% (d) DR_{N2}=60%

Fig. 4.6 CO emission at 50kW_{th} with respect to N_2 dilution ratio.

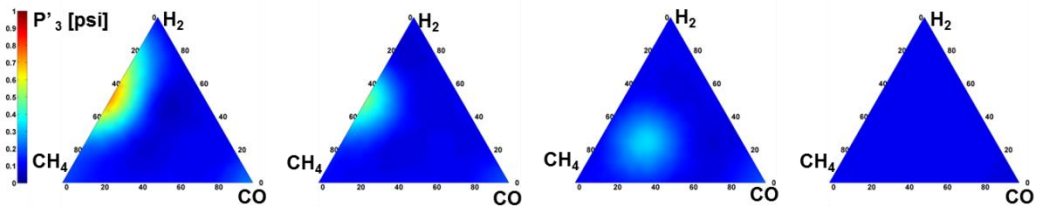

(a) DR_{N2}=0% (b) DR_{N2}=20% (c) DR_{N2}=40% (d) DR_{N2}=60%

Fig. 4.7 RMS of P'_3 at 40kW_{th} with respect to N_2 dilution ratio.

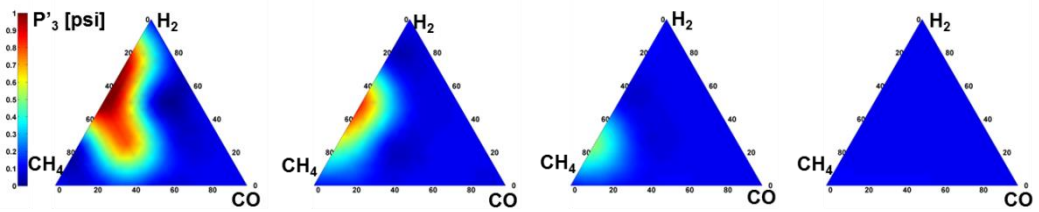

(a) DR_{N2}=0% (b) DR_{N2}=20% (c) DR_{N2}=40% (d) DR_{N2}=60%

Fig. 4.8 RMS of P'_3 at 50kW_{th} with respect to N_2 dilution ratio.

4.2 EFFECT OF N_2/CO_2/STEAM DILUTION ON THE COMBUSTION CHARACTERISTICS H_2/CO SYNGAS

In this chapter, NO_x and CO emissions, combustion instabilities, flame shapes, and the temperature at several points of the combustion chamber are observed while varying the dilution ratio of nitrogen, carbon dioxide and steam in H_2/CO syngas flame. The feeding rate of syngas for this experiment is outlined in Table 4.1. Syngas composition is determined by the ratio of syngas composition of the existing Buggenum IGCC plant in the Netherlands [57] shown in Table 4.2. The dilution rate of nitrogen, carbon dioxide and steam is varied from 0% to 90%, 40% and 100% respectively, of which the span is 10%. These conditions are determined by the amount of dilution gas used at the Buggenum IGCC plant, but the larger dilution range is used to further investigate and understand the dilution of carbon dioxide and steam. The feeding ratio of hydrogen and carbon monoxide is approximately 1:2, which is well matched to the conditions of the Buggenum plant as shown in Table 4.1.

Heat input [kW_{th}]	Syngas flow rate [Nm^3/hr]	H_2 [Nm^3/hr]	CO [Nm^3/hr]	Overall equivalence ratio	Dilution ratio [%]		
					N_2	CO_2	Steam
30	25.62	3.15	6.36	0.343	0~90	0~40	0~100
35	29.89	3.68	7.42	0.400	0~90	0~40	0~100
40	34.17	4.20	8.47	0.457	0~90	0~40	0~100
45	38.44	4.73	9.53	0.514	0~90	0~40	0~100
50	42.71	5.26	10.59	0.572	0~90	0~40	0~100
55	46.98	5.78	11.65	0.628	0~90	0~40	0~100

Table 4.1 Experimental conditions for N_2/CO_2/steam dilution test.

Name of Gas	CO_2	N_2	H_2O	H_2	CO
Syngas Composition [%]	0.80	42.60	19.10	12.30	24.80
C_p @ 573K [kJ/kg·K]	1.06	1.07	2.00	14.54	1.08
C_p @ 573K [J/mol·K]	46.58	29.96	36.00	29.08	30.26

Table 4.2 Syngas gas composition and constant pressure specific heat at 573K [57, 71, 78]

4.2.1 NOx emission characteristics

Figures 4.9–4.11 show the dilution effect of nitrogen, carbon dioxide, and steam on the NO_x emissions of the syngas combustion. As shown in Fig. 3, in the case of N_2 dilution, the NO_x emissions show a tendency to increase as the heat input increases. This result matches with Zeldovich's NO_x mechanism where the flame temperature increases as more fuel is added to the combustor in fuel-lean conditions. Meanwhile, the NO_x emission decreases exponentially as the DR_{N2} increases, which is why in the IGCC plant surplus nitrogen from the air separation unit is injected into the gas turbine combustor. The incoming dilution gas to the combustor results in the same heat input having to heat a larger amount of gases. The lowering of the flame temperature means less NO_x is emitted, according to Zeldovich's NO_x mechanism.

In the case of NO_x emission characteristics of the CO_2 and steam dilution, both decrease as the dilution ratio is raised and both increase as the heat input is raised. The amount of NO_x reduction at the same DR is largest when steam is injected, followed by the CO_2 and N_2. When the DR of N_2, CO_2, and steam is 40% at 55 kW heat input, the NO_x emission is reduced by 78.6%, 87.7%, and 95.0% respectively. To clearly see the cause and effect of dilution on the NO_x reduction, the following definitions are shown by equations 4.3 to 4.5.

$$\text{Diluent heat capacity [J/ K-s]} = \dot{m}_{diluent} \cdot C_{p,\, diluent} \tag{4.4}$$

$$NO_x \text{ reduction [ppm]} = (NO_x \text{ without dilution}) - (NO_x \text{ with dilution}) \tag{4.5}$$

$$NO_x \text{ reduction per unit heat input [ppm/kW]} = \frac{NO_x \text{ reduction [ppm]}}{\text{Heat input [kW]}} \tag{4.6}$$

Herein NO_x reduction per unit heat input denotes how much NO_x is emitted to generate unit electricity since heat input is linearly proportional to power output when assuming that plant efficiency is constant.

Figure 10 shows the relationship between NO_x reduction and diluent heat capacity. With constant heat input, the NO_x reduction increases logarithmically as the diluents heat capacity increase, approaching the value of NO_x emission without dilution. When it comes to lean, partially premixed syngas combustion, the amount of NO_x reduction is related to the diluent heat capacity itself, rather than the kind of gas, because the dilution gas is seldom involved in the chemical reaction. Only the heat capacity can be counted. Figure 5 demonstrates that the amount of NO_x reduction per unit of heat input is only the function of the diluent heat capacity. It can be concluded that the most important property of NO_x reduction is specific heat at a constant pressure. The amount of NO_x reduction can be determined by the multiplier of the mass flow rate and heat capacity i.e. the diluent heat capacity, and the heat input that is proportional to the amount of fuel input.

This relationship between NOx reduction and diluent heat capacity is verified by the following derivations of analytic equations. First, Zeldovich mechanism is as follows:

$$O + N_2 \xrightarrow{k_{1f}} NO + N, \quad k_{1f} = 1.8\times10^{11} \exp\left(\frac{-38,370}{T\ [K]}\right) \quad m^3/kmol\cdot s \tag{4.7}$$

$$N + O_2 \xrightarrow{k_{2f}} NO + O, \quad k_{2f} = 1.8\times10^{7} T \exp\left(\frac{-4680}{T\ [K]}\right) \quad m^3/kmol\cdot s \tag{4.8}$$

$$N + OH \xrightarrow{k_{3f}} NO + H, \quad k_{3f} = 7.1\times10^{10} \exp\left(\frac{-450}{T\ [K]}\right) \quad m^3/kmol\cdot s \tag{4.9}$$

Since Eq. (4.7) dominates the thermal NO_x mechanism and backward reaction is negligible comparing to the forward reaction, Eqs. (4.7)~(4.9) can be induced to Eq. (4.10).

$$\frac{d[NO]}{dt} = 2k_{N1,f}[O]_{eq}[N_2]_{eq} \tag{4.10}$$

Since NOx emission is more affected by T_{ad} rather than [O] or [N_2] in the

environment of enough oxygen and nitrogen (i.e. fuel lean condition), following relationship can be obtained:

$$NOx\ reduction = [NO]_1 - [NO]_2 \sim A\left\{\exp(\frac{-38370}{T_1}) - \exp(\frac{-38370}{T_2})\right\} \tag{4.11}$$

where $[NO]_1$ and $[NO]_2$ denote the amount of NO emission in first and second cases.

Then, from the calculation results of adiabatic temperature which will be discussed in subchapter 4.2.4, it can be seen that the dilution ratios are inversely proportional to the flame temperature whereas the heat input is linearly proportional to the T_{ad}.

$$(DR_{N2}, DR_{CO2}, DR_{steam}) \sim \frac{1}{T_2}\ ,\ \dot{m}c_p \sim \frac{1}{T_2}\ ,\ kW \sim T_{ad} \tag{4.12}$$

Thus, Eq. (4.13) can be induced by substituting Eq. (4.12) into Eq. (4.11).

$$NOx\ reduction \sim \exp(\frac{-318 \times \dot{m}c_p}{R}) \sim \exp(\frac{-318}{R \times kW}) \tag{4.13}$$

After dividing both sides by heat input, nonlinear exponential fitting can be expressed as follow:

$$NOx\ reduction / kW = 0.99 - 0.81\exp(-0.88 \times \dot{m}c_p) \tag{4.14}$$

This curve is plotted together in Fig. 4.11 showing excellent fitness with adjusted cross- correlation coefficient of 0.95.

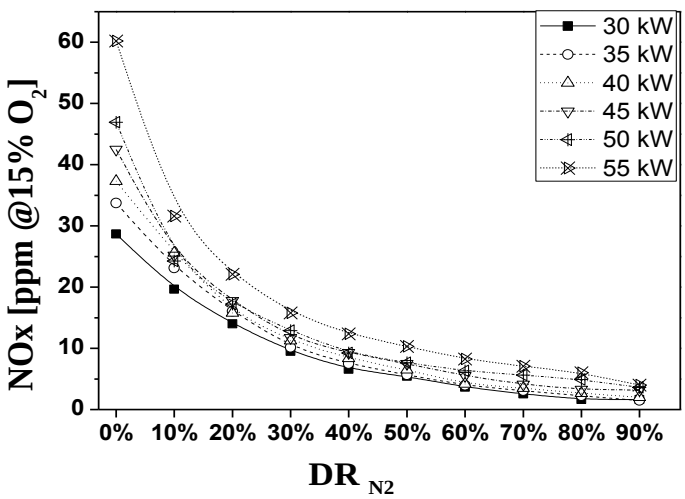

Fig. 4.9 NO_x emissions with respect to the N_2 dilution ratio.

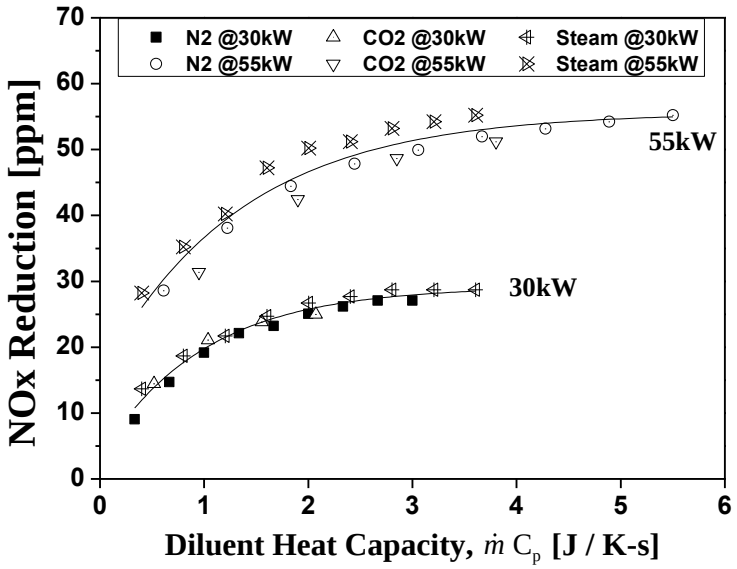

Fig. 4.10 NO_x reduction with respect to the diluent heat capacity of N_2, CO_2, and steam.

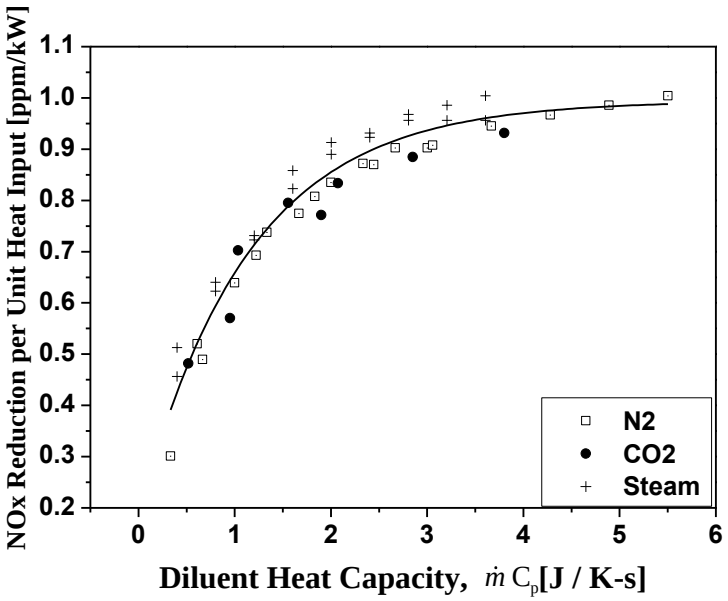

Fig. 4.11 NO_x reduction per unit heat input with respect to the diluent heat capacity of N_2, CO_2, and steam.

4.2.2 CO emission characteristics

Figure 4.12 shows the variation of CO emissions with respect to the diluents, heat input, and DR. In all test cases without steam at 30kW, the CO emission is under 10ppmv, corrected by 15% oxygen in exhaust gas i.e. over 99.9% combustion efficiency. Such a good combustibility can be differed from the case of pure methane or carbon monoxide flame itself, because the higher hydrogen content (over 20%) results in almost perfect combustion, according to the previous research [20]. Where steam dilution is at 30kW, the CO emission increases exponentially according to the DR. This phenomenon means that dilution can cause the incomplete combustion of syngas, which is distinctive in the case of steam dilution. Dilution with nonflammable gases decreases the flame temperature, which slows down the oxidation reaction of CO and H_2. Slow reaction can cause incomplete combustion, especially at the low heat input since flame temperature depends on the equivalence ratio (further discussion on the flame temperature can be found in subchapter 3.4). Moreover, since steam has the largest heat capacity (based on mass) of the three dilution gases shown in Table 3, flame temperature and reaction rate is affected more by steam than N_2 and CO_2 and thus steam dilution emits more CO. It is also notable that the CO emission at 30kW with N_2 dilution of 90% DR is comparable with the steam dilution of 40~50% DR because steam has almost twice the heat capacity of N_2. This also proves that the reduced reaction rate caused by dilution is one of the main reasons why steam injection at low heat input significantly raises CO emissions. Therefore, the use of N_2 or CO_2 dilution is recommended rather than steam dilution in the view of CO emissions. However, in higher load conditions over 40kW, the CO emission remains under 10ppm throughout the DR range from 0% to 100%. It can be concluded that steam dilution in the low load condition should be adapted carefully for a high level of combustion efficiency and environmentally friendly emissions.

4.2.3 Combustion oscillation characteristics

Combustion oscillations of syngas with respect to the DR of N_2, CO_2, and steam dilution are investigated, as shown in Fig. 4.13. The combustion pulsation level is very

low in all tests i.e. almost zero combustion instability is generated. These combustion oscillation results are comparable to the results of previous tests on H_2 and CO combustion without dilution [20], so this characteristic does not change even though the diluents are added in the fuel side. Generally, combustion instabilities are characterized by large-amplitude pressure oscillations that are driven by unsteady heat release. In order to understand why combustion instability is not generated in syngas combustion, it is necessary to consider the specific mechanism responsible for the instability. Two mechanisms are reported to be the particularly significant in gas turbine combustion systems: oscillation feedback [24, 25] and vortex/flame interaction [22, 23]. In the former mechanism, a pressure fluctuation in the combustor results in a velocity and pressure fluctuation at the fuel nozzle, and this perturbs fuel flow rate. This perturbation is propagated to the flame, where it produces a heat release oscillation and, in turn, a pressure fluctuation. Herein, heat release oscillation is the periodic repetition of extinction and re-ignition. Syngas that contains considerable amounts of hydrogen is not easily extinguished, since hydrogen has a larger flammable limit and cannot be blown out even in large flame stretches [48]. Thus, fluctuations in heat release are minimal and do not cause fluctuations in pressure or fuel flow rate. In the latter mechanism, large-scale, coherent vortical structures cause the rate of heat release to oscillate. These structures are the result of flow separation from flame holders and rapid expansions, as well as vortex breakdown in swirling flows. However, in this study, neither vortical structure at the dump plane nor flow separation near the fuel nozzle is observed (as shown in Fig. 4.14) since hydrogen whose burning velocity is very high causes the flame shape to be diffusive-like and short.

Even with these understandings of combustion instability mechanism of syngas, however, predicting of combustion instability is difficult due to need for predicting complex flame response to perturbations, which determines the energy addition rate to the acoustic field by the flame. In addition, since combustion instability is highly depends on the fuel composition of syngas and combustor configurations, careful monitoring on the combustion instability is necessary when operating syngas turbine.

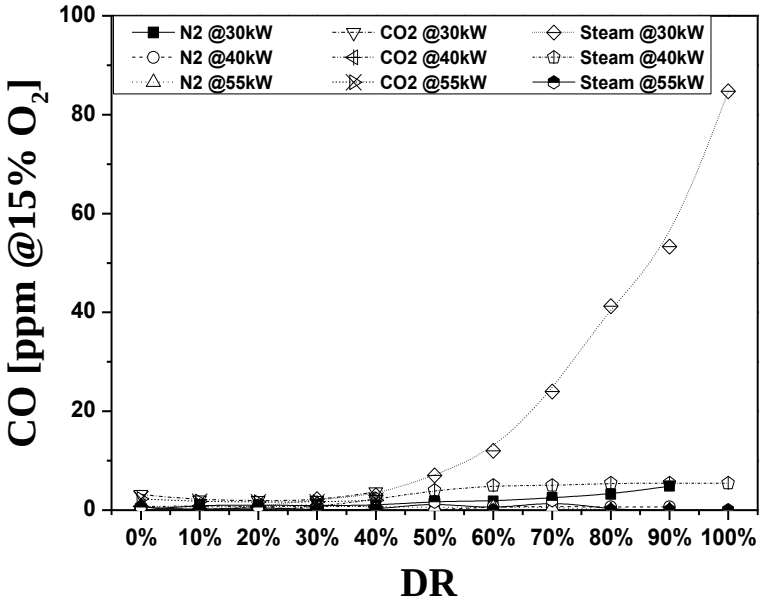

Fig. 4.12 CO emissions with respect to the DR of N_2, CO_2, and steam.

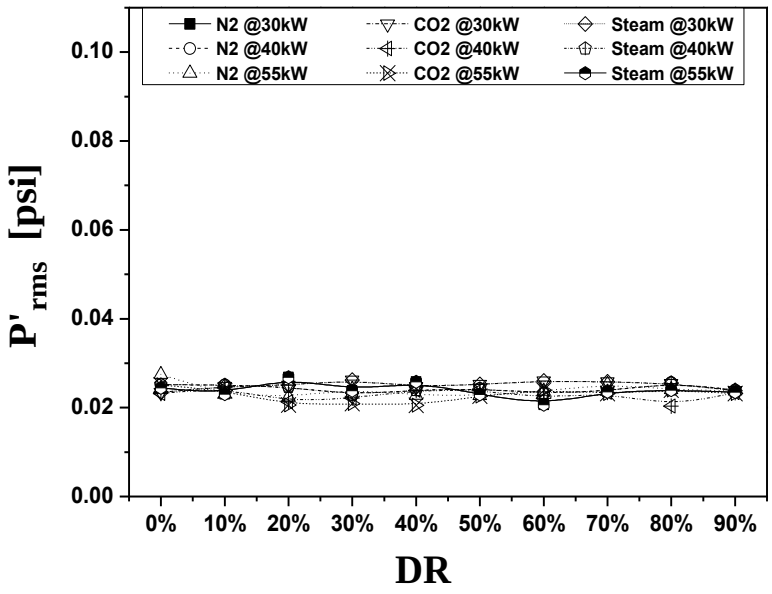

Fig. 4.13 Pressure fluctuation with respect to the DR of N_2, CO_2, and steam.

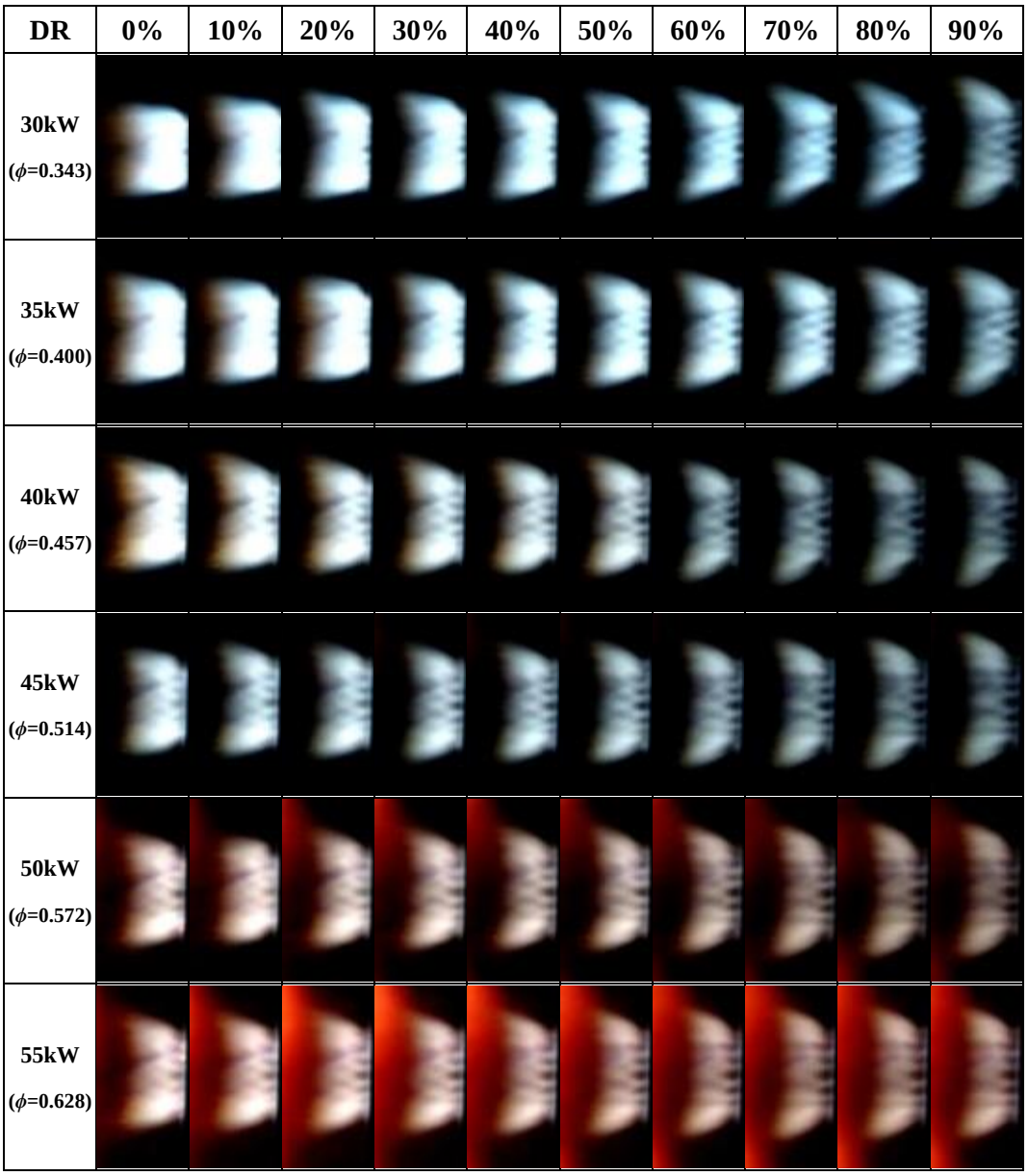

Fig. 4.14 Direct flame photos of H_2/CO syngas with respect to the N_2 dilution ratio

4.2.4 Temperature characteristics

The temperatures at the fuel nozzle (T_n), dump plane (T_d), and exit (T_{ex}) of the combustion chamber are measured regarding DR of N_2, CO_2, and steam. With these

temperatures, the T_{ad} calculated by CANTERA code is plotted together in Fig. 4.15 in order to understand how flame temperature affects T_n, T_d and T_{ex}. Since the combustor liner is cooled by a high-pressure injection of the same amount of air as combustion air, large heat dissipation results in a significant difference between T_{ad} and T_{ex}. As easily expected, T_d, T_{ex} and T_{ad} shows an upward tendency as heat input increases since flame temperature increases following the rise in heat input. However, T_n shows no significant change according to the change in heat input. This result differs from that of previous research on H_2 and CO combustion without dilution [7], which reports an increasing tendency of T_n with the addition of heat input. In this study, since syngas contains large amount of dilution gas (more than 50% as described in Table 3), T_n does not increase as the heat input increases mainly due to the enhanced cooling effect on the fuel nozzle. Another notable characteristic is that T_n decreases as the DR increases, which happens for the following two reasons. Firstly, as shown in Fig. 4.14, flame is lifted up slightly and is not observed near the fuel nozzle as DR increases, which clearly means the fuel nozzle is less heated by the flame. The flame lift-up occurs when the flow velocity at the fuel nozzle exceeds the turbulent flame speed of syngas along the streamline. Dilution with nonflammable N_2 decreases the flame temperature, which reduces the rate of CO and H_2 oxidation reactions and hence flame speed. The fuel jetting velocity increases with the addition of large amounts of diluents. Thus, flame lift-up occurs. Secondly, the convective heat transfer from nozzle to syngas results in the decrement of T_n with respect to the increment of DR. Namely, the higher flow rate of syngas cools down the nozzle better when the radiation from the flame to the fuel nozzle is almost constant at the same heat input. The important implication of this result is that these flame lift-up and nozzle cooling with dilution gases can be used to inhibit flash-back and/or auto-ignition, which are considered to be significant operability issues in syngas turbines [26]. Furthermore, it is also notable that there is a crossing point at around 40% DR in each heat input line. This means that convective cooling by synthetic gas flow is more dominant than radiant heating from the flame to the fuel nozzle when DR is under 40%.

As described in an earlier paragraph, T_d shows an upward tendency as the heat input

increases, and this tendency can be considered with the flame images in Fig. 4.14. By raising the equivalence ratio, the resulting rise in the temperature of the flame and burned gas makes the quartz tube for flame visualization hotter and redder, which in turn heats the dump plane. Furthermore, T_d increases within 50°C as DR_{N2} increases from 0% to 40% and remains constantly above 50% DR. This phenomenon can also be analyzed from the flame images. As shown in Fig. 4.14, the luminosity of the white-blue flame weakens as the DR increases, since the flame temperature, which can be predicted from the T_{ad}, decreases. While this weakened flame lowers T_d, the flame grown wider and closer to the dump plane raises T_d. Trade-off between these two effects is attributed to the slight increasing and constant tendency of T_d.

T_{ex} increases proportionally with the increase of heat input for the same reason as T_d. As DR increases, T_{ex} decreases by 25°C because the larger amount of DR requires a larger mass of exhaust gas to be heated and, for the same reason, T_{ad} also decreases. These kinds of T_{ex} characteristics can be considered significant when designing and operating an IGCC plant because most gas turbines are operated by the turbine inlet temperature (TIT) control.

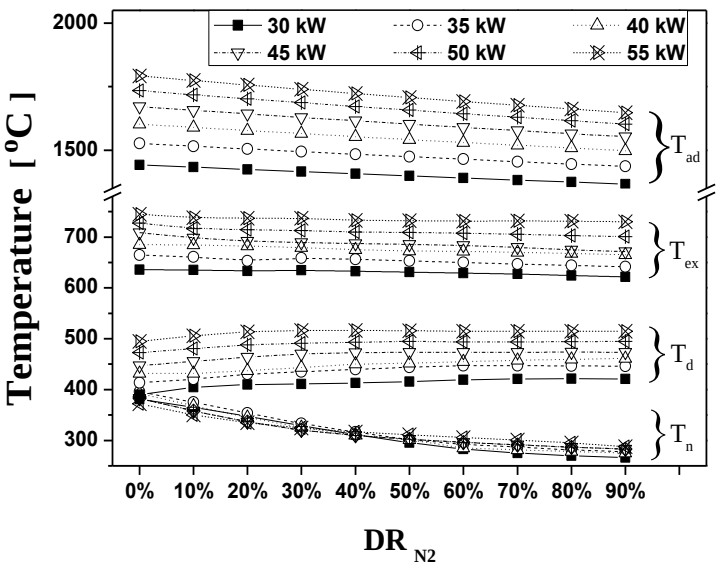

Fig. 4.15 Characteristics of fuel nozzle temperature, dump plane temperature, exit gas temperature and adiabatic flame temperature with respect to the N_2 dilution ratio.

4.2.5 Summary and conclusion of N_2/CO_2/steam dilution study

From the test results of H_2/CO syngas regarding the DR of N_2, CO_2, and steam, the following conclusions are obtained.

(1) The dilution of syngas with nonflammable gas decreases NOx emissions, and the amount of NOx reduction per unit power is logarithmically related to only the diluent's heat capacity which is the product of mass flow rate of the diluent and constant pressure heat capacity. This relationship is also induced as Eq. (4.14) using the Zeldovich mechanism and the calculation results of adiabatic flame temperature with some appropriate assumptions.

$$NOx\ reduction / kW = 0.99 - 0.81\exp(-0.88 \times \dot{m}c_p) \tag{4.14}$$

This result can be used for controlling, adjusting, and predicting the NOx emission of an IGCC plant that uses fuel dilution technology for NOx reduction.

(2) In most of the tested cases, CO below 10ppm is emitted, i.e. almost complete combustion, but in the case of steam dilution at 30kW, CO emissions are increased exponentially according to the dilution ratio. This result means that the dilution system of an IGCC plant should be cautiously operated by monitoring the CO emission for the better fuel efficiency.

(3) The temperature at the nozzle, dump plane, and exit of the combustor shows similar characteristics for all tested diluents. The reason for this is explained by direct photos of the flames and the analysis of their physical meaning on syngas combustion and thermodynamics.

(4) Synthetic gas does not generate combustion instability in all test cases. The reason for this result is explained by introducing two combustion instability mechanisms: oscillation feedback and vortex/flame interaction.

(5) From the results, we conclude that N_2, CO_2 and/or steam are applicable to a syngas turbine to control NOx emissions with ensuring reliable operation. Test data will be used to determine the significant material for combustor design, optimum plant operation, and analysis of plant outage.

CHAPTER 5
APPLICATION ON THE COMMERCIAL GASES: COAL GAS AND SYNTHETIC NATURAL GAS

This chapter presents the results of application test for coal-derived syngas and synthetic national gas into the gas turbine model combustor of this study. Based on the results obtained in chapter 3 and 4, test conditions are determined and test results are interpreted. As previously mentioned in chapter 1, studies of this chapter are aim to provide useful information when operating Taean coal IGCC plant and Kwangyang SNG plant. Thus, simulated gas of which composition is identical to each demonstration plant was used for this study. First, combustion characteristics of the Taean IGCC syngas are compared to that of Buggenum IGCC syngas in view of flame stability, dynamic pressure characteristics, NO_x and CO emissions, temperature in the combustion chamber, and flame structures. Next, the combustion performance of SNG as varying small amount of H_2 is investigated to give important information for the establishment of quality standards for synthetic natural gas in Korea.

5.1 COAL-DERIVED SYNGAS COMBUSTION

The first Korean IGCC project (power output: 300 MW_e; plant site: Taean) was launched in 2006 and is expected to be complete toward the end of 2015. For better operational availability and combustion optimization at this plant, Taean syngas is tested in a model GE7EA gas turbine combustor in this study to quantify the potential application problems and to evaluate its combustion performance as a gas turbine fuel.

Combustion tests on both Taean and Buggenum syngases are conducted with respect to the heat input and DR_{N2}, and the results were compared to understand the effect of slight differences in syngas composition on combustion performance. Table 5.1 outlines the fuel composition of Taean and Buggenum, which were determined from the reports of the Taean and the Buggenum IGCC plants [4]. The main features of the Taean syngas,

compared with the Buggenum syngas, are a lower H_2/CO ratio, lower diluents in fuel due to low moisture, and thus higher heat content per unit volume.

Fuel was supplied from each bottle of feedstock gases while maintaining fuel composition constant and varying heating values from 30 kW to 60 kW, of which span is 5 kW. Fuel gases were mixed well through the inline static mixer and were supplied to the combustor. Instead of carbon dioxide and steam, only nitrogen was used as a diluent because the effect of dilution on combustion performance is almost the same when diluents have the same heat capacity as previously explained in subchapter 4.2. Thus, the equivalent mass flow rate of nitrogen is determined from the following equation:

$$\dot{m}_{N_2,eq} = \dot{m}_{N_2} + \frac{\dot{m}_{CO_2} c_{p,CO_2} + \dot{m}_{steam} c_{p,steam} + \dot{m}_{Ar} c_{p,Ar}}{c_{p,N_2}} \tag{5.1}$$

where $\dot{m}_i$ and $c_{p,i}$ are mass flow rate and specific heat at constant pressure of i-gas.

To offer a simpler description, the IR_{N2} were defined in following equations:

$$IR_{N_2} = \frac{\text{flow rate of } N_2 \text{ [slpm]}}{N_2 \text{ equivalent dilution ratio} \times \text{total fuel flow rate [slpm]}} \tag{5.2}$$

While the nitrogen dilution ratio which is expressed in Eq. (4.1) indicates how many times of nitrogen are contained in the fuel, compared to the combustible H_2/CO gas, the IR_{N2} indicates how many times of nitrogen content is in the fuel, compared to the composition of the Taean or Buggenum syngases. That is to say, 100% of IR_{N2} is 56.4 mol% and 65.4 mol% nitrogen in the fuel at Taean and Buggenum, respectively. This represents the conditions under which all nitrogen produced from an air separation unit is supplied to the gas turbine combustor and, thus, when an IGCC plant is operating with the maximum integration of nitrogen.

Syngas composition	Unit	Taean [A]	Buggenum [B]	Difference [(A-B)/A]
H_2	mol%	12.9	12.3	3.54%
CO	mol%	31.5	24.8	21.12%
CH_4	mol%	0.1	0.0	0%
N_2	mol%	50.8	42.4	17.09%
CO_2	mol%	0.4	0.8	-114.57%
H_2O	mol%	4.2	19.1	-341.86%
Ar	mol%	0.4	0.6	-37.09%
H_2S	mol%	0.0	0.0	0%
Sum	mol%	100.0	100.0	0%
Higher heating value	MJ/Nm^3	5.60	4.70	16.07%
Lower heating value	MJ/Nm^3	5.35	4.46	16.64%
H_2/CO	%	40.6	49.6	-22.47%
Mole fraction of combustible gas	mol%	44.3	37.1	16.06%
LFL in air	%	19.1	21.2	-10.99%
UFL in air	%	73.3	71.7	2.18%
N_2 equivalent dilution ratio	%	56.4	65.4	-15.96%
Upper Wobbe index	MJ/Nm^3	10.02	9.44	5.79%
Lower Wobbe index	MJ/Nm^3	9.57	8.95	6.48%

Table 5.1 Syngas composition of Taean and Buggenum [4].

5.1.1 Flame stability map

In the present study, the stability regime according to the flame shape and intensity of pressure fluctuation is classified, as reported in many flame stability map researches [48, 80, 81]. Fig. 5.1 describes the criteria for classification on the flame stability map. Regime I is a V-shaped flame; this flame shape occurs due to swirling flow and outwardly diverging recirculation flow toward the dump plane while the flame root is attached to the fuel nozzle. Regime II is an M-shaped flame; as opposed to regime I, this type of flame interacts with a vortex flow and burns close to the dump plane and quartz liner. In regime IV, a long cone-shaped flame occurs, and it seems like a long tornado due to the swirling flow. In regime III, flames of regime II and IV occur alternately, and this flame oscillation results in large pressure fluctuations. In regimes V and VI, lift off and blowout phenomena occur, respectively.

Fig. 5.2a shows the flame stability map of Taean and Buggenum syngas according to DR_{N2}. For both fuels, flame changes from strong burning regime I though II, III, IV and V to regime VI as the DR_{N2} increased and the heat input decreased. Regime I occurred at just over 40 kW of heat input with a DR_{N2} under 100%. As the nitrogen dilution increased, more enhanced recirculation flow occurred due to high fuel–air mixture momentum, which resulted in the flame's transition from regime I to regime II. Further nitrogen additions in syngas slowed down the combustion reaction, and consequently lowered the burning velocity. Moreover, since a nitrogen addition increases the mean mixture velocity, the flame was extinguished locally, being detached from dump plane and moving downstream when the mean mixture velocity exceeded the turbulent burning velocity. This movement downstream resulted in a regime shift from II to VI, passing through a narrow region of III, in which the flame oscillated very unstably with an alteration motion between detachment and attachment to the dump plane. Next, flame lifting (regime V) and lean blowout (VI) phenomena occurred sequentially with decreasing heat input and increasing nitrogen dilution. Combustion instability did not occur for all tested conditions without regime III (detailed results and discussions on the combustion instability

characteristics are in subchapter 3.5). Therefore, when considering only the flame stability map, we conclude that only regimes I and II are stable operating conditions for Taean and Buggenum syngas combustion, and the Taean syngas is more stable when compared to the Buggenum syngas since it occurred farther from the unstable regime III.

In the meantime, we redrew the flame stability map according to the nitrogen mole fraction in fuel, as demonstrated in Fig. 5.2b. This figure illustrates several important points missing from Fig. 5.2a. First, in the low load condition, excessive nitrogen dilution (exceeding 30 mol%) can cause unstable combustion. Second, all borderlines (except the border between regimes I and II) asymptotically approach the range between 77 mol% and 82 mol%. Third, the flames of both fuels cannot exist when the nitrogen content is more than 82 mol% in the fuel. To understand why a flame blows out over a certain limit, we estimated the LFL of the $H_2/CO/N_2$ mixture on the basis of the Le Chatelier rule [28, 29]:

$$FL_{mix} = \frac{100}{\frac{x_1}{FL_1} + \frac{x_2}{FL_2} + \frac{x_3}{FL_3} + \cdots} \tag{5.3}$$

where FL_{mix} is measured the flammability limit of the mixture in vol%, FL_i is the flammability limits of the binary sub-mixtures comprised of one combustible gas and one inflammable gas, and x_i the volume percentage of a sub-mixture in total fuel ($\Sigma x_i = 1$). Assuming that the sub-mixtures are H_2+N_2 and CO+N_2, we calculated the maximum LFL of Taean and Buggenum syngases as 83.9 vol% and 84.5 vol%, respectively. These value lines are plotted in Fig. 5.2b, and the blowout limit occurred because both fuels approach the LFL lines of syngas but cannot exceed them. It is notable that even though a high swirl stabilizes a flame nearly until the LFL, the flame cannot go beyond the maximum LFL of syngas. Inversely, the blowout limit line of any mixture can be estimated by obtaining the maximum LFL of a mixture.

Regime	Flame images	Description
I		V-shaped flame (Flame does not interact with outer recirculation flow)
II	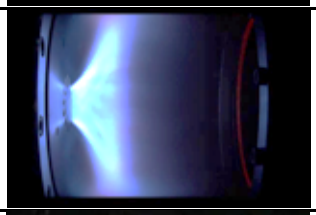	M-shaped flame (Flame interacts with outer recirculation flow)
III		Oscillating flame (Flame oscillates alternately between M-shaped flame and long cone-shaped flame)
VI		Long cone-shaped flame (Flame does not interact with outer recirculation flow and seems like a tornado due to swirling flow)
V		Lift-off
VI	No Flame	Blowout

Fig. 5.1 Criteria for classification on a flame stability map.

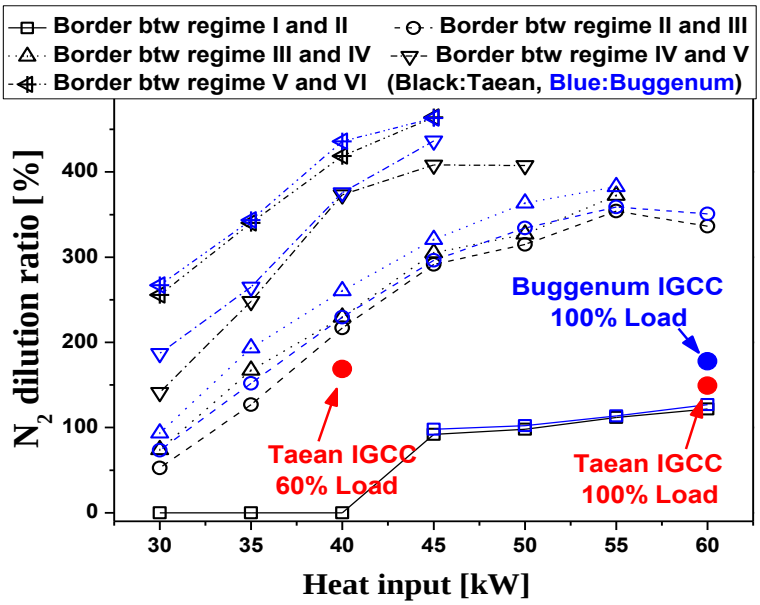

(a) Flame stability map of Taean and Buggenum syngases according to the DR_{N2}.

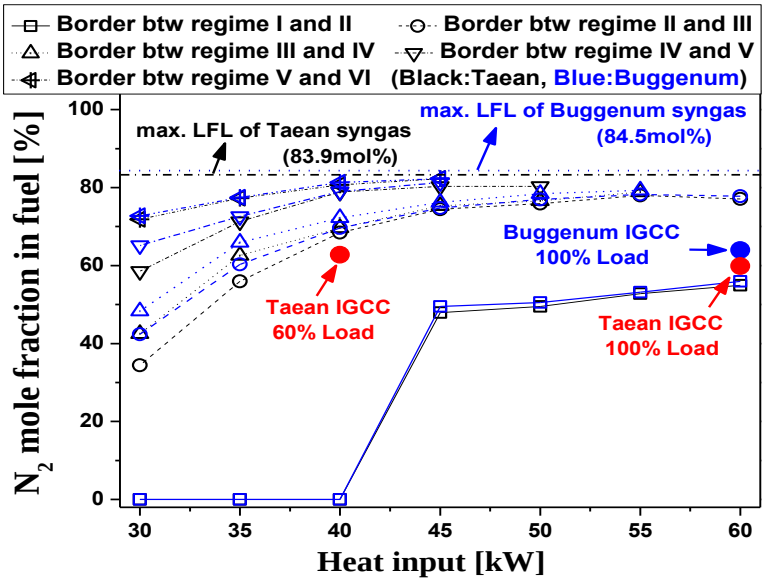

(b) Flame stability map of Taean and Buggenum syngases according to the nitrogen mole fraction in fuel.

Fig. 5.2 Flame stability map of Taean and Buggenum syngases.

5.1.2 Temperature characteristics

Fig. 5.3 presents measurements of T_1 and T_4 with respect to IR_{N2}. With these temperatures, the T_{ad}, calculated via CATERA code with the GRI 3.0 mechanism, is plotted. For all test conditions, the T_1 maintained at 200±3°C, which indicates that the air preheater controls T_1 well and that the test's accuracy in terms of temperature is over 98.5%. As easily expected, T_4 and T_{ad} show a linearly increasing tendency as heat input increases because the flame temperature increases following the rise in heat input. As the IR_{N2} increases, the T_{ad} decreased almost linearly since the addition of inflammable nitrogen increased the total heat capacity in the fuel and, thus, the heat demand to raise the flame temperature. The nitrogen-induced flame cooling effect at Buggenum is stronger than that at Taean, since the Buggenum syngas has a higher nitrogen mole fraction in the fuel, as shown in Table 5.1. This fact implies that the Buggenum IGCC plant expends 16% more nitrogen to control the NO_x emission, resulting in a decrease in flame temperature by 8.2%.

Similar characteristics in T_4 were observed for the same reasons. However, we observed a sudden drop in T_4 at over 50% of IR_{N2}. Flame position and structure largely affected T_4, so the stability mode change from regime II to regime IV via regime III resulted in the change in T_4. For example, for the Taean syngas at 30 kW, we observed a sudden drop between 39% and 50% of IR_{N2}, and this condition corresponds to the 47.3% and 86.4% of DR_{N2}, which are respectively in regimes II and IV according to Fig. 5.2a. On the other hand, for the Buggenum syngas at 30 kW, we observed a sudden temperature drop between 50% and 100% of IR_{N2}, and this condition corresponds to the 88.2% and 176.3% of DR_{N2}, which are in regimes III and IV, respectively. Thus, it can be concluded that flame movement downstream is the main cause of a sudden drop in combustor liner temperature. From this result, nitrogen for NO_x reduction should be carefully controlled in a lower load (under 40 kW) since flames are easily destabilized. Consequently, the flame might lift off and then damage downstream parts of the combustor, such as turbine blades and vanes.

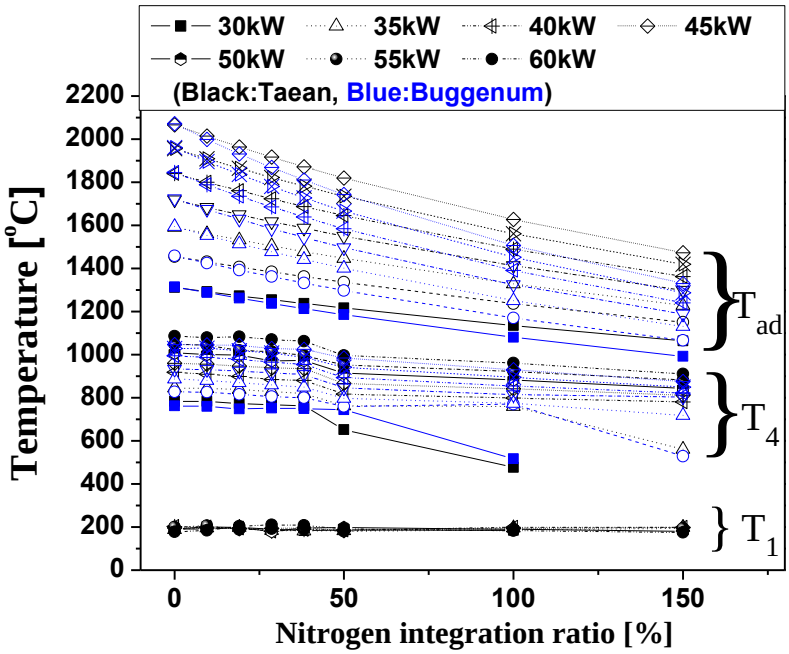

Fig. 5.3 Temperature characteristics of Taean and Buggenum syngases according to the IR_{N2}.

5.1.3 NO_x and CO emission characteristics

Figs. 5.4a and 5.4b show the emission characteristics of NO_x and CO with respect to IR_{N2}. For both syngases, the concentration of NO_x emissions showed an exponentially decreasing trend when adding more nitrogen to the fuel for all heat inputs. We attributed these results to the decrease in flame temperature via increased nitrogen integration and the extended Zeldovich NO_x mechanism, which explains that NO_x emissions are exponentially correlated with flame temperature. From the three Zeldovich reactions (Eqs. 4.6~4.8), NO can be minimized by decreasing $[N_2]$, [O], or k_1 (i.e., by decreasing the flame temperature). It is noteworthy that increased N_2 enhances NO_x emissions in view of $[N_2]$, and simultaneously suppresses NO_x in view of flame temperature. However, flame temperature dominates the NO_x emission, and thus NO_x decreases as N_2 increases because k_1 is insignificant at temperatures < 1700 K [65]. This feature is evident in Fig.

5.5, which illustrates the NO_x emission dependence on flame temperature. For both syngases, NO_x emissions become significant at T_{ad} > 1450°C and increase exponentially as T_{ad} increases. Furthermore, most of the test data fit well in the exponential asymptotic curve. This good fit implies that T_{ad} mainly affects NO_x, not the nitrogen mole fraction. Discordance and early rise of NO_x in low heat input conditions might be attributed to the nature of partially premixed flame, which forms a localized high temperature zone. NO_x emissions of the Taean syngas were slightly higher than that of Buggenum by 2.09 ppm at 60 kW without N_2 dilution. Since flame temperature is almost the same for that condition, residence time in flame can be considered as the main cause of the NO_x emission difference. We calculated the residence time via the following equation, which is based on hot gas flow through the primary flame zone [73, 74]:

$$\tau_{res} = \frac{V_{pz}\ P_3}{\dot{m}_{air}\ R_{air}\ T_{in}} \tag{5.4}$$

where V_{pz}, P_3, $\dot{m}_{air}$, R_{air} and T_3 are volume of the primary zone [m^3], combustion chamber inlet pressure [Pa], mass flow rate of air [kg/s], ideal gas constant for air [J/kg-K] and combustion chamber inlet temperature [K] respectively. Herein, P_3, $\dot{m}_{air}$, R_{air} and T_{in} are the same for both syngases and only V_{pz} is a control variable of $\boldsymbol{\tau}_{res}$, which is obtained from the time-averaged Abel-deconvoluted OH^*-chemiluminescence images in Fig. 5.6. The calculated V_{pz} of the Taean syngas was 5020 mm^3, which was larger than that of Buggenum by 8.2%, and consequently, the $\boldsymbol{\tau}_{res}$ of the Taean syngas was longer than that of Buggenum by 4%. Therefore, we can assert that an 8.2% longer $\boldsymbol{\tau}_{res}$ in a flame is a vital cause of increased NO_x emissions when comparing the Taean and Buggenum syngases. This volume difference might be due to the H_2/CO ratio in the fuel. Since H_2 burns more than 10 times faster than CO (see Table 3.1), the Taean syngas's flame propagation speed, which contains more CO, must be lower than that of the latter. Hence, this relatively slow reaction resulted in the larger V_{pz} and longer $\boldsymbol{\tau}_{res}$.

For both tested syngases, the concentration of CO was very high, reaching up to 500 ppm or more for lower loads with high nitrogen integration (over 50%), but the concentration decreased sharply for higher loads (down to 10 ppm or less), showing

almost perfect combustion (combustion efficiency > 99.9%). Because the high emissions of CO stemmed from the low mixed mean adiabatic combustion temperature, the nitrogen injection (which quenches flame) can be a main source of high CO emissions for the low load. When increasing the load, enough of the main fuel supply can cause the flame temperature to rise, and thus CO emissions drop to a sufficiently lower level. Fig. 5.7 illustrates the relationship between CO emissions and flame temperature. CO is rapidly emitted when T_{ad} < 1230°C, and this spiking relationship between CO and flame temperature coincides with the results from Yoshimura et al. [30], who reported that CO emissions exponentially increase at T_{ad} < 1500K. By comparing the Buggenum and Taean syngases, we found that the Buggenum syngas is prone to emit more CO. For example, over 1000 ppm of CO is emitted when firing the Buggenum syngas at 40 kW with 150% IR_{N2}. On the other hand, we detected no significant CO emission under the same conditions for the Taean syngas. This discrepancy can be explained by the fact that the Buggenum IGCC plant integrates more nitrogen to control NO_x, as shown in Table 5.1, because the T_{ad} at Buggenum is significantly lowered when IR_{N2} increases, and the slope is steeper than that of the Taean syngas, as shown in Fig. 5.4a.

From the NO_x and CO emission results, we conclude that emissions characteristics highly correlate with flame temperature, which relates to IR_{N2} as well as the H_2/CO ratio. However, even though an increased nitrogen molar concentration should enhance the NO_x formation, according to the extended Zeldovich mechanism, this effect was not significant in our study when compared to the effect of flame temperature. When considering only the H_2/CO ratio, the Taean syngas emitted more NO_x than that of the Buggenum syngas due to a larger $\boldsymbol{\tau}_{res}$, and these emissions were suppressed to under 3 ppm when IR_{N2} was over 50%. On the other hand, when increasing the IR_{N2}, the Buggenum syngas emitted more CO because of a lower flame temperature, and these emissions were suppressed to under 10 ppm when the heat input was over 45 kW.

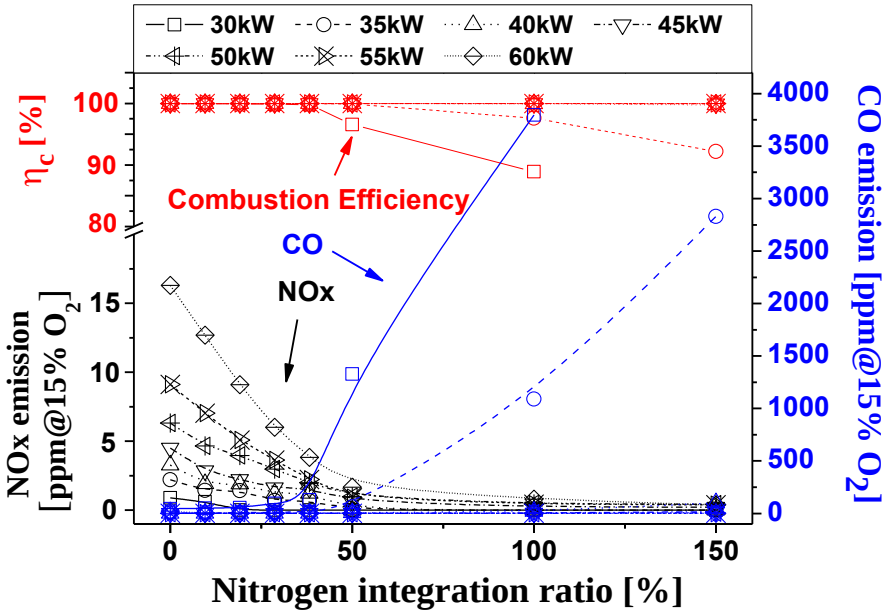

(a) NOx and CO emissions of Taean syngas according to the IR_{N2}.

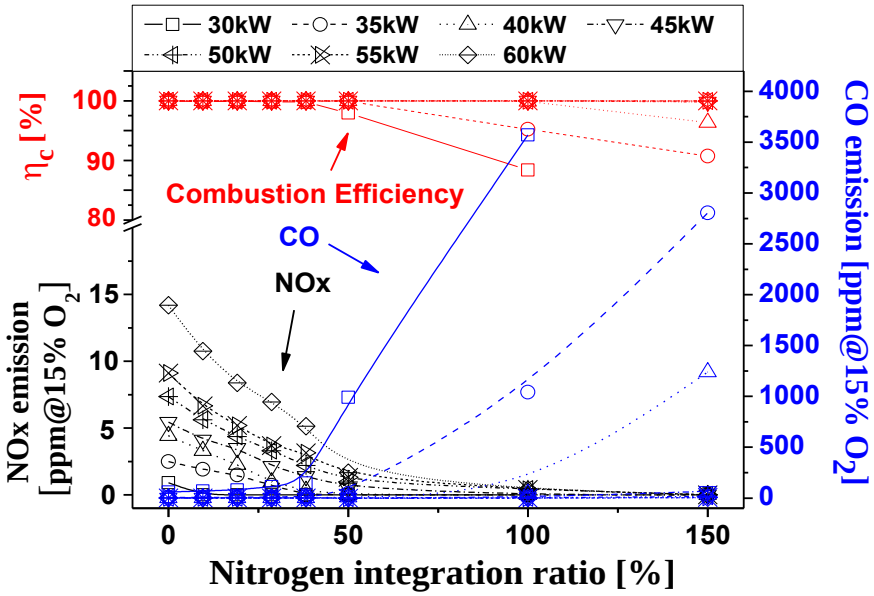

(b) NO_x and CO emissions of Buggenum syngas according to the IR_{N2}.

Fig. 5.4 NOx and CO emissions of Taean and Buggenum syngases.

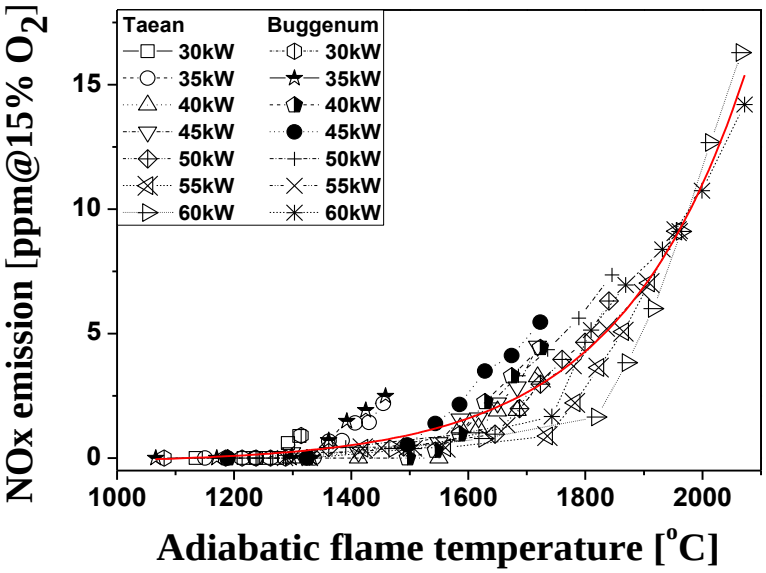

Fig. 5.5 NOx emissions of Taean and Buggenum syngases with respect to T_{ad}.

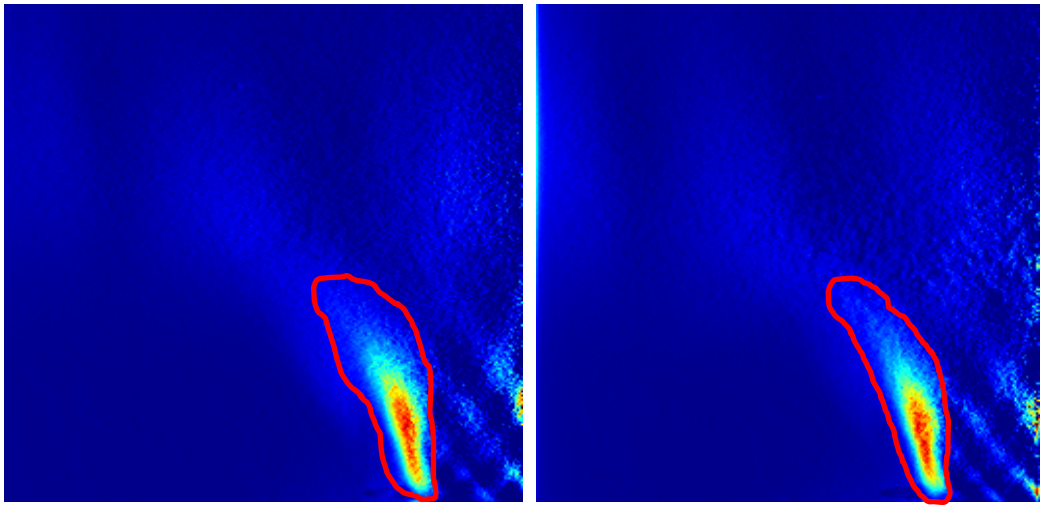

(a) Taean syngas (b) Buggenum syngas

Fig. 5.6 Primary combustion zone of Taean and Buggenum syngases

(left half images of time-averaged Abel-deconvoluted OH^*-chemiluminescence)

Min. Max.

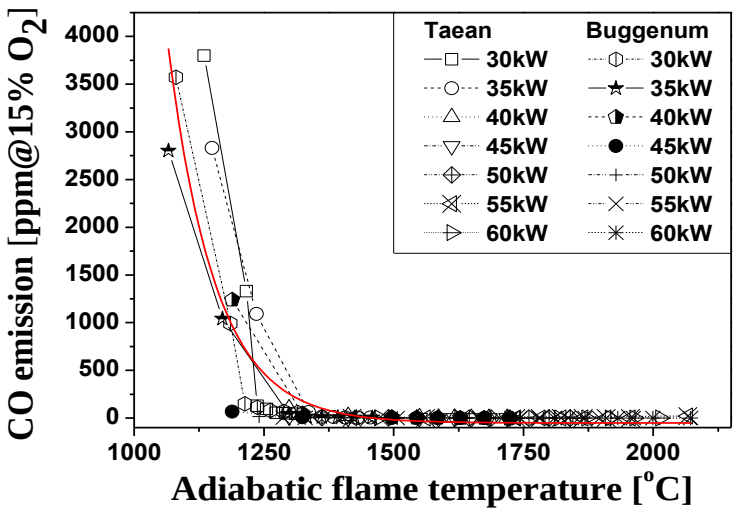

Fig. 5.7 CO emissions of Taean and Buggenum syngases with respect to T_{ad}.

5.1.4 Combustion oscillation characteristics

Fig. 5.8 shows our investigation of combustion oscillations of both syngases with respect to IR_{N2}. The combustion pulsation level was very low in all tests (i.e., almost zero combustion instability occurred without in the case of 35 kW with 100% IR_{N2}). This low fluctuating level is much lower than the oscillation in a standard gas turbine combustor, and it is at least 5% under the control limit for oscillation in a standard turbine combustor. These results are comparable to the results of chapter 4.2.3. To understand why combustion instability did not occur, two mechanisms can be introduced of particular significance in gas turbine combustion systems: oscillation feedback among acoustic pressures, equivalence, and heat release and flame–vortex interaction. In the former mechanism, an acoustic pressure fluctuation in the combustor results in a velocity and acoustic pressure fluctuation at the fuel nozzle, which perturbs the fuel flow rate. This perturbation propagates to the flame, where it produces a heat release oscillation and, in turn, another pressure fluctuation. Herein, heat release oscillation is the periodic repetition of extinction and re-ignition, and a syngas with considerable hydrogen content cannot be easily extinguished, due to the large flammable limit and flame extinction stretch rate of highly reactive hydrogen. Thus, fluctuations in heat release are minimal

and do not cause fluctuations in pressure or fuel flow rate. In the latter mechanism, large-scale, coherent vortical structures cause the rate of heat release to oscillate. These structures are the result of flow separation from flame holders and rapid expansions, as well as vortex breakdown in swirling flows. However, in this study, neither a vortical flame structure at the outer recirculation zone nor flow separation near the fuel nozzle is observed (as shown in Fig. 5.10) since hydrogen causes the flame shape to be diffusive and short. In the case of 35 kW with 100% IR_{N2}, we observed a large amplitude pressure fluctuation in both syngases. Thus, to analyze the oscillation frequency, we plotted Fig. 5.9 by conducting the FFT. The main frequency was 10 Hz, which was due to flame oscillation in regime III, and 300Hz and higher frequencies were fundamental longitudinal frequency and their harmonics. Therefore, only flame oscillation near flame lift-off conditions can be considered as a significant source of combustion instability for both syngases, and flames in regimes I and II were not a concern for thermo-acoustic instabilities.

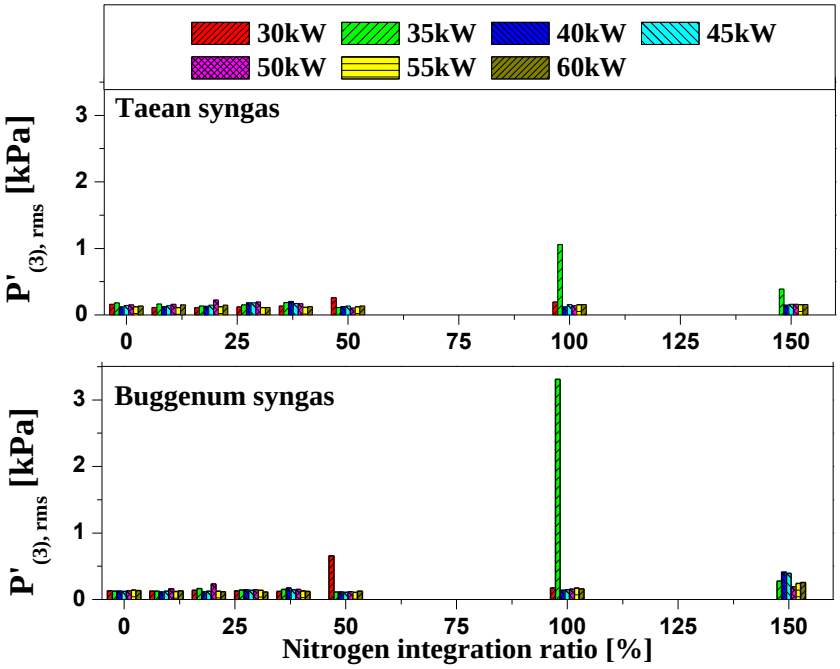

Fig. 5.8 RMS values of pressure fluctuations according to the IR_{N2}.

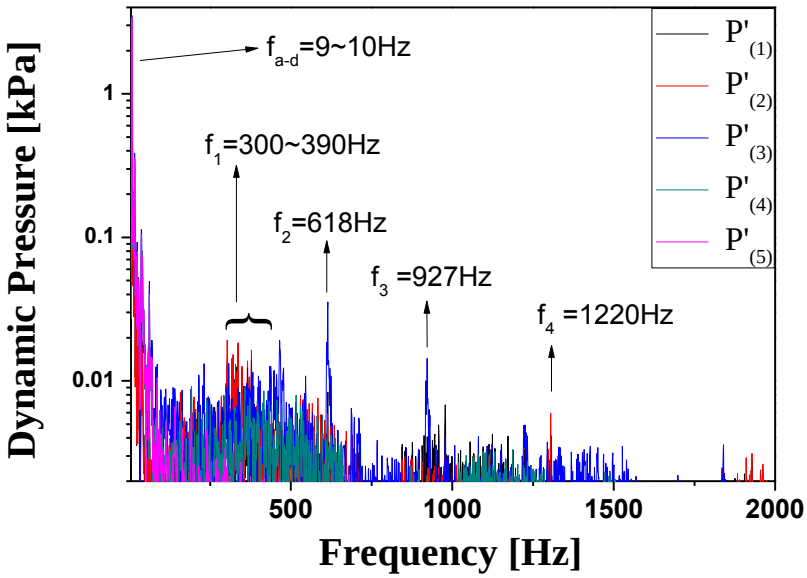

Fig. 5.9 FFT of pressure fluctuations of Buggenum syngas at 35 kW with 100% DR_{N2}.

5.1.5 Flame structures

Fig. 5.10 illustrates the time-averaged OH^*-chemiluminescence images (upper half) and their Abel-deconvoluted images (lower half). Since the flow is assumed to be axisymmetric, only half images are shown. In low heat input conditions, the flame is weak and broader, because the outer recirculating flow can easily affect a flame at a low equivalent ratio. When increasing the heat input, a flame grows larger and stretches downstream, and the primary combustion zone moves to the center due to increased momentum in the downstream direction.

When increasing IR_{N2}, the burning intensity in both syngases diminishes and the flame moves from upstream/center to downstream/outer wall of the combustion chamber, increasing the combustion region. The high temperature combustion region in which the thermal NO_x occurred contracted substantially, but the lower temperature combustion zone expanded. As previously described in subchapter 3.3, these flame structure results coincide with the results of NO_x and CO emissions.

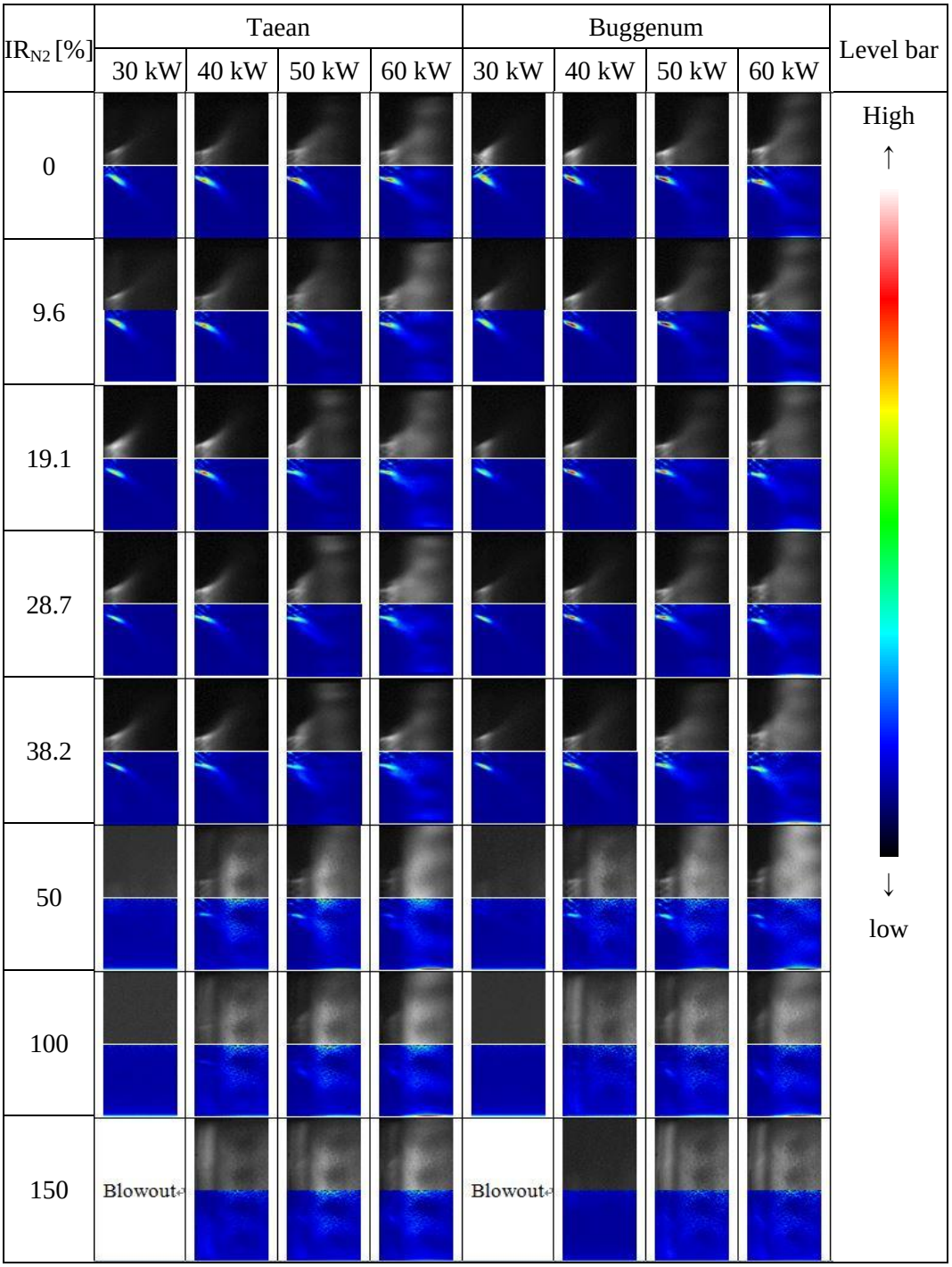

Fig. 5.10 OH*-chemiluminescence and Abel-deconvoluted images of Taean and Buggenum.

5.1.6 Summary and conclusions of coal gas combustion study

From the combustion test results of Taean and Buggenum syngas, we obtained the following conclusions: (1) The flame stability map was plotted by categorizing flames into six regimes according to the flame shape and pressure fluctuation. We observed stable combustion in regimes I and II, into which both Taean and Buggenum syngases fall. Considering only the H_2/CO ratio in the fuel, the Buggenum syngas is more stable. However, considering all aspects, including IR_{N2}, the Taean syngas is more stable. Furthermore, flames from both syngases cannot exist when nitrogen is more than 82 mol%, and this content almost corresponds to the maximum LFL estimated by the Le Chatelier rule. Therefore, we concluded that the lean blowout limit of syngas is predictable by simply calculating maximum LFL, even in the high swirl stabilized flame. (2) Temperature characteristics with respect to IR_{N2} and heat input showed monotonic increasing or decreasing trends, except at some unstable flame conditions. In these unstable conditions, we observed sudden drops and elevations in combustor temperature due to flame movement. This condition should be avoided since it can damage the combustor's liner and transition piece and diminish the lifetime of hot gas path components, including turbine blades and vanes. (3) NO_x and CO emissions highly correlate to flame temperature, and the optimal operating conditions of syngas turbines is determined to be when $1230^oC < T_{ad} < 1500^oC$. Under the same flame temperature, the Taean syngas, which contains more CO in the fuel, emits more NO_x than the Buggenum syngas does, due to a larger $\boldsymbol{\tau}_{res}$ at the former's primary combustion zone. On the other hand, the Buggenum syngas, which contains more diluents, emits more CO because of a lower flame temperature. We verified that fuel-side nitrogen dilution is very effective in suppressing NO_x emission by lowering the flame temperature, and the NO_x emission decreases under 3 ppm when IR_{N2} is over 50%. However, operating with a low load and a high DR_{N2} caused problems with CO emission and flame stability. Thus, the dilution system of an IGCC plant should operate with analysts cautiously monitoring the CO emission and flame stability for better fuel efficiency and plant reliability. (4) Combustion

instability occurred only near regime III due to flame attachment/detachment mechanism. Thus, operating conditions, including IR_{N2}, should avoid this combustion instability. In the other regimes, we did not observe combustion instability for two reasons: 1) lower heat release oscillation and its feedback to pressure fluctuation and 2) flame shape, which does not generate vortical flow. (5) Flame structure was used to analyze the combustion performance test results, such as flame stability, NO_x and CO emissions, combustion efficiency, combustion instability, and temperatures in the combustor. All tested data will be used to determine the optimal operating conditions at the Taean IGCC plant and to analyze the plant's outage.

5.2 SYNTHETIC NATURAL GAS COMBUSTION

A series of SNG fuel was supplied from compressed SNG bombs, of which composition and properties are listed in Table 5.3. C0, C1, C3 and C5 gases have hydrogen concentrations of 0%, 1%, 3% and 5% respectively but their heating values were maintained almost constant by adjusting the propane content. The fuel and air were supplied in the sequence shown in Fig. 5.11. The fuel gas was supplied at the rate of 35~60kW_{th} heat input with a span of 5kW_{th}. In each test condition, flow rates of fuel and air were kept constant for more than 100 seconds to achieve steady state value.

Property	Unit	H_2	CH_4	C_2H_6	C_3H_8	n-C_4H_{10}
density @STP	kg/m^3	0.090	0.715	1.356	2.010	2.48
AF_{st}	L/L	2.38	9.52	16.66	23.80	30.94
AF_{st}	kg/kg	34.32	17.16	16.02	15.60	15.38
LFL	vol %	4	5	3	2.1	1.6
UFL	vol %	75	15.4	12.4	9.5	8.4
HHV	MJ/Nm^3	12.76	39.75	69.64	99.11	128.44
WI	MJ/Nm^3	48.40	53.40	68.35	80.32	90.66
T_{ig} @STP	^oC	500	580	515	480	500
max. S_l in air	cm/s	289	37	40	39-43	43

Table 5.2 Combustion properties of hydrogen, methane, ethane, propane and n-buthane.

Gas or property	Unit	NG	C0	C1	C3	C5
CH_4	vol %	92.5	95.3	93.8	91.0	88.1
C_2H_6	vol %	5.0	0.0	0.0	0.0	0.0
C_3H_8	vol %	1.5	4.7	5.2	6.1	6.9
i-C_4H_{10}	vol %	0.3	0.0	0.0	0.0	0.0
n-C_4H_{10}	vol %	0.3	0.0	0.0	0.0	0.0
i-C_5H_{12}	vol %	0.0	0.0	0.0	0.0	0.0
N_2	vol %	0.4	0.0	0.0	0.0	0.0
H_2	vol %	0.0	0.0	1.0	3.0	5.0
density	kg/m^3	0.774	0.774	0.773	0.772	0.769
HHV	MJ/Nm^3	42.71	42.71	42.71	42.71	42.71
WI	MJ/Nm^3	55.47	55.53	55.1	55.14	55.18
LFL	vol %	4.7	4.69	4.66	4.58	4.51
UFL	vol %	15.06	14.96	15.04	15.19	15.35
AF_{st}	L/L	10.191	10.195	10.188	10.170	10.145

Table 5.3 Chemical composition and combustion properties of tested gases.

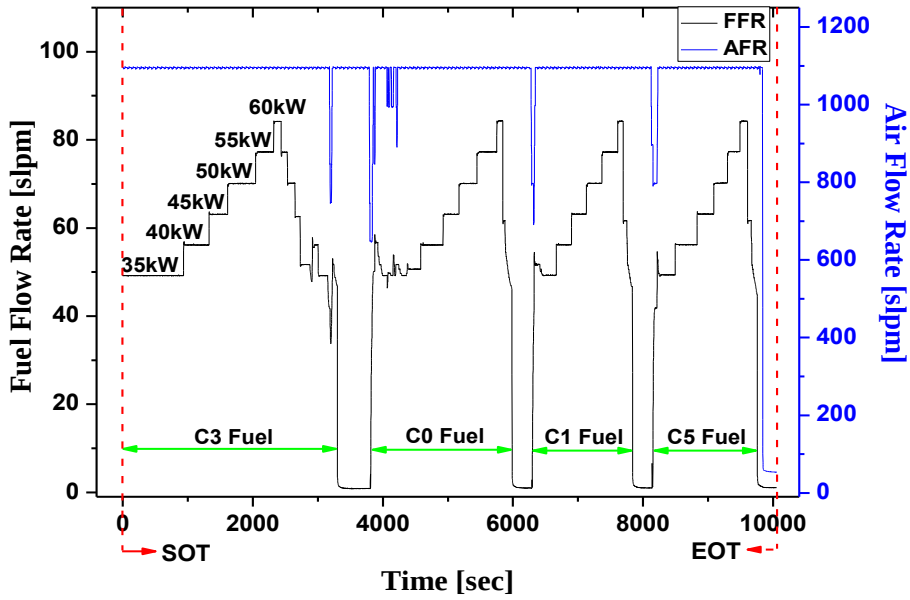

Fig. 5.11 Fuel and air supply sequence.

5.2.1 Temperature characteristics

The temperatures at the fuel nozzle (T_n), dump plane (T_d), and the gas upon exiting the combustion chamber (T_{ex}) were measured regarding the fuel composition and heat input. With these temperatures, the adiabatic flame temperature (T_{ad}) calculated by CANTERA code with GRI 3.0 mechanism was plotted together, as shown in Fig. 5.12. As expected, T_{ex} and T_{ad} show a linearly proportional tendency as heat input increases since flame temperature increases following the rise in heat input. T_{ad} slightly decreased with an increasing hydrogen concentration in the fuel because the overall equivalence ratio of C0 is slightly higher than the C5, even remaining heat input. Lower T_{ad} at the same load can be beneficial in the view of NOx and hot gas path component. That is to say, lowered maximum combustion temperature can lower the emission of thermal NOx and prevents overheating of combustor components such as the chamber liner and fuel nozzle. On the other hand, as a result of having the same amount of heat input, T_{ex} shows almost the same value for all tested SNGs. That is to say, regardless of fuel composition of SNG, same amount of power can be generated by assuming that the gas turbine thermal efficiency is the same since most gas turbines are operated by the turbine inlet temperature (TIT) control.

Meanwhile, T_n shows a downward tendency with respect to heat input. This tendency is due to enhanced heat transfer from heated nozzle to fuel gas. Namely, the temperature of the nozzle is lowered by a higher flow rate of SNG more so than it is raised by radiation. When the hydrogen content of fuel is changed, no significant changes in T_n are observed. The important implication of this result is that the probability of occurrence of flash back, which is considered to be significant operability issues in combustion of hydrogen enriched fuel, is extremely low when firing SNG in a gas turbine.

T_d shows neither upward nor downward tendency but a small difference is observed at 50kW$_{th}$. This phenomenon can be explained with the result of dynamic pressure. T_d is mainly affected by the outer recirculation flow which is the main source of combustion instability according to the flame-vortex interaction mechanisms. As shown in Fig. 5.14, a

difference in pressure fluctuation among SNGs at 50kW$_{th}$ results in a difference in outer recirculation flow at dump plane, hence the difference in T_d.

To sum up the temperature results of SNGs, no harmful effect was observed with respect to flash back or overheating of the combustor and only a trivial difference in T_d was observed.

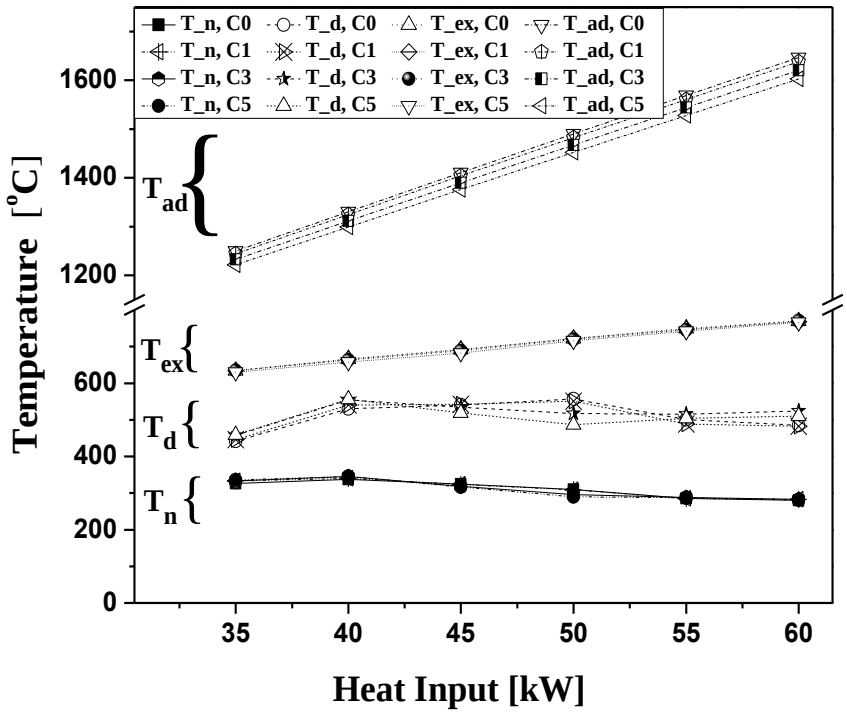

Fig. 5.12 Temperatures of combustor with respect to relative power output.

5.2.2 CO and NO$_x$ emission characteristics

Fig. 5.13 presents the CO and NO$_x$ emission characteristics of C0, C1, C3 and C5 gases with respect to heat input from 35kW$_{th}$ to 60kW$_{th}$. For the heat input range above 40kW$_{th}$, CO was emitted at a sufficiently low level of 2 ppm or below. This result can be explained together with the previously described temperature results shown in Fig. 5.12. The lower temperature of combustion slows down the oxidation of SNG and causes

incomplete combustion. According to the Yoshimura et al. [65], CO concentration starts to grow rapidly in exhaust gas when adiabatic flame temperature is under 1500K in lean premixed gas turbine without pilot fuel. Their results correspond well with the present result of 35kW$_{th}$, at which T_{ad} was under 1230°C. Therefore, we can conclude that CO emission stems from the low mixed mean adiabatic combustion temperature less than 1500K approximately. However, CO emission of 35kW$_{th}$ does not seem to be significant because the emission level was under 15ppm in low load, while over 99.8% combustion efficiency was achieved. NOx emissions show a tendency to increase as the heat input increases. This result matches well with Zeldovich's NOx mechanism, where the flame temperature increases as more fuel is added to the combustor in fuel-lean condition. Little difference is observed in both CO and NOx emissions from various SNGs, and, thus, we can conclude that SNG is safely applicable to the gas turbine based on the results regarding the emissions.

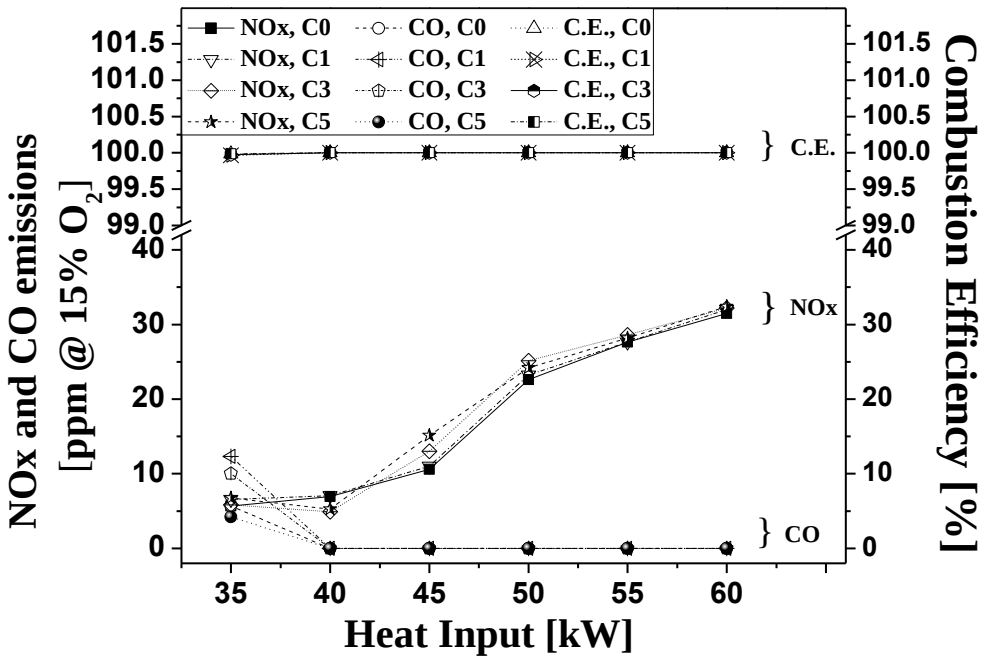

Fig. 5.13 CO and NO_x emissions of C0, C1, C3 and C5 gases with respect to heat input.

5.2.3 Combustion oscillation characteristics

Fig. 5.14 shows the root mean squares (RMS) value of the dynamic pressure fluctuation at the dump plane ($P'_{(1)}$), and the combustion chamber liner ($P'_{(2)}$). Similar trend and value were observed between C0 and C1 (group I) and also between C3 and C5 (group II), while the two groups differed from each other. Group I was higher than group II at 50kW$_{th}$ and on the contrary, group II was higher than group I at 55kW$_{th}$ and 60kW$_{th}$. In the former group, as previously explained in subchapter on emission, more intense evolution of outer recirculating flame vortex generated by higher pressure fluctuation heats up the dump plane more, hence showing higher T_d. Normally, synthetic gas that contains considerable amounts of hydrogen cannot be easily extinguished because hydrogen has a high flammable limit, as shown in Table 1, and cannot be blown out even in large flame stretches. However, the result of pressure fluctuation of SNG does not fully correspond with this characteristic of hydrogen. The higher fluctuation in higher load in group II cannot be easily explained in this manner. The characteristic of combustion instability is very sensitive to the fuel composition since small variation in fuel can alter the phase difference between heat release and dynamic pressure. The phase difference between pressure and heat release ($\theta_{p'-q'}$) will be discussed in detail later. The frequency characteristics of pressure fluctuation for group I and group II are also compared in Figs. 7 and 8. As the amplitude of pressure fluctuation and frequency characteristics of C0 and C1 were very similar, and those of C3 and C5 were similar. Thus the frequency domain plot of C1 and C3 was omitted in this paper. In both groups, the fundamental frequency increased as the heat input increased. These results can be simply explained by the longitudinal mode frequency equation of Eqn. (3) and (4) under some reasonable assumptions [82].

$$\text{Frequency} = \frac{(2n-1)\,c}{4L}\ ,\ \ n = 1, 2, 3, \ldots \quad \text{(cloed-open system)} \tag{5.4}$$

where c and c_o are sonic velocity in the air at the temperature of T ^{o}C and 0 ^{o}C respectively. Herein the combustion chamber of this study can be assumed as a closed-open system since one side of combustion chamber is enclosed by dump plain and

another is opened to the atmosphere. An increase in the heat input elevated the T_{ad} results to the higher sonic velocity, resulting in higher frequency. The pressure wave of closed-open system oscillates in quarter wave mode; exit of combustor and dump plane can be considered as a node and an anti-node of pressure respectively. Thus $P'_{(1)}$ is almost two times higher than the $P'_{(2)}$. Small upward shift of frequency is observed at each heat input when comparing C5 with C0. But the changes are very small since the combustion temperatures of both groups are almost the same.

Next, the heat release oscillation (q') of C0 and C5 gases, synchronized with $P'_{(1)}$ signal, was investigated. Heat release oscillation was calculated from the OH^*-chemiluminescence image and both q' and $P'_{(1)}$ were normalized to compare the phase difference only. As shown in Figs. 9 and 10, q' led $P'_{(1)}$, the phase gap ($\theta_{p'-q'}$) of C5 is slightly smaller than that of C0. This might be due to the nature of hydrogen toward fast oxidation and its accelerated chain reaction, which shortens the total chemical reaction time and consequently the phase gap. The aforementioned differences were very small and other significant difference could not be found in regard to either the amplitude or the frequency of pressure fluctuation. However, since the combustion instability is very difficult to predict in a real engine and this poses a fatal risk of failure, careful monitoring of combustion pulsation is necessary during operation.

5.2.4 Flame structures and heat release oscillation

Using measurements of intensified high speed camera and OH filter, flame structures were investigated, as shown in Fig. 5.19. For all tested gases, the flame evolution and decaying could be closely observed with respect to the phase angle. As the hydrogen content was increased, a slight delay of flame regeneration was observed between 270° and 330°, which can be attributed to the aforementioned fact that adding hydrogen delays ignition time [62]. An increased concentration of hydrogen may also cause rapid burning, but this phenomenon was not observed using Fig. 5.19 only. As previously mentioned in the subchapter on combustion oscillation, the frequency of heat release and pressure

oscillations of C5 were higher than that of C0 by approximately 10 Hz. This means if there is high hydrogen concentration in SNG, it starts to burn later but reacts faster, and this fast burning characteristic shortens the cyclic period by approximately 0.3 msec, 5% of periodic time, i.e. 5% higher frequency in C5.

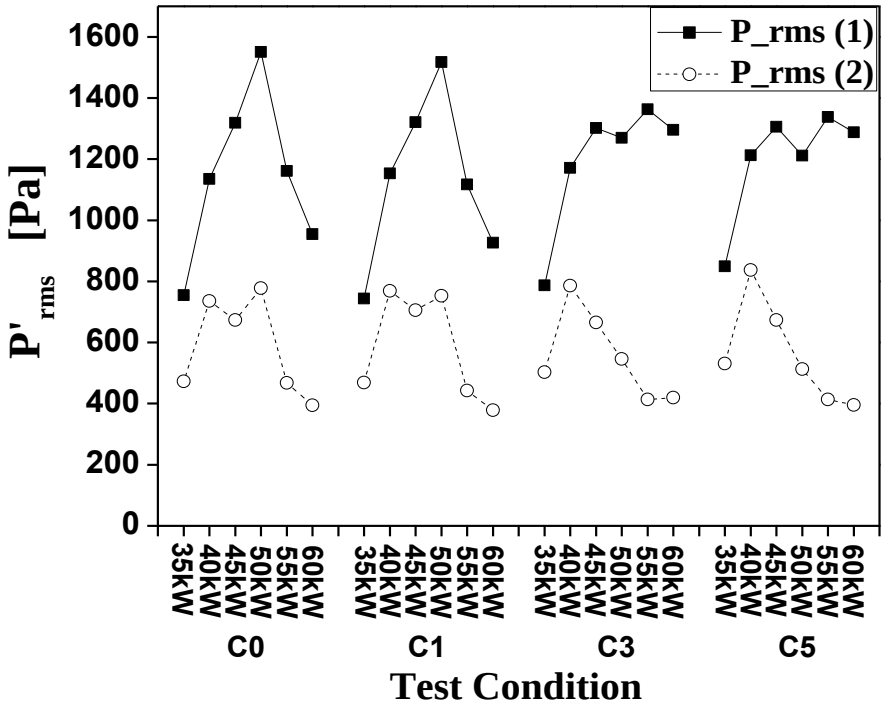

Fig. 5.14 Pressure fluctuations of C0, C1, C3 and C5 gases with respect to heat input.

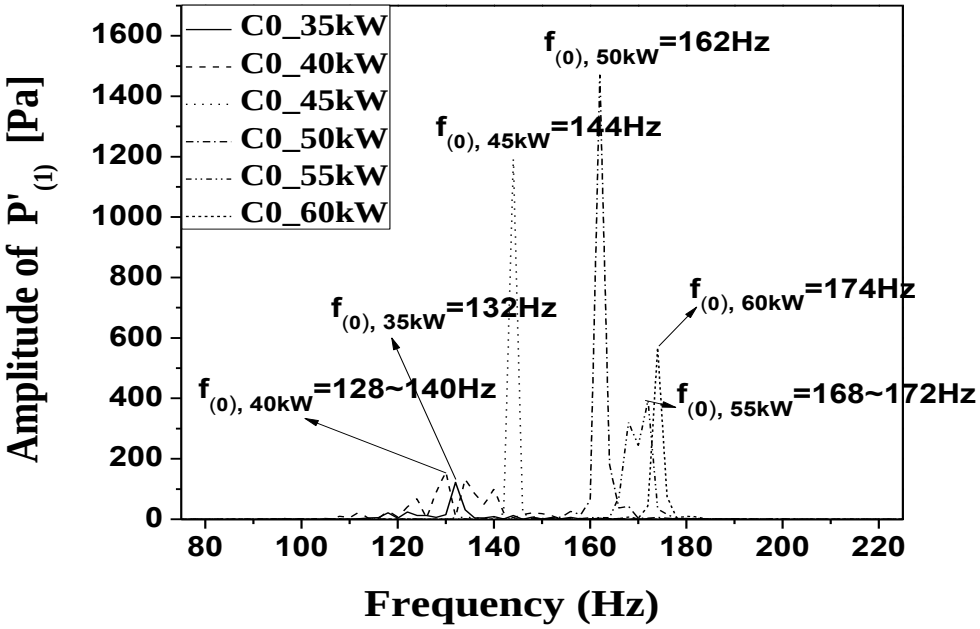

Fig. 5.15 FFT results of pressure fluctuations with respect to heat input of C0 gas.

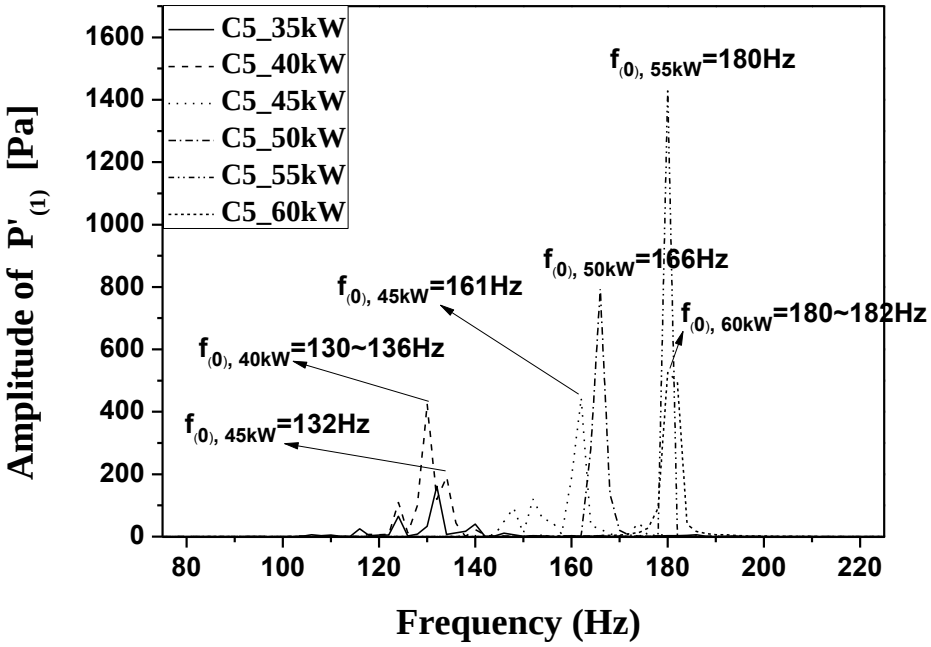

Fig. 5.16 FFT results of pressure fluctuations with respect to heat input of C5 gas.

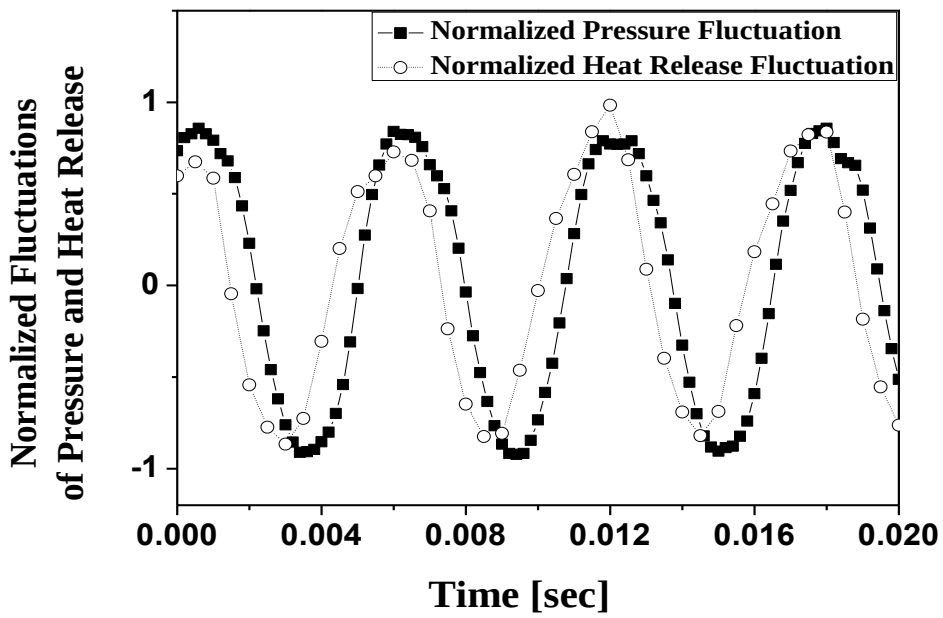

Fig. 5.17 Normalized fluctuations of pressure and heat release at 60kW$_{th}$ heat input of C0 natural gas.

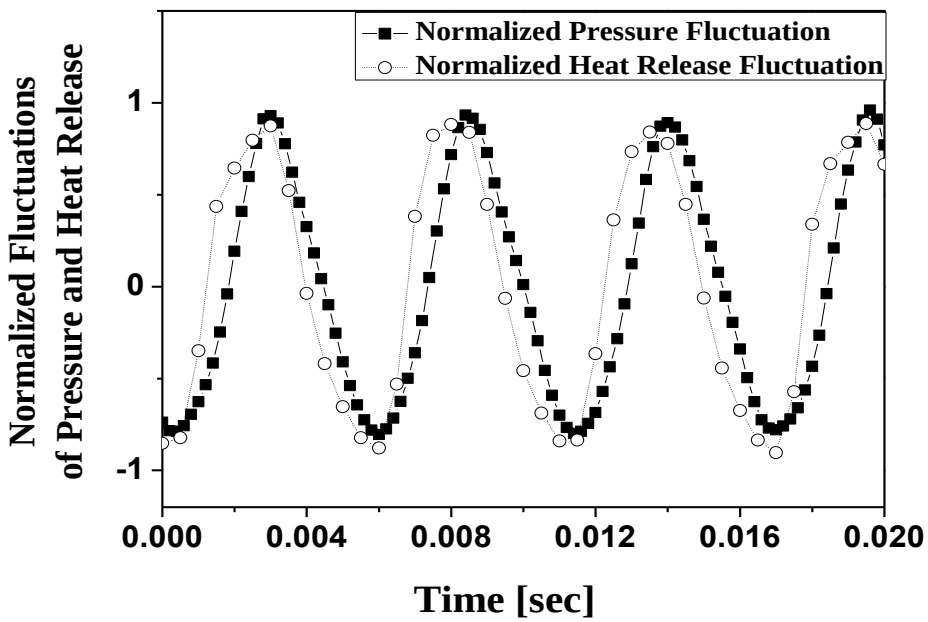

Fig. 5.18 Normalized fluctuations of pressure and heat release at 60kW$_{th}$ heat input of C5 natural gas.

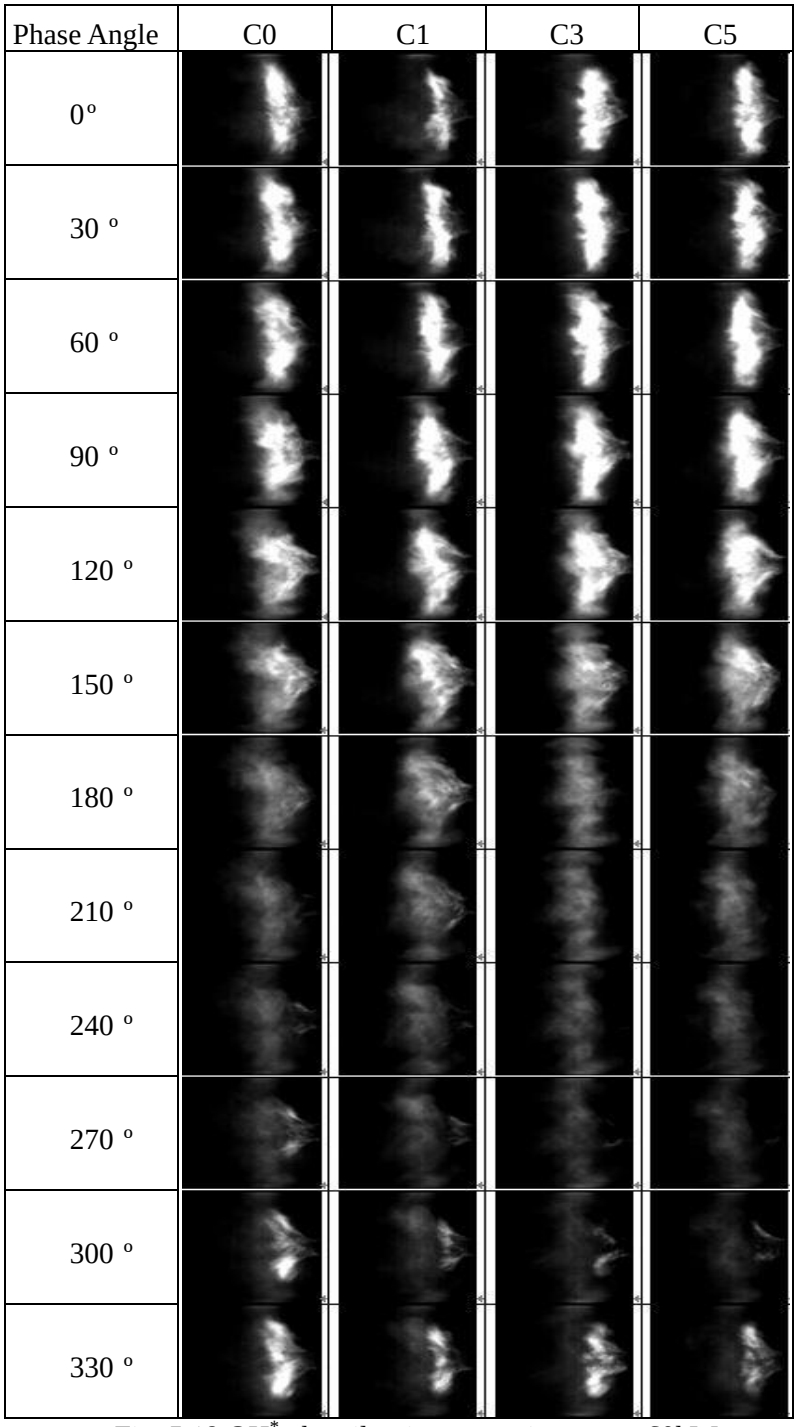

Fig. 5.19 OH^*-chemiluminescence images at $60kW_{th}$.

5.2.5 Summary and conclusions of SNG combustion study

The combustion characteristics of SNGs have been investigated when with varying hydrogen concentrations, from 0% to 5%. The experimental results led to the following conclusions:

(1) The hydrogen content in synthetic natural gas has a nonlinear effect on the combustion characteristics, but the trends can be explained based on the combustion properties. The combustion properties of SNG with higher hydrogen content include faster burning velocity, longer ignition delay time, lower adiabatic flame temperature and larger flammable limit, and their effects on the gas turbine combustion characteristics are schematized in Fig. 5.20.

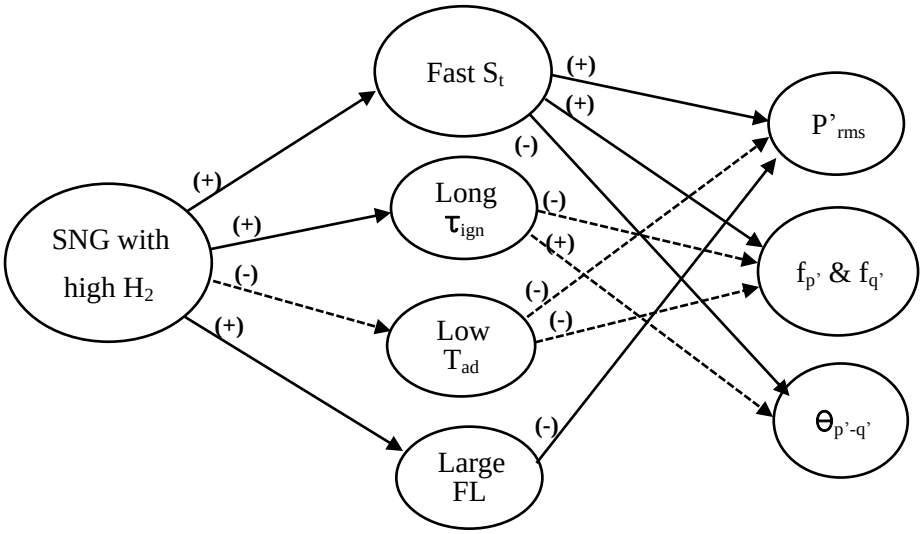

Fig. 5.20 Cause and effect diagram for the relationship between combustion properties in SNG and gas turbine combustion characteristics. (+): positive effect, (-): negative effect, dashed line: weak effect.

(2) There were no differences in the combustion characteristics observed between C0 and C1, which confirms that the effect of hydrogen in SNG on gas turbine combustion is

negligible for cases where the hydrogen content is below 1%. In addition, C0 and C5 show a slight difference in terms of combustion instability such as amplitude and frequency of pressure fluctuation, but other characteristics such as temperature and emissions of NOx and CO were almost same. From these results, we concluded that the synthetic natural gas containing hydrogen of under 1% is adaptable without retrofitting of any combustor parts. Korea coal-SNG Quality Standard Bureau is planning to supply SNG for power generation, guaranteeing hydrogen content of under 1%.

(3) To clearly verify whether SNG can be safely and reliably adapted to gas turbine, more long term combustion tests are necessary with the assessment of the lifetime of hot gas path components such as combustor head, combustion liner, transition piece, and turbine blades and vanes.

CHAPTER 6
CONCLUSION

In this study, the temperatures of flame and combustor, NO_x/CO emissions, combustion instability, flame stability, and flame structures of various compositions of H_2/CO/CH_4 syngas are investigated in a PPM GTMC, which can prevent flashback problem even in high hydrogen content, to understand the combustion characteristics of new fuel for IGCC and SNG plant. In order to identify the detailed flame structure during combustion instability, OH^*-chemiluminescence images were taken at the rate of 12500 frame/sec using the high-speed intensified ICCD camera and/or planar OH^* distribution in flame was obtained using phase-locked OH^*-PLIF setup.

First, the fuel composition effects of H_2/CO/CH_4 syngas (0~100%, span: 12.5% by LHV) on trends of each combustion performance were investigated by using ternary diagram. A lot of NO_x is emitted at high H_2 composition due to high flame temperature and high CO composition due to long residence time. This feature could be also explained by flame structure and combustor temperature. H_2/CH_4 syngas flame generated high combustion instability at the frequency of 750 Hz, 1000 Hz and 1500 Hz correspond to 3L, 4L and 6L mode which varies according to the fuel composition. This self-excited high multi-mode combustion characteristics have been studied by investigating combustion properties, flame structure, Rayleigh indices, POD and characteristic time scales from the images of high-speed chemiluminescence and OH^*-PLIF. The flames have different shapes and generate different CI frequency at near 4L or 3L mode with their harmonics. The CI frequency which is non-linear for fuel composition was appeared to be linearly proportional to T_{ad} and S_L. Phase-synchronized OH^*-PLIF images suggested clues of an important CI driving mechanism including the periodic alternation of flame attachment/detachment and coupling of vortex with everlasting heat release at the ORZ due to high reactivity of high hydrogen fuels. These images also used for the precise calculation of 2-D flame length by obtaining centroid of heat release intensity when

performing time-lag analysis. The RI results notified the dependence of the location and intensity of CI driving/damping on the fuel composition and instability mode. For higher H_2 containing flame (4th mode), driving and damping is occurred in narrow region but with high heat release density and the frequency of RI was doubled. Otherwise in case of 3rd mode RI shape was similar with pressure fluctuation due to the characteristics of multi-mode CI with high superposition of higher harmonics. Analysis of POD from high-speed OH* images showed the distinct coherent structures and large roll-up of flame are responsible for generating flame oscillations for each mode. High cross-correlation was found between POMs of 4th mode indicating convection of these coherent structures. When conducting TLA for syngas in a PPM GTMC, the significance of skewness time induced by wave distortion and importance of careful inspection on L_{flame} using 2-D OH^*-PLIF is verified by showing the improvement in prediction accuracy.

Next, the effect of the fuel-side dilution of N_2, CO_2 and steam on the combustion characteristic of syngas has been studied. This fuel-side dilution reduced flame temperature, combustor temperature and consequently NO_x but significantly increased CO emission due to incomplete combustion at low flame temperature. From the NO_x results of each diluent, it can be obtained that the dilution of syngas with nonflammable gas decreases NO_x emissions, and the amount of NO_x reduction per unit power is logarithmically related to only the diluent's heat capacity which is the product of mass flow rate of the diluent and constant pressure heat capacity. This relationship between NO_x reduction and diluent heat capacity is verified by inducing analytic solutions with some appropriate assumptions.

Finally, based on the combustion results of $H_2/CO/CH_4$ syngas with N_2/CO_2/steam dilution, the combustion tests were performed for the commercial fuels: coal-derived syngas and SNG. The results of coal gas of which H_2/CO ratio is 1/2 showed that N_2 dilution is appeared to be negative in view of flame stability and CO emission but can be operable with enough stability margins and to be very positive in view of NO_x emission. Combustion test of C0, C1, C3 and C5 SNGs of which H_2 content is 0%, 1%, 3% and 5% but Weber index is constant was performed. Combustion characteristics of temperature

and NO_x/CO emission were almost identical for all SNGs but combustion instabilities of C0 and C1 were slightly differed from that C3 and C5 in frequency as well as amplitude. This feature also closely visualized by examining the high-speed unsteady flame behaviors. Even though the impact on combustion instability is not so significant for SNG which contains over 1% H_2, this 1% where the change of combustion starts can be provided as the quality standard in SNG considering the existence of various types of natural gas firing gas turbines.

APPENDICES

APPENDIX A. CALCULATION OF ADIABATIC FLAME TEMPERATURE

- Calculation Program : Matlab with CATERA code
- Chemistry Set : GRI 3.0 Mechanism

The Matlab code for the calculation of adiabatic flame temperature of syngas is provided as below.

```
%% Initial setting
clear all
close all
clc
Po = 100000;                                    %    [Pa]
gas      = IdealGasMix('gri30.xml');
N          = nSpecies(gas);
iCH4    = speciesIndex(gas,'CH4');
iH2      = speciesIndex(gas,'H2');
iCO      = speciesIndex(gas,'CO');
iC3H8 = speciesIndex(gas,'C3H8');
iCO2    = speciesIndex(gas,'CO2');
iO2      = speciesIndex(gas,'O2');
iN2      = speciesIndex(gas,'N2');
iH2O      = speciesIndex(gas,'H2O');

%% Syngas Adiabatic Temperature Calculation
  Temp_ad = zeros(7,6);
  DR = [0 9.56 19.12 28.67 38.23 50 100 150];
```

```
for c = 1 : 1 : 7                          % 30kW, 35kW, 40kW, 45kW, 50kW, 55kW,
60kW
    for d = 1 : 1 : 8                      % Nitrogen dilution ratio for Taean Syngas
H2=12.8%, CO=31.4%, N2=50.7%, CO2=0.4%, H2O=4.3%
        a=c+5;                             % DR 0% 9.56% 19.12% 28.67% 38.23% 50.00%
100.00% 150.00%
        fgas = zeros(1,N);                 % Fuel
        LHV_Syn = 5.36;                    % LHV of Buggenum Syngas, MJ/Nm3
        LHV_CH4 = 35.9;                    % LHV of CH4, MJ/Nm3
        fgas(iH2) = (a*5)/LHV_Syn*60*0.128;          %    flow rate of H2, slpm
        fgas(iCO) = (a*5)/LHV_Syn*60*0.314;          % flow rate of CO, slpm
        fgas(iN2) = (a*5)/LHV_Syn*60*0.5641*DR(1,d)/100;          % flow rate of
N2, slpm, N2 equivalent dilution ratio
        T_3 = 273.15+10;                           % fuel temp=10oC
        P_3 = Po;                                  % ambient pressure test
        set(gas,'T',T_3,'P',P_3,'X',fgas);
        %M_reac = meanMolarMass(gas);                    % obtaining mean molar
weight
        h_reac_3 = enthalpy_mole(gas)*(sum(fgas));         % enthalpy per mol is used,
enthalpy_mole is also available
        agas = zeros(1,N);                         % Air
        agas(iO2) = 930.2*0.21;                    % flow rate of O2, slpm
        agas(iN2) = 930.2*0.79;                    % flow rate of N2, slpm
        T_4 = 273.15+200;                          % air temperature 200oC
        P_4 = Po;                                  % ambient pressure test
        set(gas,'T',T_4,'P',P_4,'X',agas);
        M_reac = meanMolarMass(gas);                    % obtaining mean molar weight
        h_reac_4 = enthalpy_mass(gas)*M_reac*(sum(agas));          % obtaining
mean molar weight
```

```
            h_reac_1=h_reac_3+h_reac_4;
            pgas = zeros(1,N);                                  % flow rate of product Gas
            pgas(iCO2) = fgas(iCO)+fgas(iCO2)+fgas(iCH4);
            pgas(iN2) = fgas(iN2)+agas(iN2);
            pgas(iH2O) = fgas(iH2)+fgas(iH2O)+2*fgas(iCH4);
            pgas(iO2) = agas(iO2)-(0.5*fgas(iH2)+0.5*fgas(iCO)+2*fgas(iCH4));
            set(gas,'T',1000,'P',P_4,'X',pgas);
            M_prod = meanMolarMass(gas);
            set(gas,'H',h_reac_1/(sum(pgas))/M_prod,'P',P_4,'X',pgas);    % sum of flow
rates of product gases
            Temp_ad(d,c) = temperature(gas)-273.15;        %    K -> oC
        end
end

test_condition = input('input file name: ','s');
result_file_name = sprintf('%s.txt',test_condition);
data_save=fopen(result_file_name,'wt');                                    % input matrix
            [Rowsize,Columsize]=size(Temp_ad);
            for k = 1 : 1 : Rowsize
                for kk = 1 : 1 : Columsize
                    fprintf(data_save, '%10.2f\t', Temp_ad(k,kk));
                end
                fprintf(data_save,'\n');
            end
            fclose(data_save);    % data_save and close file
% result_4 = sprintf('2.32 adiabatic flame temperature = %.5g [K]',Temp_ad);
disp('Syngas adiabatic temperature calculation')
disp(' ')
disp('- END -')
```

APPENDIX B. CALCULATION OF IGNITION DELAY TIME

Ignition delay time of syngas was calculated using CHEMKIN-Pro program. Detailed setting for the calculation is provided as below. This simulation is assumed that homogeneous mixture is in rapid compression machine (RCM).

- Calculation Program : CHEMKIN-Pro
- Reactor Model : Closed Homogeneous Batch Reactor
- Chemistry Set : Aramco Mechanism
- Problem Type : Constant Volume and Solve Energy Equation

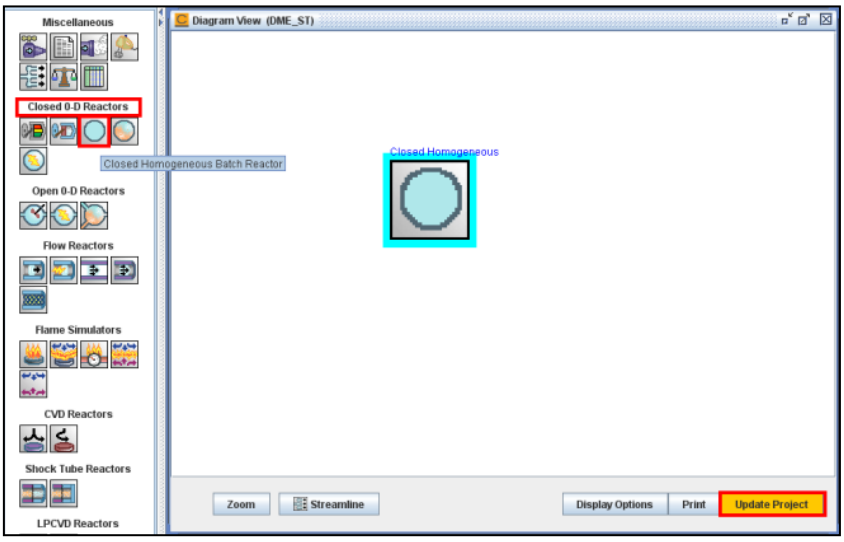

Fig. B.1 Configuration of reactors in CHEMKIN for the calculation of ignition delay time.

From the calculation results, time-series variations of pressure, temperature and CH^* can be obtained as shown in Fig. B. 2a and 2b. Time derivative of them are shown in Fig. B. 2c and 2d of which maximum is identical to the rising time of temperature, pressure and CH^*. The ignition delay time is determined at the moment of maximum temperature and pressure.

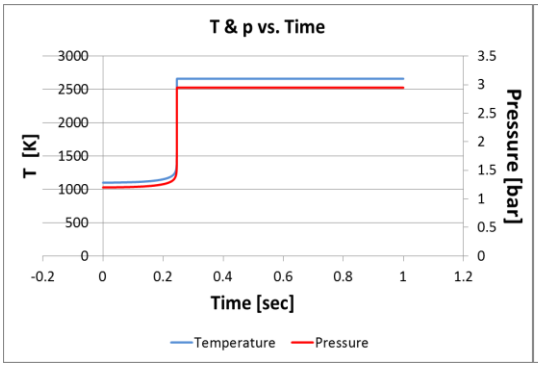

(a) Temperature and pressure

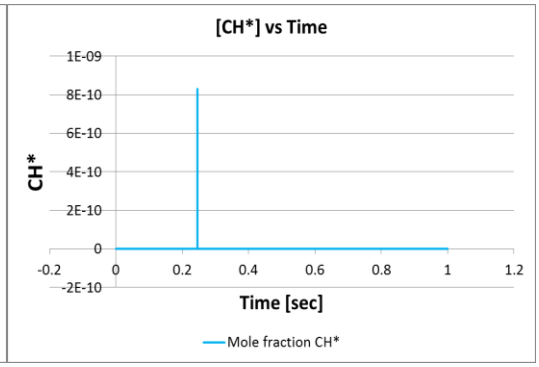

(b) CH^*

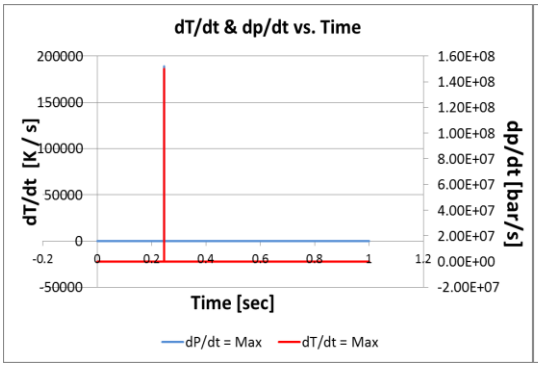

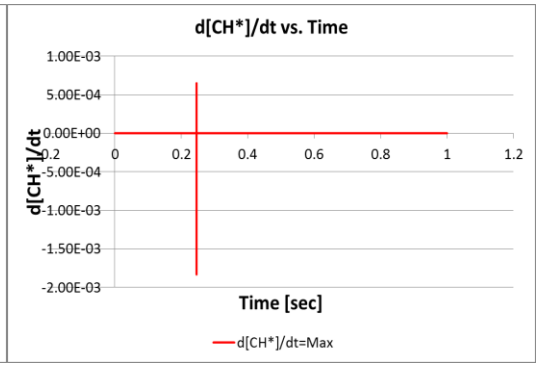

(c) Time derivative of temperature and pressure in RCM (left)

(d) Time derivative of CH^* in RCM (right)

Fig. B. 2 Results of the CHEMKIN simulation for the calculation of ignition delay time.

APPENDIX C. CALCULATION OF LAMINAR FLAME SPEED

Ignition delay time of syngas was calculated using CHEMKIN-Pro program. Detailed setting for the calculation is provided as below.

- Calculation Program : CHEMKIN-Pro
- Reactor Model : Flame Speed Model (same Governing Equation with Premixed Flame Model)
- Chemistry Set : GRI 3.0 Mechanism
- Problem Type : Constant Pressure and Solve Enthalpy Equation

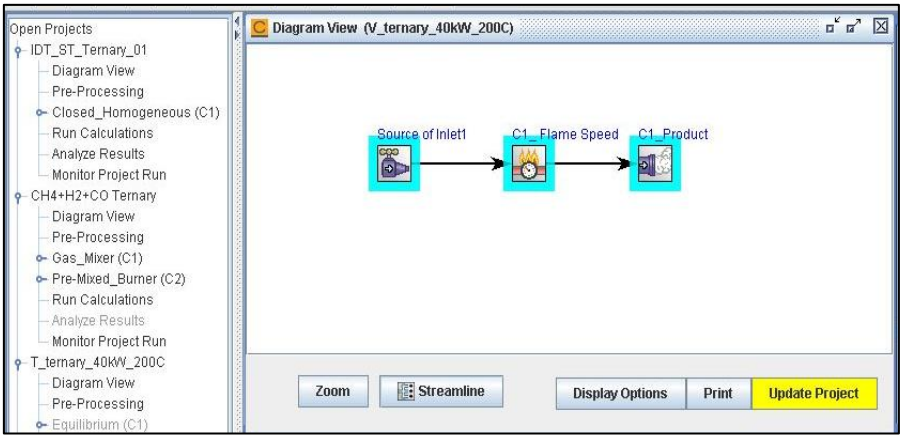

Fig. C.1 Configuration of reactors for the calculation of laminar burning velocity.

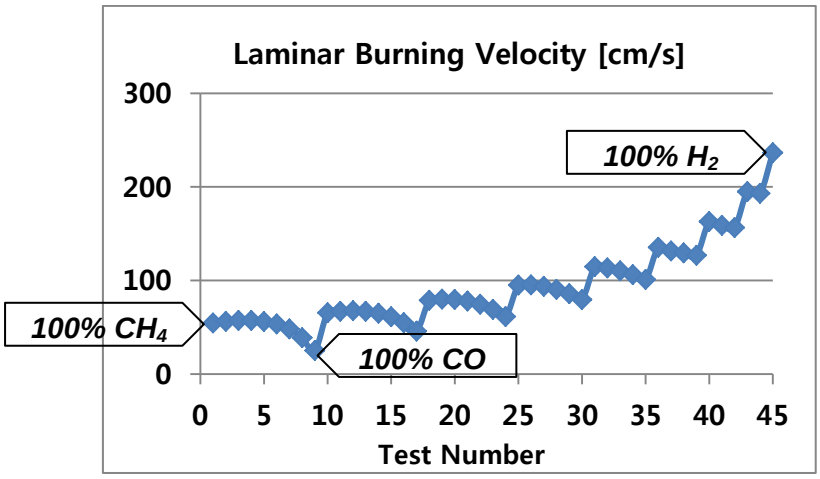

Fig. C.2 Laminar burning velocity with respect to test number from 1 to 45.

APPENDIX D. ANALYSIS OF PROPER ORTHOGONAL DECOMPOSITION

The POD technique provides a linear approximation of a set of functions that enable an easier characterization of the complex original input data as a sum of weighted basis functions. [36, 76]. This POD has evolved into a valuable tool for investigating coherent structure of unsteady flame. In this study, the construction of the POD was performed by the snapshot methods. Decomposition of snapshot images from high-speed OH^*-chemiluminescence was used for this study and a sample code written in MATLAB. These images were considered as a collection of data with elements $\{x_i\}$, where i=1,2,…,N, of m by n pixels belongs to a linear metric space Ω with inner product.

$$< x, y > \; = \int x(s)y(s)ds, \qquad x, y \in \Omega \tag{D.1}$$

where <x,y> is the L2 inner product $\sum_j \sum_j x(j,k)\, y(j,k)$. The 0-th POM is the average.

$$\varphi_0 = \frac{1}{N}\sum_i^N x_i \tag{D.2}$$

The modes are obtained from the N x N correlation matrix K with entries.

$$K_{i,j} \; =< x_i, x_j > \tag{D.3}$$

where $\tilde{x}_i = x_i - \varphi_0$ is the deviation from the averaged image φ_0 .Then the eigenvector problem can be contructed like below:

$$Kv_r = e_r v_r \tag{D.4}$$

The solution of this eigenvector problem is N eigenvalues, $e_1 \geq e_2 \geq \ldots \geq e_2$. From each eigenvalue pair, the mode φ_r is constructed by linear combination of the N images,

$$\varphi_r = \sum_{i=1}^N v_{r,i} x_i, \qquad r = 1,...,N \tag{D.5}$$

The projection of $\{\tilde{x}_i\}$ onto φ_r generates the series

$$a_{r,i} =< x_i, \varphi_r >, \qquad i = 1,...,N \tag{D.6}$$

Data reduction is achieved by taking only the first M modes, M < N.

$$Z_{M,i} = \varphi_0 + \sum_{r=1}^{M} a_{r,i}\varphi_i \tag{D.7}$$

For continuous images obtained at a certain sampling rate, $a_{r,i}$ can be interpreted as a time series for mode φ_r from which power spectral density can be deduced to investigated if a dominat frequency f_r exists for the pattern represent by mode r. Additionally, cross correlation was performed to infer the underlying physical process associates with various modes such as flame propagation with convection flow.

Above mentioned algorithm is programmed by Matlab. The code was established by revising the code of Ref. [76]. Collection of data was converted from vector quantities distributions to scalar quantities distributions and additional cross correlation is performed as given below.

```
%%   POD Program coded by Min Chul Lee at SNU by revising the code of Hao Chen et al.
%%   Initial Setting
clear all
close all
clc
path = pwd;
mkdir ('resultPOD2');
files = dir;

%% RI Calculation
k=0;
n_snapshots = 5000;
for i=1: 1: 512
    for j=1: 1: 256
        k=k+1;
```

```
            x(1,k)=i;
            y(1,k)=j;
        end
    end
    for j = 1 : n_snapshots
        data_origin = importdata(files(j+3).name);                    % recall image file
        data_new = double(data_origin.cdata);          % change file format (uint8 ->
double)
        k=0;
        for x1= 1: 1: 512
            for y1 = 1:1:256
                k=k+1;
                U(j,k) = data_new(x1,y1); % u velocity
            end
        end
    end

    % Section 2 --Compute spatial correlation matrix C
    c1 = U*U';
    C = (c1)/n_snapshots;

    % Section 3 -- Solve the eigenvalue problem: C * EigenVector = EigenValue *
EigenVector
    [beta,lmd] = svd(C);

    % Section 4 -- Calculate basis functions
    phix = U'*beta;

    % Normalize basis functions
```

```
GridNum = size(x,2);
for j=1:n_snapshots
    PhiNor = 0;
    for i=1:GridNum
        PhiNor = PhiNor + phix(i,j)^2;
    end
    PhiNor = sqrt(PhiNor);
    phix(:,j)= phix(:,j)/PhiNor;
end

% Section 5 --? Calculate coefficient
TimCoeU = U*phix;
TimCoe = TimCoeU;
for z=1:n_snapshots
    k=0;
    for x2 = 1 : 512
        for y2 = 1: 256
            k=k+1;
            ReFig(x2,y2,z) = phix(k,z);
        end
    end
end

%% Section 6 --? Export basis functions
for mode_num=1:1:1000
    %figure(mode_num)
    contourf(ReFig(:,:,mode_num), 30);
    axis([1 256 1 512])
    h1 = findobj('Type','patch');
```

```
        set(h1,'LineWidth',0.2)
        h2= colorbar('location','EastOutside');
        set(h2,'fontsize',10,'fontWeight','bold');
        figureHandle = gcf;
        set(findall(figureHandle,'type','text'),'fontSize',15,'fontWeight','bold')
        file_name_save=sprintf('%s/resultPOD2/C30_%s.tiff',path,
num2str(mode_num));
        print ('-dtiff', '-r300',file_name_save)
    end

    %% Write coefficients into excel file
    Save_num = 1000;
    maxlags = 30;
    TimCoe_save = zeros(n_snapshots,Save_num);
    TimCoe_save(:, (1:Save_num)) = TimCoe(:, (1:Save_num));
    xlswrite('TimCoe_3.xlsx',TimCoe_save);
    Corr_1 = zeros((maxlags*2+1),100);
    k4=0;
    for k2=1:10
        for k3=1:10
            k4=k4+1;
            Corr_1(:, k4) = xcorr(TimCoe(:,k2),TimCoe(:,k3),maxlags,'coeff');
        end
    end
    contourf(Corr_1);
    xlswrite('Xcorrel_1.xlsx',Corr_1)
```

APPENDIX E. CARBONYL TRAPPER

Carbon monoxide in nickel containing stainless steel bottles can produce iron pentacarbonyl ($Fe(CO)_5$), melting point: -21.0^{o}C, boiling point: 103°C) and nickel tetracarbonyl ($Ni(CO)_4$), melting point: -17.2^{o}C, boiling point: 43°C) [83]. The evidences of these metallic compounds in combustion tests can be indicated by oxide deposits on quarts liner. As shown in Fig. F.1 quartz liner is contaminated by reddish deposits after combustion test of CO containing fuels. To determine the source of these deposits which prevent the investigation of flame structures, the particles are collected on the specimen (Fig. F.2) for the analysis of Rietveld refinement using X-ray diffractometer (XRD, Model: Bruker D8 Advance, Fig. F.3). From the results of XRD, shown in Fig. F.4, the reddish deposits were determined to be iron oxide (Fe_2O_3) which was produced by the oxidation of iron pentacarbonyl. Thus, to eliminate these carbonyl compounds, devised is the cold trapper which can filter them in CO gas after solidifying and/or liquefying. The trapper was implemented by immersing the 2m-long metal line in the alcohol bed at the temperature of 60°C. Stream temperature of CO outlet was maintained at below 30°C which is lower than the melting point of metal carbonyl. Better images of CO containing syngas flames were achieved but the contamination problems were still remained after long combustion test of high CO containing fuels. Thus, the clear images were obtained by the repeated replacement of quartz liner while using the carbonyl trapper.

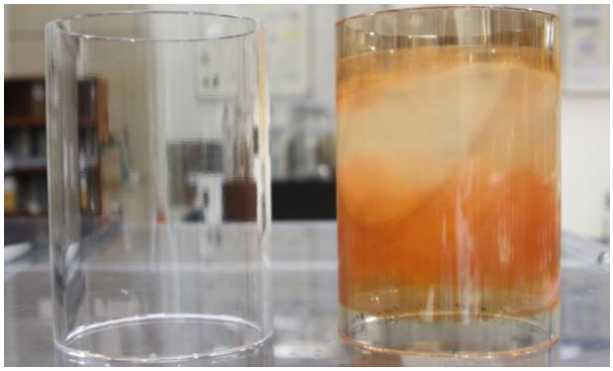

Fig. E.1 Comparison of quartz tubes between before (left) and after (right) burning of CO containing fuels.

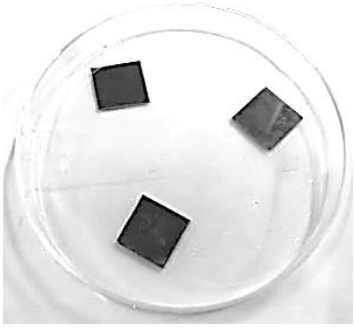

Fig. E.2 Reddish particles colleted for XRD analysis

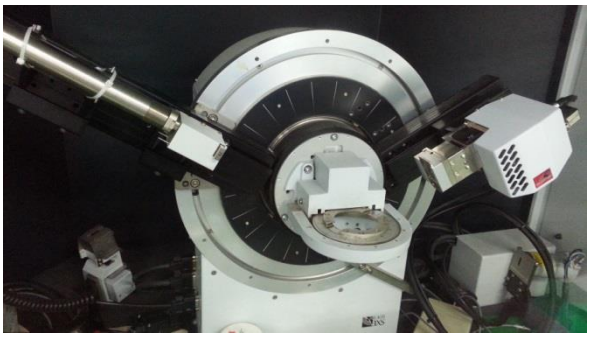

Fig. E.3 XRD Analyzer (D8 Advance)

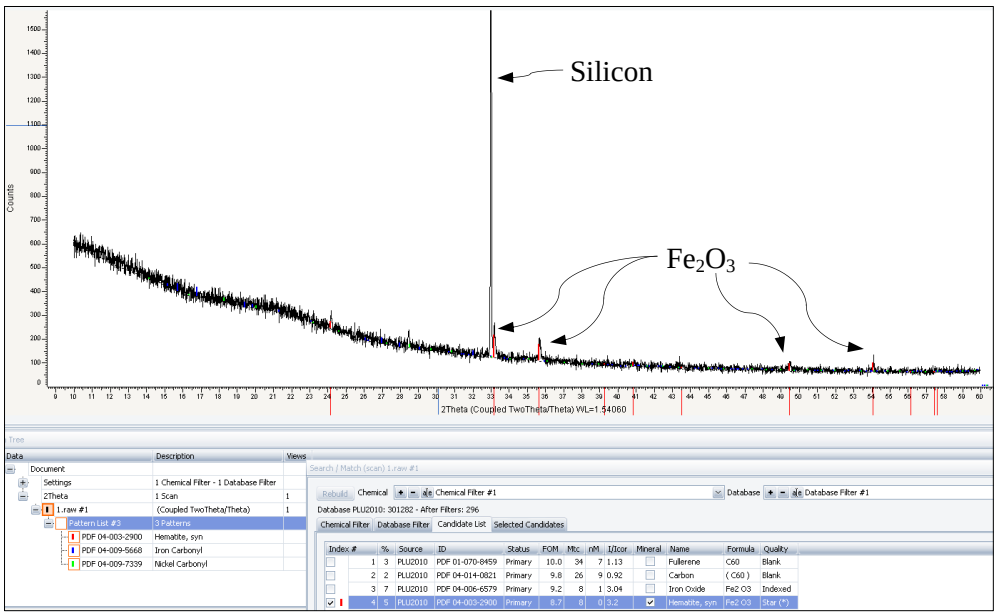

Fig. E.4 XRD Analysis result (2-theta vs. intensity).

REFERENCES

[1] Friedman TL., "Code green, hot flat and crowded", 2008, New York, International creative management, Inc.

[2] Hornick MJ, McDaniel JE., "Tampa electric Polk power station integrated gasification combined cycle project final technical report", U. S. DOE project 2002, DE-FC21-91MC27363.

[3] Dowd RA "Wabash river coal gasification repowering project final technical report. U. S. DOE project", 2000, DE-FC21-92MC29310.

[4] Phillips J, "Integrated gasification combined cycle design consideration for high availability", EPRI Technical Report, 2007, 1012226.

[5] Natarajan J, Lieuwen T, Seitzman J, "Laminar flame speeds of H_2/CO mixtures : Effect of CO_2 dilution, preheat temperature, and pressure", Comb. and flame, 2007, 151:104-119.

[6] Dong C, Zhou Q, Zhao Q, Zhang Y, Xu T, Hui S, "Experimental study on the laminar flame speed of hydrogen/carbon monoxide/air mixtures", Fuel, 2009, 88:1858-1863.

[7] Walton SM, He X, Zigler BT, Wooldridge MS. "An experimental investigation of the ignition properties of hydrogen and carbon monoxide mixtures for syngas turbine applications", Proc. Combust. Inst., 2007, 31:3147-3154.

[8] Kalitan DM, Petersen EL, Mertens JD, Crofton MW, "Ignition of lean CO/H_2/Air mixtures at elevated pressures", Proc. ASME Turbo Expo 2006, GT2006:90488.

[9] Xu G, Tian Y, Song Q, Fang A, Cui Y, Yu B, Nie C, "Flashback limit and mechanism of methane and syngas fuel", Proc. ASME Turbo Expo 2006, GT2006:90521.

[10] Lieuwen T, McDonell V, Petersen E, Santavicca D. "Fuel flexibility influences on premixed combustor blowout, flashback, autoignition, and stability", J. Eng. for Gas Turbine and Power, 130:011506.

[11] Noble DR, Zhang Q, Shareef A, Tootle J, Meyers A, Lieuwen T. “Syngas mixture composition effects upon flashback and blowout”, Proc. ASME Turbo Expo 2006, GT2006:90470.

[12] Whitty KJ, Zhang, HR, Eddings EG, “Emissions from syngas combustion”, Comb. Sci. and Tech., 2008, 180:1117-1136.

[13] Giles DE, Som S, Aggarwal SK. “NOx emission characteristics of counterflow syngas diffusion flames with airstream dilution”, Fuel , 2006, 85:1729-1742.

[14] Konnov AA, Dyakov IV, Ruyck JD, “Nitric oxide formation in premixed flames of H_2+CO+CO_2 and air”, Proc. Combust. Inst., 2002, 29:2171-2177.

[15] Littlejohn D, Cheng RK, Noble DR, Lieuwen T. “Laboratory investigations of low-swirl injectors operating with syngases”, J. Eng. for Gas Turbine and Power, 2010, 132:011502.

[16] Dodo S, Asai T, Koizumi H, Takahashi H, Yoshida S, Inoue H, “Performance of a multiple-injection dry low NOx combustor with hydrogen-rich syngas fuels”, J. Eng. for Gas Turbine and Power, 2013, 135:011501.

[17] Hasegawa T, Tamaru T, “Gas turbine combustion technology reducing both fuel-NOx and thermal NOx emissions for oxygen-blown IGCC with hot/dry synthetic gas cleanup”, J. Eng. for Gas Turbine and Power, 2007, 129:358-369.

[18] Hasegawa T, Nakata T, “A study of combustion characteristics of gasified coal fuel”, Trans. of the ASME, 2001, 123:22-32.

[19] Nakata T, Sato M, Ninomiya T, Hasegawa T, “A study on low NOx combustion in LBG-fueled 1500°C -class gas turbine”, Trans. of the ASME, 1996, 118:534-540.

[20] Lee MC, Seo SB, Chung JW, Kim SM, Joo YJ, Ahn DH, “Gas turbine combustion performance test of hydrogen and carbon monoxide synthetic gas”, Fuel, 2010, 89:1485-1491.

[21] Lee MC, Seo SB, Yoon J, Kim M, Yoon Y, “Experimental study on the effect of N_2, CO_2, and steam dilution on the combustion performance of H_2 and CO synthetic gas in an industrial gas turbine”, Fuel, 2012, 102:431-438.

[22] Külsheimer C, Buchner H, “Combustion dynamics of turbulent swirling flames”, Combust. Flame, 2002;131:70–84.

[23] Schadow KC, Gutmark E, Parr TP, Parr DM, Wilson KJ, Crump JE, “Large-scale coherent structures as drivers of combustion instability”, Combust. Sci. Technol., 1989, 64:167–186.

[24] Lieuwen T, Torres H, Johnson C, Zinn BT, “A mechanism of combustion instability in lean premixed gas turbine combustors”, J. Eng. Gas Turb. Power, 2001, 123:182–189.

[25] Seo S, “Combustion instability mechanism of a lean premixed gas turbine combustor.”, J. Mech. Sci. Technol., 2003, 176:906–913.

[26] Sattelmayer T, “Influence of the combustor aerodynamics on combustion instabilities from equivalence ratio fluctuations”, J. Eng. Gas Turb. Power, 2003, 123:11–19.

[27] Eckstein J, Freitag E, Hirsch C, Sattelmayer T, “Experimental study on the role of entropy waves in low-frequency oscillations in a RQL combustor”, J. Eng. Gas Turb. Power, 2006, 128:264–270.

[28] Steinberg AM, Boxx I, Stohr M, Carter CD, Meier W, “Flow-flame interactions causing acoustically coupled heat release fluctuations in a thermo-acoustically unstable gas turbine model combustor”, Combust. Flame, 2010, 157:2250–2266.

[29] Syred N, “A review of oscillation mechanisms and the role of the precessing vortex core (PVC) in swirl combustion systems”, Prog. Energy Combust. Sci., 2006, 32:93–161.

[30] Kim KT, Santavicca DA, “Interference mechanism of acoustic/convective disturbances in a swirl-stabilized lean-premixed combustor”, Combust. Flame, 2013, 160:1441-1457.

[31] Komarek T, Polifke W, “Impact of swirl fluctuations on the flame response of a perfectly premixed swirl burner”, J. Eng. Gas Turb. Power, 2010, 132:061503.

[32] Wang S, Yang V, “Unsteady flow evolution in swirl injectors with radial entry. Ⅱ. Extuernal excitations”, Phys. Fluids, 2005, 17:045107.

[33] Acharya V, Shreekrishna, Shin D, Lieuwen T, “Swirl effects on harmonically excited, premixed flame kinematics”, Combust. Flame, 2012, 159:1139–1150.

[34] Steinberg AM, Arndt CM, Meier W, “Parametric study of vortex structures and their dynamics in swirl-stabilized combustion”, Proc. Combust. Inst., 2013, 34:3117-3125.

[35] Boxx I, Stohr M, Carter CD, Meier W, “Temporally resolved planar measurements of transient phenomena in a partially pre-mixed swirl flame in a gas turbine model combustor”, Combust. Flame, 2010, 157:1510-1525.

[36] Davis DW, Therkelsen PL, Littlejohn D, Cheng RK, “Effects of hydrogen on the thermo-acoustics coupling mechanisms of low-swirl injector flames in a model gas turbine combustor”, Proc. Combust. Inst., 2013, 34:3135-3143.

[37] Lieuwen T, McDonell V, Petersen E, Santavicca DA, “Fuel flexibility influences on premixed combustor blowout, flashback, autoignition, and stability”, J. Eng. Gas Turb. Power, 2008, 130:011506.

[38] Kim D, Park SW, “Forced and self-excited oscillations in a natural gas fired lean premixed combustor”, Fuel Processing Technol., 2010, 91:1670-1677.

[39] Kim KT, Hochgreb S, “Measurements of triggering and transient growth in a model lean-premixed gas turbine combustor”, Combust. Flame, 2012, 160:1215-1227.

[40] Palies P, Schuller T, Durox D, Candel S, “Modeling of premixed swirling flames transfer functions”, Proc. Combust. Inst., 2011, 33:2967-2974.

[41] Palies P, Durox D, Schuller T, Candel S, “The combined dynamics of swirler and turbulent premixed swirling flames”, Combust. Flame, 2010, 157:1698-1717.

[42] Palies P, Durox D, Schuller T, Candel S, “Nonlinear combustion instability analysis based on the flame describing function applied to turbulent premixed swirling flames”, Combust. Flame, 2011, 158:1980-1991.

[43] Allison PM, Driscoll JF, Ihme M, “Acoustic characterization of a partially-premixed gas turbine model combustor: Syngas and hydrocarbon fuel comparisons”, Proc. Combust. Inst., 2013, 34:3145-3153. Syngas CI, RI

[44] Shin W, Lee JG, Santavicca DA, “Stability and emissions characteristics of a lean premixed gas turbine combustor”, Proc. Combust. Inst., 1996, 26:2771-2778

[45] Syred N, “A review of oscillation mechanisms and the role of the precessing vortex core (PVC) in swirl combustion systems”, Prog. Energy Combust. Sci., 2006, 32:93–161.

[46] Tran N, Ducruix S, Schuller T, “Damping combustion instabilities with perforates at the premixer inlet of a swirled burner”, Proc. Combust. Inst., 2009, 32:2917-2924.

[47] Dodo S, Asai T, Koizumi H, Takahashi H, Yoshida S, Inoue H, “Performance of a multiple-injection dry low NOx combustor with hydrogen-rich syngas fuels”, J. Eng. Gas Turb. Power, 2013, 135:011501.

[48] Lieuwen T, Yang V, Yetter R, “Synthesis gas combustion: fundamentals and applications”, CRC Press, U.S.A., 2010.

[49] Richards GA, McMillian MM, Gemmen RS, Rogers WA, Cully SR, “Issues for low-emission, fuel-flexible power systems”, Prog. Energy Combust. Sci., 2001, 27:141–169.

[50] Figura L, Lee JG, Quay BD, Santavicca DA, “The effects of fuel composition on flame structure and combustion dynamics in a lean premixed combustor”, ASME Turbo Expo 2007, Montreal, Canada, GT2007:27298.

[51] Williams TC, Shaddix CR, “Contamination of carbon monoxide with metal carbonyls: Implications for combustion research”, Combust. Sci. Technol., 2007, 179:1225-1230.

[52] Rumminger MD, Linteris GT, “The role of particles in the inhibition of counterflow diffusion flames by iron pentacarbonyl”, Combust. Flame, 2002, 128:145-164.

[53] Sterling JD, Zukoski EE, “Nonlinear dynamics of laboratory combustor pressure oscillations”, Combust. Sci. Technol., 1991, 77:225‑238.

[54] Billoud G, Galland MA, Huu CH, Candel S, “Adaptive active control of

combustion instabilities", Combust. Sci. Technol., 1992, 81:257–283.

[55] Gulati A, Mani R, "Active control of unsteady combustion-induced oscillations", J. Propul. Power, 1992,8:1109–1115.

[56] Fleifil M, Hathout MP, Annaswamy AM, Ghoniem AF, "The origin of secondary peaks with active control of thermoacoustic instability", Combust. Sci. Technol., 1998, 133:227-265.

[57] Dennis RA, Shelton WW, Le P, "Development of baseline performance values for turbines in existing IGCC applications", Proc. ASME Turbo Expo 2007, GT2007: 28096.

[58] Pack J, Bae DS, Cha MS, Yun JH, Keel SI, Cho HC, Kim TK, Ha JS. "Flame characteristics in H_2/CO synthetic gas diffusion flames diluted with CO_2 : Effects of radiative heat loss and mixture composition", Hydrogen Energy, 2008, 33:7256-7264.

[59] Korean 300MW IGCC demonstration agency website (http://www.igcc.or.kr/)

[60] Environmental impact assessment of Gwangyang synthetic natural gas plant construction project, 2010.

[61] Petersen EL, Hall JM, Smith SD, Vries J, Amadio A, Crofton MW, "Ignition of lean methane-based fuel blends at gas turbine pressures". J. Eng. Gas Turbines Power, 2007, 129(4):937-944.

[62] Vries J, Petersen EL, "Autoignition of methane-based fuel blends under gas turbine conditions", Proc. Combust. Inst., 2007, 31: 3163-3171.

[63] Flores RM, Miyasato MM, McDonell VG, Samuelsen GS, "Response of a Model Gas Turbine Combustor to Variation in Gaseous Fuel Composition," J. Eng. Gas Turbines Power, 2001, 123: 824-831.

[64] Flores RM, McDonell VG, Samuelsen GS, "Impact of Ethane and Propane Variation in Natural Gas on Performance of a Model Gas Turbine Combustor," J. Eng. Gas Turbines Power, 2003, 125: 701-708.

[65] Yoshimura T, McDonell V, Samuelsen S, "Evaluation of hydrogen addition to natural gas on the stability and emissions behavior of a model gas turbine

combustor", ASME Turbo Expo 2005, GT2005-68785.

[66] Jones HRN, Leng J, "The effect of hydrogen and propane addition on the operation of a natural gas-fired pulsed combustor," Combust. Flame, 1994, 99:404-412.

[67] York WD, Ziminsky WS, Yilmaz E, "Development and testing of a low NOx hydrogen combustion system for heavy duty gas turbines", ASME Turbo Expo 2012, GT2012-69913.

[68] Turns SR, "An introduction to combustion", 1999, Singapore, McGraw-Hill, pp. 527-60.

[69] Mathur ML, Maccallum NRL, "Swirling air jets issuing from vane swirlers part-1; free jets". J. Inst. Fuel, 1967, 39: 214-225.

[70] Lefebvre AH, Ballal DR. "Gas turbine combustion", 3rd ed., 2010, Boca Raton, Taylor&Francis, pp. 364-366.

[71] Felder RM, Rousseau RW, "Elementary principles on chemical processes", 3rd ed., 1999, New York, John Wiley & Sons, Inc., pp. 627-634.

[72] Warnatz J, Maas U, Dibble RW, "Combustion", 2nd ed., 1999, Germany, Springer, pp. 219-231.

[73] LaViolette M, Perez R. "On the prediction of pollutant emission indices from gas turbine combustion chambers", ASME Turbo Expo 2012, GT2012-70038.

[74] LaViolette M, Strawson M, "On the prediction of nitrogen oxides from gas turbine combustion chambers using neural networks", ASME Turbo Expo 2008, GT2008-50566.

[75] Putnam AA, Dennis WR, "Organ-pipe oscillations in a flmae-filled tube" Proc. Comb. Inst., 1953, 4:566.

[76] Chen H, Reuss DL, Hung DL, Sick V, "A practical guide for using proper orthogonal decomposition in engine research", Intern. J. Engine Research, 2012, 14:307–319.

[77] Lee J, Park S, Kim Y, "Effects of fuel-side nitrogen dilution on structure and NOx formation of turbulent syngas non-premixed jet flames", Energy and Fuels,

2012, 26:3304-3315.

[78] Black WZ, Hartley JG, “Thermodynamics”, 3rd ed., 1996, New York, Harper Collins College Publishers, A3-A84.

[79] Lieuwen T, Torres H, Johnson C, Zinn BT. “A mechanism of combustion instability in lean premixed gas turbine combustors”, J. Eng. Gas Turbine Power, 2001, 123:182-9.

[80] Shih W, Lee JG, Santavicca DA, “Stability and emissions characteristics of a lean premixed gas turbine combustor”, Proc. Combust. Inst., 1996, 26:2771-2778.

[81] Kim J, Yoon Y, Park CW, Hahn JW, “The characteristic modes and structures of bluff-body stabilized flames in supersonic coflow air”, Int. J. Aero. and Space Sci., 2012, 13(3):386-397.

[82] Kinsler LE, Frey AR, Coppens AB, Sanders JV, “Fundamentals of acoustics”, 2000, USA, John Wiley & Sons Inc., pp. 46-54.

[83] Bouvet N, “Experimental and numerical studies of the fundamental flame speeds of methane/air and syngas (H_2/CO)/air mixtures”, 2009, PhD Thesis of ICARE-CNRS.

초 록

본 논문에서는 석탄가스화 복합발전(Integrated gasification combined cycle, IGCC) 및 합성 천연가스(Synthetic natural gas, SNG) 플랜트에 적용되는 신연료의 가스터빈 연소특성을 이해하기 위해 높은 수소함량에서도 역화를 방지할 수 있는 부분 예혼합 가스터빈 연소기 내에서 다양한 조성의 수소, 일산화탄소, 메탄으로 구성된 합성가스의 화염 및 연소기 온도, NO_x 및 CO 배출, 연소불안정, 화염의 안정성, 그리고 화염의 구조 등에 관해 조사하였다. 연소불안정시 자세한 화염구조의 파악을 위해서는 영상증폭 초고속카메라를 이용하여 초당 12500장의 OH라디칼의 자발광을 촬영하거나, 평면 레이저 유도 형광법(Planar laser induced fluorescence, PLIF)을 이용하여 동압과 위상 동기된 OH라디칼의 분포를 획득하였다.

수소, 일산화탄소, 메탄의 비율을 각각 0%에서 12.5%의 간격으로 100%까지 바꾸어 가며 실험을 하여 삼각형도(Ternary diagram)를 통해 각각의 연소성능인자의 경향성을 확인하였다. NO_x 배출의 경우 화염온도의 영향이 지배적인 높은 수소 조성과 체류시간의 영향이 지배적인 높은 일산화탄소 조성에서 높게 나타나는 것이 특징적이었고, 이는 화염의 구조와 연소실 온도로도 설명 가능하였다. 수소와 메탄 합성가스 연소시 연소불안정 크게 나타났으며, 그 때 주요 주파수는 3, 4, 6번 길이방향 모드에 해당하는 750Hz와 1000Hz, 1500Hz로 연료조성의 변화에 따라 다양한 주파수 및 모드 특성이 나타났다. 또한 일부 조성의 경우 이들 주파수의 배음(Harmonics)과 함께 나타났고, 이러한 다중

고주파 불안정 그리고 주파수 및 모드 천이 현상에 대해 연소 물성, OH 자발광(Chemiluminescence), OH-PLIF, Rayleigh 지수, 고유 직교함수 전개(Proper orthogonal decomposition, POD), 시간지연분석(Time-lag analysis)을 통해 그 원인 및 특성을 파악하였다. CHEMKIN 프로그램을 통해 단열화염온도 및 층류 화염속도를 계산한 결과 불안정 주파수 및 모드는 이들 두 물성에 비례하여 증가하는 경향을 보였고, 층류 화염속도가 큰 수소가 크게 영향을 미치는 것을 확인할 수 있었다. 또한 수소 함량이 높은 불안정 조건에서는 짧은 화염 형태로 인해 Rayleigh 지수가 노즐부에 가까운 위치에서 크게 나타나는 것을 Raleigh 선도를 통해 확인할 수 있었고, 적분된 Rayleigh 지수를 통해 압력섭동과 열발생량의 변화가 결합하여 불안정을 증폭시키는 것이 각각의 모드에서 동일하게 나타났다. 하지만 수소함량이 낮은 3번 모드의 경우 6번 모드와 함께 나타나서 동압이 많이 찌그러진 형태로 나타났고, 이로 인해 Rayleigh 지수의 주파수가 일반적인 경우에는 동압 주파수의 2배가 되지만 이 경우에서는 그렇지 않은 것을 확인할 수 있었다. POD 분석을 통해 각각의 모드에서 고유한 화염의 응집성 구조(Coherent structure)를 가지는 것을 확인하였고, 상호상관관계 분석(Cross-correlation)을 통해 화염의 대류전파, 스월 및 난류특성 구조를 확인하였다. 시간지연분석을 실시한 결과 연료-공기 혼합거리가 짧은 부분 예혼합 연소기에서 화염의 구조가 특성시간에 미치는 영향이 매우 큼을 확인하고, 높은 모드가 나타나는 현상은 혼합거리가 짧아 총 지연시간이 짧아져서 불안정의 주파수 및 모드가 증가하기 때문이라는 것을 확인하였고, 연료

조성에 따른 민감한 모드의 천이 현상은 화염의 구조가 연료의 조성에 대해 매우 크게 변화하여, 화염으로부터 연료분사구까지의 거리가 큰 변화를 보이기 때문인 것으로 확인되었다. 이를 좀 더 확실히 증명하기 위해 시간 1차원의 화염구조부터 예측한 불안정 구간과, 2차원 그리고, 음압이 찌그러진 다중 모드에 대한 해석을 동시에 수행하여 상호 비교하였다. 이 때 2차원 화염구조의 계산은 화염의 PLIF 영상의 강도중심(Intensity centroid)을 계산하여 대류시간, 음향시간 등을 계산하였으며, 그 결과 2차원의 화염구조로부터 계산한 지연시간이 1차원의 얇은 화염가정의 경우보다 더 불안정 예측 정도가 높았다. 또한 다중 불안정 모드의 경우 음압이 삐뚤어짐으로 인해 지연되는 시간을 수학적으로 뒤틀림 시간(Skewness time) 계산한 후 그 영향이 큼을 확인하였고, 이를 고려하였을 때 불안정 예측 정확도가 크게 향상됨을 확인할 수 있었다.

합성가스 연료상에 질소, 이산화탄소, 스팀의 희석제를 추가하였을 경우 연소특성 변화를 관찰하였다. 희석제는 화염온도 및 연소실 온도를 저감시키는 데 효과적일 뿐 아니라 NO_x 및 연소불안정의 저감에도 효과적 이였으나, 저부하 높은 CO 조성의 합성가스에서는 과다한 CO 발생으로 인한 불완전 연소현상이 나타났다. 각각의 희석제가 NO_x 저감에 미치는 영향을 분석한 결과 단위 입열량 당 NO_x 저감량은 희석제 열용량에 로그형태로 비례함을 확인할 수 있었고, 이를 모든 희석제에 대해 하나의 상관관계 함수 형태로 분석적 해를 유도하여 나타내었으며, 그 결과는 실험결과와 정확히 일치하였다.

한편 상기 실험결과를 기초로 하여 실제 상업용 연료인 태안 IGCC용 석

탄가스 및 천연가스를 대체용 합성 천연가스를 대상으로 연소 실험을 수행하였다. 수소/일산화탄소 비가 1:2인 석탄가스 연소실험 결과 질소희석이 화염의 안정성 및 CO 발생량 측면에는 불리하나 상당한 안정성 여유를 두고 운전이 가능함을 확인하고, NO_x 저감에는 매우 효과적임을 확인하였다. SNG의 경우 웨버지수(Weber index)를 고정시키면서 수소함량이 0%, 1%, 3%, 5%로 변화시킨 C0, C1, C3, C5의 SNG 가스에 대해 연소특성을 관찰하였다. 상기의 SNG 연소시 온도, NO_x/CO 배출 특성은 동일하였으나, 연소불안정 특성에 있어서는 C0 및 C1 SNG가 C3 및 C5 SNG와 진동의 크기와 주파수가 다소 상이함을 확인하였고, 이는 화염의 고속촬영을 통해 구체적으로 가시화 되었다. 상기 결과에서는 1% 이상일 때도 연소불안정에 심각한 수준으로는 영향을 미치지는 않지만, 각종 가스터빈의 형태가 다양함을 고려할 때 변화를 보이기 시작하는 1%의 수소함량이 안정적인 SNG의 품질 기준이라고 제시할 수 있다.

주요어: 연소불안정, 질소산화물, 합성가스, 가스터빈 연소, 석탄가스화 복합발전, 합성 천연가스

학 번: 2011-30206

감사의 글

박사과정 중 어려울 때 마다 지혜를 주시고, 위로해 주시며, 삶을 인도해 주신 하나님께 모든 영광을 돌립니다.

회사 근무 중 박사과정 교육을 통해 원없이 공부할 수 있는 시간을 가질 수 있었음에 참으로 행복했습니다. 이러한 좋은 기회를 제공해 준 회사와 교육 담당자 분들과 저의 부재 기간 동안 대신 고생해 준 KEPCO 전력연구원 IGCC 연구팀원들께 진심으로 감사의 말씀을 드립니다.

많이 부족한 제가 과분한 논문을 쓸 수 있도록 지도해 주신 윤영빈 지도 교수님께 진심으로 감사드리며, 바쁘신 중에도 제 연구 내용이 더 충실해 질 수 있도록 귀한 조언과 날카로운 지적을 해 주신 정인석 교수님, 여재익 교수님, 차동진 교수님, 안규복 교수님께 크게 감사 드립니다.

실험실에서 동고동락했던 GT팀 지수, 성필, 정진에게 정말 고맙다는 말을 전하고, 광계측 실험때 마다 도움을 준 정재, 연소라는 주제로 함께 머리 맞대며 토론을 했던 정찬영, 태성, 재익, 연구보다는 축구로 더 많은 시간을 함께 했던 Injector팀 성호, 연재, 구정, 정수, 인규, 현태, 재요, 신입생이라 한학기 밖에 함께 하지 못해 아쉬웠던 정호, 해솔 모두 도와줘서 고맙고, 더 훌륭한 연구로 우리 실험실을 빛내길 응원한다.

좋은 연구와 저희 가정의 안녕을 위해 부단히 기도해 주신 유성중앙교회 배명수 목사님 내외 분과 찬양팀과 구역식구들과 성도님들께 진심으로 감사의 말씀을 드리며, 예수님의 이름으로 축복합니다.

생각만 하면 눈물나도록 감사한 부모님께 그리고, 타지 생활하는 사위 걱정을 쉬지 않으셨던 장인 장모님께 오늘날 저와 저희 가정이 있게 해 주심에 논문을 빌어 감사의 말씀을 올리며, 오래 오래 건강하시길 기도 드립니다. 독일서 동생이 잘 되길 늘 응원해 준 누나네와 지칠 때면 서로 도와주며 형부에게 큰 힘이 되어 준 처제네 모두 정말 고맙습니다.

마지막으로 주말부부 생활을 하며 주중에 홀로 어린 두 아들을 키우느라 고생한 아내 윤경진에게 그리고, 아빠로서 많은 시간을 함께 하지 못해 미안한 두 아들 찬영, 찬승이에게 기다려줘서 고맙다는 말과 영원히 사랑한다는 말을 전합니다.